UNIVERSITÀ
DEGLI STUDI
DI PADOVA

Università degli Studi di Padova

Dipartimento di Scienze Chimiche

SCUOLA DI DOTTORATO DI RICERCA IN SCIENZA ED INGEGNERIA DEI MATERIALI
CICLO XXVI

SYNTHESIS AND CHARACTERIZATION OF PLASMONIC NANOSTRUCTURES WITH CONTROLLED GEOMETRY FOR PHOTONIC APPLICATIONS

Direttore della Scuola: Ch.mo Prof. Gaetano Granozzi
Supervisore: Ch.mo Prof. Giovanni Mattei

Dottorando: Boris Kalinic

A Susanna

"Un minuto intero di beatitudine!
È forse poco per colmare tutta la vita di un uomo?..."
Fëdor Dostoevskij, Le notti bianche

Abstract

The purpose of the present thesis is the study of the interaction of plasmonic and pre-plasmonic nanostructures with an emitter in close proximity. The investigation was carried out following different approaches but always with the aim of inserting the experimental results in the framework of new or existing theoretical models in order to better understand the photophysical nature of the interaction. To this aim in the framework of this thesis different nanoarchitectures have been synthesised and coupled to Er-doped silica layers. The choice of Erbium as emitting source was driven by the great technological importance of this rare earth in photonics and optoelectronics, connected to the characteristic emission at 1540 nm that matches the window of minimum transmission loss for silica. For this reason the first step of the research activity was devoted to the optimization of the Er^{3+} photoluminescent properties in silica.

When an emitter is placed near an interface, its optical properties will be modified. To describe this variation different contributions have to be taken into account: the variation of the local density of state due to the reflection from the interface, the coupling of the emitted radiation with propagating surface plasmons on the metal-dielectric interface and the dissipation in the overlayer. All these aspects have been studied in detail for different overlayer materials demonstrating that the strong control of the excited state lifetime of the emitter can be obtained by tailoring the dielectric properties of the overlayer and the separation distance from the interface.

Nanostructuring the overlayer offers further opportunities for changing the optical properties of a nearby emitter. Among different plasmonic nanostructures, nanohole arrays (NHAs) can represent the ideal candidate for this purpose due to their extraordinary optical transmission (EOT): at specific frequencies determined by the hole periodicity, the light transmitted through the NHA is orders of magnitude higher than the one predicted with the classical diffraction theory. When the EOT peak was tailored with the emission wavelength of the emitter strong plasmonic coupling was demonstrated, leading to lifetime shortening with almost no dissipation in the overlayer.

The improvement of the optical performances of an emitter can be obtained not only acting on the decay from the excited state but also increasing the excitation efficiency. For this purpose, an interesting possibility that has been explored is the sensitization by of ultra-small molecular-like metal nanoclurters (NCs) produced by ion implantation. Noble metal NCs can indeed efficiently absorb light through broad-band interband transitions and transfer energy to a nearby emitter, acting as efficient nanoantennae for excitation of the emitter. Such interaction leads to the increase of the effective excitation cross-section by several orders of magnitude.

Finally, all the obtained results allowed the development of predictive models that can be used in the design of novel devices for different photonic applications.

Estratto

Lo scopo del presente lavoro di tesi è l'analisi dell'interazione di nanostrutture plasmoniche e pre-plasmoniche con un emettitore. Lo studio è stato condotto seguendo diversi approcci, ma sempre con il fine di confrontare i risultati sperimentali con modelli teorici sia già noti che nuovi, in modo da comprendere appieno la natura foto-fisica dell'interazione. In questo senso nell'ambito della presente tesi diverse nano-architetture sono state sintetizzate ed accoppiate con film sottili di silice drogata con erbio. La scelta dell'erbio come emettitore è stata dettata dalla sua grande importanza tecnologica della terra rara nella fotonica e nell'optoelettronica, associata alla caratteristica emissione radiativa a 1540nm, che si trova nella finestra di minimo assorbimento ottico della silice. Per questa ragione il primo passo dell'attività di ricerca è stato volto all'ottimizzazione delle proprietà di fotoluminescenza dello ione erbio in silice.

Quando un emettitore è posto in prossimità di un film sottile le sue proprietà ottiche vengono modificate. Per descrivere tale variazione è necessario tenere conto di contributi differenti: la variazione della densità locale degli stati dovuta alla riflessione all'interfaccia, l'accoppiamento della radiazione emessa con plasmoni di superficie propaganti sull'interfaccia metallo-dielettrico e infine la dissipazione nel film. Tutti questi aspetti sono stati studiati in dettaglio per film di diversi materiali, dimostrando che un ottimo controllo sul tempo di vita dello stato eccitato può essere ottenuto agendo sulle proprietà dielettriche del film e sulla distanza di separazione tra l'emettitore e l'interfaccia.

La nanostrutturazione del film può offrire ulteriori opportunità nella modifica delle proprietà ottiche di un emettitore. Tra le diverse nanostrutture plasmoniche, i *nanohole arrays* (NHAs) possono essere visti come i candidati ideali per questo scopo grazie alla loro trasmissione ottica straordinaria (EOT): a determinate lunghezze d'onda definite dalla periodicità dei buchi e dalle proprietà dielettriche dei materiali coinvolti, la luce trasmessa attraverso il NHA è ordini di grandezza più grande rispetto a quella predetta dalla teoria classica della diffrazione. Quando il picco della EOT è risonante con la lunghezza d'onda di emissione dell'emettitore, è stato dimostrato un forte accoppiamento plasmonico che porta ad un marcato accorciamento del tempo di vita nella quasi assenza di dissipazione nella nanostruttura.

Il miglioramento delle proprietà ottiche di un emettitore può essere ottenuto non solamente agendo sulla parte emissiva del processo, ma anche aumentando la probabilità di eccitazione. A questo scopo, una possibilità interessante è offerta dalla sensitizzazione da aggregati metallici ultra-piccoli ottenuti per impiantazione ionica. Cluster di metalli nobili composti da 10–20 atomi possono infatti assorbire efficientemente la radiazione di eccitazione attraverso transizioni interbanda e trasferire l'energia a un emettitore posto nelle vicinanze, agendo in questo modo da efficienti nanoantenne. Tale interazione può portare ad un aumento della sezione d'urto di eccitazione efficace di diversi ordini di grandezza.

Infine, tutti questi risultati hanno permesso lo sviluppo di modelli predittivi che possono essere utilizzati nella progettazione di nuovi dispositivi per diverse applicazioni fotoniche.

Contents

List of Figures

Introduction

In last decades nanoscience and nanotechnology have been gaining great importance and increased scientific attention due to the possibility of obtaining new properties from materials when they are manipulated at the nanometric scale. At this scale, indeed, changing the morphology implies changing also the physical and chemical properties of matter, many of which are no longer intrinsic but depend on the size, shape, and dielectric environment. One of the most striking examples in this sense is given by the colour of noble metals when they are in nanoparticle form; gold, for example could appear vine-red or green, or bluish or grey simply by changing the size of the nanoparticles. Historically, the first acknowledgement of the importance of the nanoscale range is generally attributed to the Noble prize physicist Richard Feynman in his brilliant lecture "There is plenty of room at the bottom" [1], in which he first proposed that the properties of materials and devices at the nanometer range would present future opportunities. The term "Nano–technology" was first used by N. Taniguchi in a paper in 1974 [2]: *"Nanotechnology mainly consists of the processing of separation, consolidation, and deformation of materials by one atom or by one molecule."* In last two decades nanotechnologies have been the subject of an intense research activity, bringing important innovations in many fields as biological sensors, surface coating, catalysis, computer science, optics, drug delivery, just to mention some of them.

One of the most fascinating fields in nanoscience is the study of the interaction of light with metallic nanostructures and nanoparticles exhibiting unique optical properties never seen in macro–world. This field goes under the name of plasmonics and explores the coupling between electromagnetic radiation and conduction electrons at metallic interfaces or in small metallic nanostructures, that leads to the confinement of light over dimensions smaller than its wavelength and an associated enhancement of the optical near-field [3]. In recent years, an increasing number of papers have been published on plasmonics disclosing the main optical properties of noble metal nanostructures. However, many aspects regarding the possible application of this technology in the realization of photonic devices have still to be investigated. The present work is focused within this framework and it is aimed at exploring the modification of the optical properties of an emitter due to the interaction with plamonic and pre-plasmonic nanostructures.

Since the pioneering work of Purcell [4], it is well known that spontaneous emission is not only a function of the emitting atom but can be modified by the interaction with the external electromagnetic environment. Its decay rate from an excited state can be strongly enhanced by the coupling in the near-field with Surface Plasmon Polaritons (SPPs), i.e. propagating electromagnetic waves confined at the interface between a metal and a dielectric, coupled to surface charge oscillations [3]. The excitation of SPPs by electromagnetic waves incident on the surface can not occur without the use of a prism or grating due to the mismatch in the wave-vector. Conversely, when an emitter is in close proximity ($d \ll \lambda_{em}$) of a planar interface the excitation of such modes can occur directly because of the wide range of wave-vectors available in the near-field of dipole-like emission. Besides the opening of an additional decay channel that increases the de-excitation probability, propagating SPPs can further excite the emitting

species or be coupled out into far-field radiation using a grating that matches the momentum between SPP and photon and thus contribute to the luminescence signal. Moreover, in the presence of an interface, the local density of optical states (LDOS) will be further affected due to reflection from the surface that provides additional paths in which spontaneous emission may occur. The field reflected by the interface indeed will interfere with the emitter and its amplitude and phase will determine whether the emission rate will be enhanced or suppressed. Thus, the lifetime oscillates with increasing distance from the interface since the phase of the reflected field changes with the distance (see Fig. 0.1). The onset of non-radiative decay channels due to dissipation in the overlayer has also to be taken into account. The variation of the decay rate due to the presence of an interface is indeed a complex phenomenon and the optical properties of the surface together with the separation distance play a crucial role on the modification of the radiative lifetime.

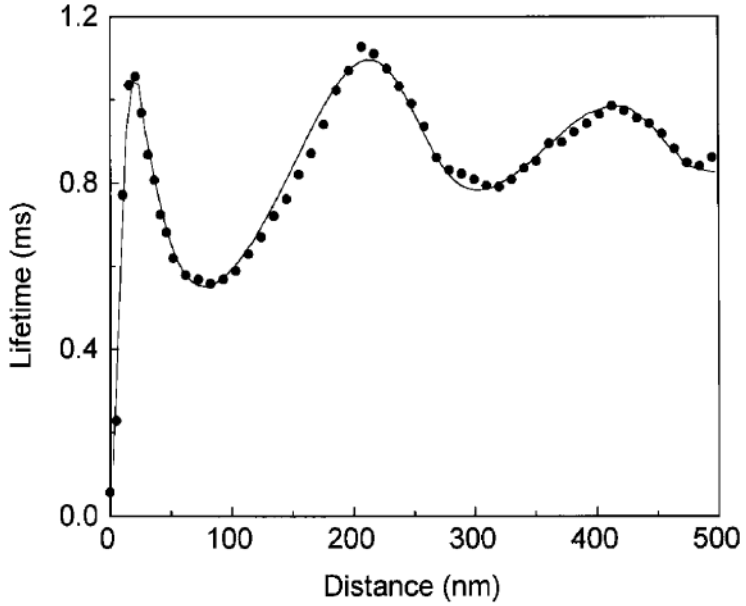

Figure 0.1: Oscillations of the lifetime of an emitter (Eu^{3+}) as a function of the separation distance from an overlayer (Ag). From Ref. [5]

A nanostructured overlayer could in principle offer further opportunities for the enhancement of the decay rate of a nearby emitter. The direct coupling between the emitted radiation and surface plasmons is for example possible when a Nanohole Array (NHA) is placed in the near-field of an emitter. A Nanohole Array is a metal thin film, whose thickness usually ranges from some tens to some hundreds of nanometres, having passing-through holes arranged with an ordered 2D periodicity. The unique property that makes these nanostructures attractive for potential applications in novel photonic architectures is their extraordinary optical transmission (EOT). When a NHA is illuminated with white light, orders of magnitude more light than the one predicted by Bethe's diffraction theory can be transmitted through subwavelengths apertures [6]. The transmittance spectrum shows peaks at specific frequencies, which are related to the periodicity of them. Several models have been suggested to describe this phenomenon and most of them indicate that the extraordinary transmission occurs when the incident excitation matches the surface plasmon resonances. When an emitter is in close

proximity of a NHA with the EOT peak resonant with the emission wavelength, the radiative decay will be strongly influenced by both the variation of LDOS and the coupling with surface plasmon modes on the metal-dielectric interface. Due to the 2D periodicity, the propagating SPPs will couple out in far-field radiation without the need of additional grating. The unique optical properties arising from the extraordinary optical transmission give the possibility not only to collect the emitted radiation from both sides of the nanostructured film, but also to filter the wavelength of the light transmitted through the NHA.

The enhancement of the luminescent properties of an emitter can be obtained not only acting on its decay from the excited state but also increasing the excitation rate, which is proportional to the electromagnetic field acting on emitter. Metal nanoparticles (NPs) can represent an ideal candidate for this purpose since the localized surface plasmon resonance can enhance the field around the nanoparticle by orders of magnitude. However, while some studies demonstrate luminescence enhancement for an emitter placed near a plasmonic nanostructure, other report luminescence quenching. When an emitter is resonantly coupled with a plasmonic NP, indeed, two competitive processes may take place: the local field enhancement leads to an increased excitation rate whereas non-radiative energy-transfer to the particle leads to a decrease of the quantum yield (quenching) [7]. Thus, acting on the shape and size of the nanoparticle together with the separation distance, the optical properties of an emitter can be optimized (see Fig. 0.2).

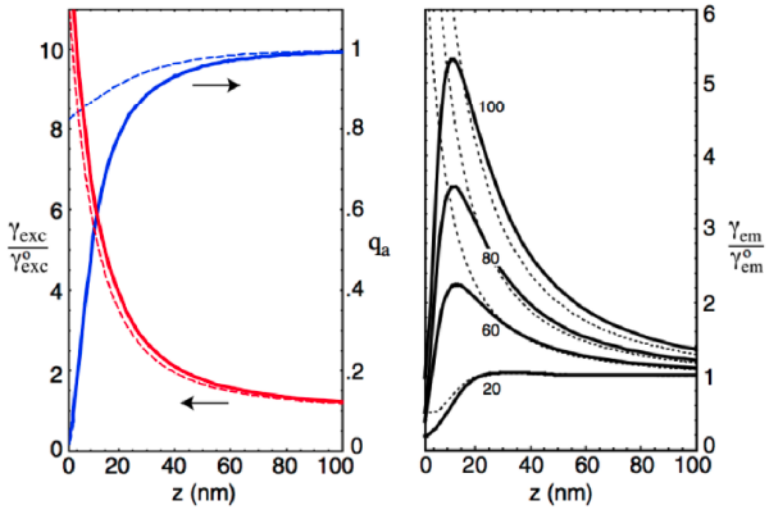

Figure 0.2: Calculated quantum yield q_a, excitation rate γ_{exc} and fluorescence rate γ_{em} for a single molecule located in a distance z from a gold sphere of diameter 80 nm (a) or as indicated in figure (b) [7].

Furthermore, novel and peculiar properties emerge when the dimensions of the nanoparticles are reduced down to sub-nanometer sizes, that is, in a range in which the clusters are too small to have the continuous density of states necessary for plasmon excitations to be supported. Although the light confinement and the subsequent local field enhancement due to plasmon resonance does not occur, nonetheless ultra-small noble metal nanoclusters can deeply influence the excitation and emission dynamics of a nearby emitter. Indeed, pre-plasmonic noble metal NPs made by 100 down to 5 atoms exhibit interesting luminescence properties as they encompass the transition between bulk and molecular regimes, where discrete electronic levels emerge, whose energy separation between the highest occupied molecular orbital and the low-

est unoccupied molecular orbital (HOMO–LUMO gap) is larger than thermal energy even at room temperature. Molecular-like NPs can indeed absorb light under direct HOMO–LUMO excitation or under interband photo-stimulation and transfer energy to an emitter in close proximity, acting as efficient nanoantennae for the luminescent enhancement. The emission rate of the emitter will be also influenced by the presence of pre-plasmonic NPs due to the opening of new decay channels. Moreover, the optical properties of such ultra-small metal clusters are size-tunable, enabling further degrees of freedom in the control of the interaction with an emitter.

A final comment concerns the photoemitting system adopted in the framework of this thesis for the investigation of the coupling effects with plasmonic nanostructures. It is constituted of thin films of Erbium-doped silica. The choice to work with Er is related to its technological importance connected to the characteristic emission at 1540 nm that matches the window of minimum transmission loss for silica. In fact, Erbium doped fiber amplifiers (EDFAs) are widely used to compensate losses in the transmission of optical signals over long distances. However, the Er-doped glass technological applications are limited by the small excitation cross-section and the long lifetime of the Er excited state (typically of the order of milliseconds). The long lifetime makes Er ions sensitive to non-radiative de-excitation processes (such as cooperative up-convertion, energy migration, excited state absorption) and limits the maximum Er concentration as doping element due to the occurrence of concentration quenching phenomena [8]. In this context, the interaction between the rare-earth and plasmonic and pre-plasmonic nanostructures could represent a possible way to overcome these limitations and open the possibility for the realization of a wide range of photonic and optoelectronic devices (e.g. planar optical amplifiers, solid state lasers and light sources).

1 Er:SiO_2 thin films

1.1 Introduction

Er-doped silica-based materials are of strategic interest in the field of optical communication technology for their application as active elements in many photonic devices [8–11]. In particular, this is related to the sharp room temperature luminescent emission at 1540 nm of the Er^{3+} ions that matches the window of minimum loss in silica optical fibers. The present chapter will focus on the synthesis and the characterization of Er-doped silica thin films obtained by co-sputtering and ion implantation, investigating the effects of the preparation parameters in order to optimize the photoluminescence performances of Er^{3+} ions embedded in the silica matrix. Although both techniques give the possibility of obtaining thin films with a high control on the concentration of the dopant, the choice between the two permits the control over a different set of synthesis parameters; in particular, by sputtering deposition the thickness of the Er-doped film can be varied from few nanometers to hundred of microns of single films or multi-layers. With ion implantation, instead, it is possible to introduce as many doping species as required with multiple implantations. Furthermore, the concentration depth profile of the doping species is essentially flat in the co-sputtered films, while it is roughly Gaussian for ion implantation, although it is possible to obtain a different concentration profiles with an broad plateaux of constant concentration with multiple implantation (by varying energy and fluence). Moreover, both synthesis techniques require a high temperature annealing for the activation of Er^{3+} characteristic photoemission at 1.54 μm. The synthesis parameters and annealing conditions, such as temperature, duration, and furnace atmosphere, have an important role on the intensity of the PL signal and on the Er^{3+} lifetime, and will be extensively investigated in order to maximize the Er^{3+} quantum efficiency.

1.2 Er^{3+} optical properties

Erbium is a rare earth element in the Lanthanides series with atomic number 68. The electronic configuration of neutral Er atoms is [Xe]-$4f^{12}6s^2$, while the most common form of Erbium when embedded in a solid is the ionic trivalent state Er^{3+}, which has an electronic configuration [Xe]-$4f^{11}$. Er ionization involves the removal of the two weakly bounded 6s electrons and one from the 4f shell. Therefore Er^{3+} ion has an incompletely filled $4f$ electron shell shielded from its environment by the outer-lying filled $5s^25p^6$ shells from the [Xe] configuration [12]. The electrostatic shielding of the $4f$ electron shell from its environment by the $5s$ and $5p$ electrons is responsible for the Er rich optical spectrum. Due to the incomplete $4f$ shell, several electronic configurations arise with different energies due to spin-spin and spin-orbit interactions. The energy level scheme of Er^{3+}, up to the blue-green region of the spectrum is shown in Fig. 1.1(a). The scheme is labelled with the Russell-Saunders notation and the corresponding transition wavelength. In the case of the free ion the degenerate levels are sharp with equal parity and therefore the electric-dipole transitions involving one photon between

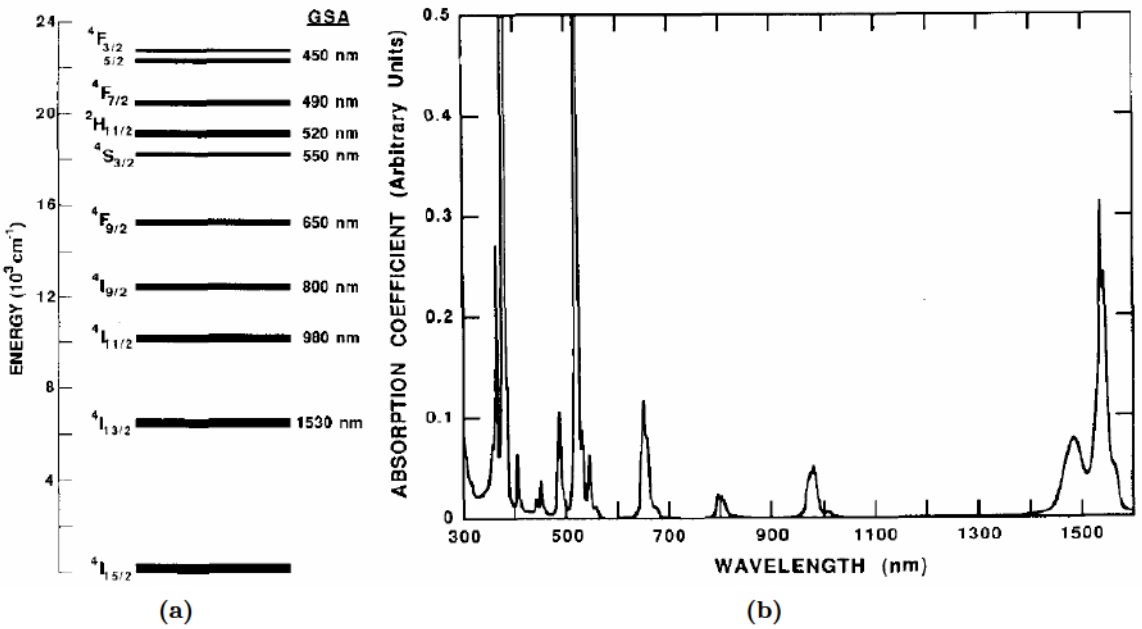

Figure 1.1: (a) Energy levels of Er^{3+} labelled with the Russell-Saunders notation. For each state the GSA column lists the wavelength of the ground-state absorption transition terminating on it. (b) Absorption spectrum of Er-doped silicate glass. The peaks of the strong bands at 380 and 520 nm are 1.5 and 1.0, respectively [9].

most of these energy states are parity forbidden. However, when Er ion is embedded in a host material the surrounding chemical species weakly perturb the $4f$ state, inducing odd-parity character in the $4f$ wavefunctions and allowing for the occurrence of radiative transitions. Moreover, the incorporation in matrix causes Stark-splitting of the different energy levels into manifolds, as pointed out in Fig. 1.1(a), giving the typical broadening of absorption peaks observed in the spectrum in Fig. 1.1(b).

PL emission spectrum

The Er excitation process originating the characteristic $^4I_{13/2} \rightarrow ^4I_{15/2}$ transition at 1.54 μm occurs with the absorption of a photon in one of the higher-lying levels and it is followed by the non-radiative fast multiphonon decay to the metastable $^4I_{13/2}$ state (τ<10 ns) [13]. Due to the large relaxation energy of about 0.8 eV between the $^4I_{13/2}$ state and the ground state, multiphonon emission is unlikely and the characteristic radiative emission at 1.54 μm occurs. The PL emission spectrum shape depends on the host glass, the peaks and the valleys are determined by the locations of the Stark levels, the intensity of the transition between the Stark levels, and the amount of inhomogeneous and homogeneous broadening of these levels [14]. A typical emission spectrum of Er^{3+} in silica is represented in Fig. 1.3(a).

Lifetime

The lifetime (τ) of an excited level is given by the sum of the inverse of the probabilities of radiative (γ_r) and non-radiative (γ_{nr}) decay:

$$\frac{1}{\tau} = \gamma_r + \gamma_{nr} = \frac{1}{\tau_r} + \frac{1}{\tau_{nr}}. \tag{1.1}$$

For Erbium embedded in a glassy host the upper level of the characteristic transition at 1.54 μm ($^4I_{13/2}$) is separated by a large energy gap from the ground state ($^4I_{15/2}$), so that its lifetime is usually in the millisecond range and mostly radiative: the phononic non-radiative transition probability drops exponentially with the number of phonons required to bridge the energy gap to the next lowest level. However, the measured lifetime strongly depends on the host matrix since the decay rate of the non-radiative transition is influenced by the presence of matrix impurities and defects that can act as non-radiative recombination centers. Furthermore, the long lifetime of the $^4I_{13/2}$ metastable level makes the Er^{3+} emission sensitive to non-radiative decay processes, such as up-conversion [15, 16] and concentration quenching [8, 17].

Cross-section

The cross-section quantifies the probability of the transition between two states to occur with the concurrent emission or absorption of light. It has the dimensions of an area and can be intuitively seen as the target area that can intercept a light flux by catching the photons that flow through it. Since optical transitions in Er^{3+} have small probability, the cross-sections for optical excitation and stimulated emission are quite small, typically on the order of 10^{-19}-10^{-21} cm^2 depending on the host matrix [8, 9, 18]. This is one of the major limitations in the realization of photonic and optoelectronc devices with Er doped materials. In recent years, a lot of work has been carried out in order to overcome this barrier introducing in the matrix sensitizing species with higher absorption cross-section which can absorb light more efficiently and than transfer the energy to a nearby Er, increasing the pumping efficiency. Over the years different sensitizing strategies have been adopted, as for example coupling with other rare earth elements [19–21], Si nanoaggregates [22–27], organic complexes [28–32] and metal nanoclusters [33–39].

1.3 Er:SiO_2 cosputtered thin films

Erbium-doped silica (Er:SiO_2) films were synthesized co-deposition of Er and SiO_2 in a magnetron sputtering system. A metallic Erbium target was mounted on a magnetron Direct Current (DC) source while the SiO_2 target was placed on a magnetron Radio Frequency (RF) source. Two different sputtering gas were explored: pure Argon and a mixture of Ar and O_2 (95%Ar + 5%O_2), with the operating pressure set at 5x10^{-5}mbar. This is the lowest pressure to ensure that the plasma stays on and minimizes the re-sputtering phenomenon. Despite a notable lowering of the deposition rate, the reactive atmosphere has shown to prevent a slight oxygen understoichiometry which characterizes the silica doped films deposited in pure argon atmosphere and therefore was chosen as operating condition. The concentration of the dopant in the deposited film can be easily tailored varying the ratio between the input power of the two sources. To prevent the overheating of the sample during the deposition the power of the RF source power was fixed at 250 W, while the DC power was varied in the range 1-7 W. The Er concentrations varying from 6.6×10^{19} at./cm^3 to 1.65×10^{21} at/cm^3 were obtained. Er concentration was measured by Rutherford Backscattering Spectrometry (RBS), while the concentration profiles were obtained by Secondary Ion Mass Spectrometry (SIMS). During the depositions, the sample holder was rotated to ensure good homogeneity of the film composition and thickness. The depositions were performed at room temperature with no bias voltage on the sample holder. The Er concentration varies linearly with the power of the DC source. At fixed RF power the thickness of the deposited film has shown a linear dependence with the deposition time and no dependence on the DC power in the range 1-7 W. A list of the samples investigated in the present section is reported, together with the synthesis parameters, in Table 1.1.

Table 1.1: Sample synthesis parameters for the Er:SiO_2 co-sputtered films. The thickness was determined by profilometer measurements and Er concentration was estimated by RBS. Sample $D2_{Si}$ has the same synthesis parameter of the sample D2, but it was deposited on silicon substrate.

Sample	Film Thickness [nm]	DC power [W]	RF power [W]	Er conc. [at/cm^3]
D1	75 ± 3	1	250	6.6x10^{19}
D2	165 ± 3	2	250	3x10^{20}
D3	75 ± 3	3	250	6.7x10^{20}
D4	103 ± 3	5	250	1.17x10^{21}
D5	97 ± 3	7	250	1.65x10^{21}
$D2_{Si}$	165 ± 3	2	250	3x10^{20}

1.3.1 PL measurements

Photoluminescence (PL) spectroscopy measurements were used to optically characterize the Er doped silica films. PL measurements, both integrated and time resolved, were performed at room temperature by exciting the samples with a 6 Hz mechanically chopped continuous wavelength (CW) Argon laser. A schematic sketch of the experimental apparatus is shown in Fig (1.2). Both in-resonance (λ_{exc}=488 nm) and out-of resonance (λ_{exc}=476.5 nm) excitation conditions were employed. The excitation wavelength was selected by laser line filters and the maximum laser power at λ=488 nm was 16.2 mW, while at λ=476.5 nm was 2.5 mW.

The chopper was placed between two lenses (100 mm focal length) to reduce the laser beam spot dimension on the chopper plane to obtain a steeper open/close transition. Two converging lenses have been used to collect and bring the emitted radiation on the entrance slit of a single-grating monochromator. The luminescence signal was detected by a near-infrared photomultiplier tube cooled by liquid nitrogen (HAMAMATSU R5509-72) and acquired with a lock-in amplifier, using the chopper frequency as a reference. Time-resolved PL analyses were carried out by fixing the monochromator wavelength at 1.54 μm and collecting the PL intensity evolution as a function of time with a digital oscilloscope (Tektronix TDS 7104). The beam spot size on the sample was determined by the Knife-Edge method [40] and the measured diameter for both wavelength was 1.2 mm. For the photon flux measurements, the beam spot diameter was reduced down to 100 μm at the sample position using a converging lens.

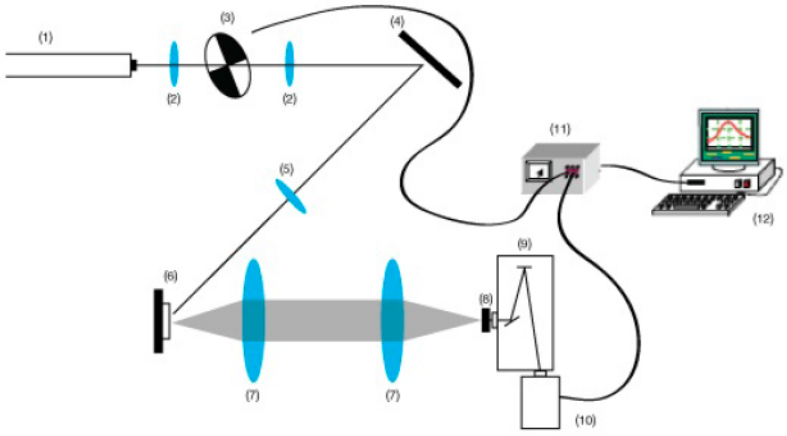

Figure 1.2: A schematic representation of the PL measurement set-up.

1.3.2 Er^{3+} emission spectrum

After the film deposition no detectable luminescence signal in the IR region has been obtained, probably due to the local disorder around Er ions. Dangling bonds and vacancies complexes as well as bond angle and length distortion in the silica network can, indeed, act as non-radiative de-excitation centres, quenching the Er^{3+} PL emission. As reported in the literature [41], annealing temperatures above 400 °C are required to recover host matrix defects and to restore the first shell of oxygen atoms surrounding the Er ions.

As an example, Fig1.3(a) shows a PL emission spectrum in the range 1450-1650 nm of a sample with Er concentration of 6.6×10^{19} at./cm^3 and film thickness of 75 nm (sample D1) after a thermal annealing at 900 °C for 2 hours in vacuum atmosphere (P<$2\text{x}10^{-5}$ mbar). The PL spectrum was obtained by excitation with the 488 nm line of the Ar laser, resonant with the $^4I_{15/2} \rightarrow ^4F_{7/2}$ transition. The emission connected with the Er^{3+} transition from the first excited state to the ground state ($^4I_{13/2} \rightarrow ^4I_{15/2}$) has a main peak located at 1540 nm (1), with a shoulder at 1500 nm (4) and two weak structures at longer wavelength (2, 3). The overall spectral width of the main peak (FWHM=47 nm) and the wide tails of the spectrum are the result of Stark splitting of the excited and ground states in the host electric field,

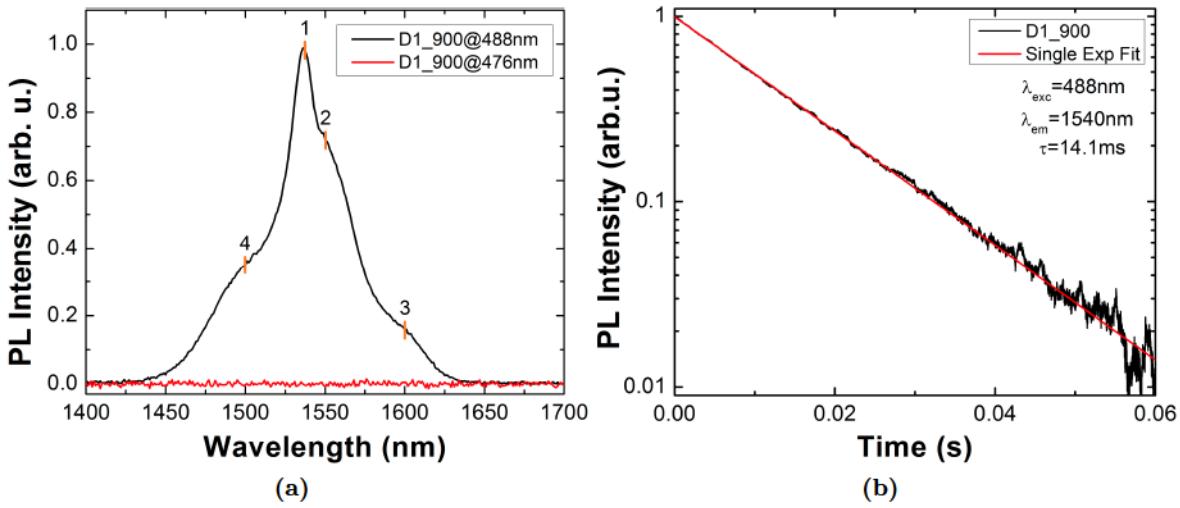

Figure 1.3: PL emission spectrum (a) and PL intensity decay curve (b) of the Er:SiO_2 co-sputtered sample D1 annealed at 900 ℃ for 2 hours in vacuum atmosphere. Sample excitation has been obtained by pumping with the 488 nm line Ar laser chopped at 6 Hz.

together with additional homogeneous and inhomogeneous broadening. Under non-resonant excitation at λ=476.5 nm no PL emission has been detected (red line in Fig 1.3(a)). In Fig. 1.3(b) PL intensity decay curve of the same sample is reported, with a single exponential fit ($I_{PL} = I_0 e^{t/\tau}$ - red line) of the curve the characteristic lifetime of the transition $^4I_{13/2} \rightarrow ^4 I_{15/2}$ can be calculated obtaining τ=14.1 ms. This value is in perfect agreement with the values reported in literature for the same Er concentration [8]. No difference in the lifetime values were found at different wavelengths corresponding to the structures 2, 3 and 4, present in the emission spectrum.

1.3.3 Thermal activation

The temperature and the atmosphere of the Er^{3+} activation annealing have a crucial role in restoring the defects in the deposited silica layer and in the promotion of the octahedral oxygen coordination around Er ions. Thus, a set of thermal treatments in air and vacuum atmosphere were performed in the 300–1000 ℃ temperature range to determine the optimum conditions for the maximization of both PL intensity and radiative lifetime of the characteristic transition at 1540 nm. In a simple picture the PL intensity (I_{PL}) can be described by the relation:

$$I_{PL} \propto N_{act}\eta, \tag{1.2}$$

where N_{act} is the concentration of optically active Er ions and η is the quantum efficiency of the luminescence process and it is given by:

$$\eta = \frac{\gamma_{rad}}{\gamma_{rad} + \gamma_{nr}} = \frac{\tau}{\tau_{rad}}, \tag{1.3}$$

with τ the measured lifetime and τ_{rad} the radiative lifetime of the transition $^4I_{13/2} \rightarrow ^4I_{15/2}$.

Fig. 1.4 shows the evolution of the PL intensity and the lifetime at λ=1540 nm under resonant excitation (λ=488 nm), as a function of the annealing temperature, of sample D2. For

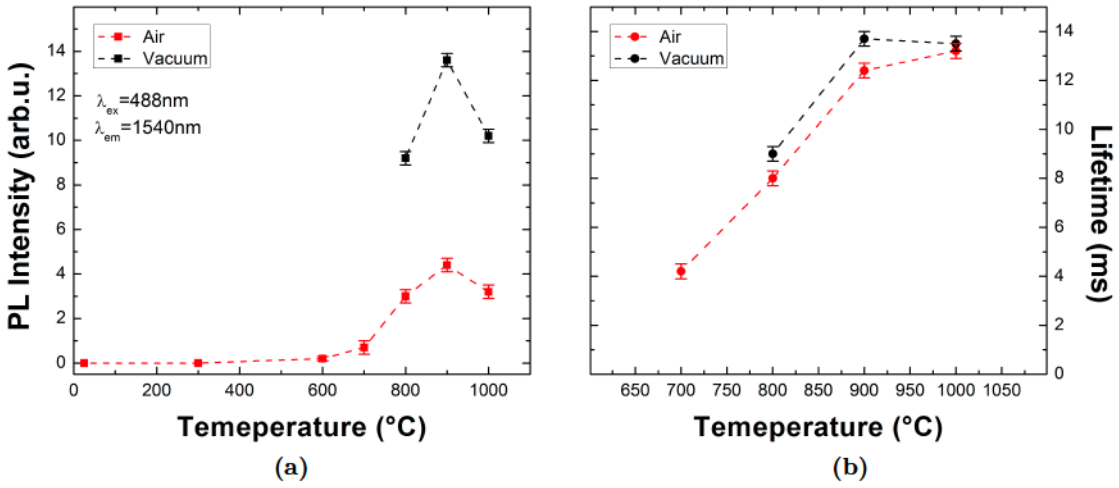

Figure 1.4: PL intensity (a) and lifetime values (b) at 1.54 μm of sample D2 as a function of the temperature for thermal treatments performed in air and vacuum atmosphere. The excitation wavelength was 488 nm. The measurements have been performed with a 16.2 mW Ar laser chopped at 6 Hz. The annealing duration was 1 h and 2 h for air and vacuum atmosphere, respectively.

both annealing atmospheres a similar trend was found. Below 600 °C no-measurable PL signal has been detected, while in the 600–900 °C range the intensity increases with the temperature reaching a maximum at 900 °C and falling off at higher temperatures. The lifetime, instead, increases in the whole range of explored temperatures, but more rapidly in the 600–800 °C interval and just slightly at higher temperatures. The increase of both PL intensity and lifetime up to 900 °C has to be attributed to the restoration of the configurational order in the silica matrix and the increase of the quantum efficiency of the radiative transition, Conversely above 900 °C the PL signal falls off probably because of the decrease of the number optically active Er ions due to the activation of the clustering phenomenon. It is worth noting that annealing in high vacuum (P$\sim 10^{-5}$ mbar) increases by more than 3 times the PL intensity with respect to air, suggesting a beneficial effect of the low pressure on the out-diffusion of quenching species (such as OH groups) from the deposited layer [42]. Hence, 900 °C in vacuum has been chosen as standard annealing condition for the activation of the Er^{3+} photoluminescence in the co-sputtered films.

1.3.4 Structural characterization

Structural characterizations of the doped films were performed by means of Transmission Electron Microscopy (TEM) and Extended X-ray Absorption Fine Structure (EXAFS) analyses. The first was performed to determine the quality of the deposited silica and to observe if the Er clustering phenomena took place in the deposited film upon the high temperature annealing, while EXAFS measurements offer the possibility to investigate the local environment of the Er ions embedded in the silica matrix. TEM analyses have been performed on a sample deposited on silicon substrate before and after a thermal annealing at 900 °C for 1 h in air (sample $D2_{Si}$ and $D2_{Si}$_900, Fig. 1.5). The thickness of the film before and after the thermal annealing was determined to be (165±5) nm and (185±5) nm, respectively. The increase of the film thickness after the thermal treatment can be attributed to the oxidation of the Si substrate, as evidenced also by SIMS elemental depth profiles. The thicknesses of the two

films are homogeneous. The as-sputtered sample does not present a columnar growth as can be seen in Fig.1.5(a) and it does not exhibit detectable porosity.

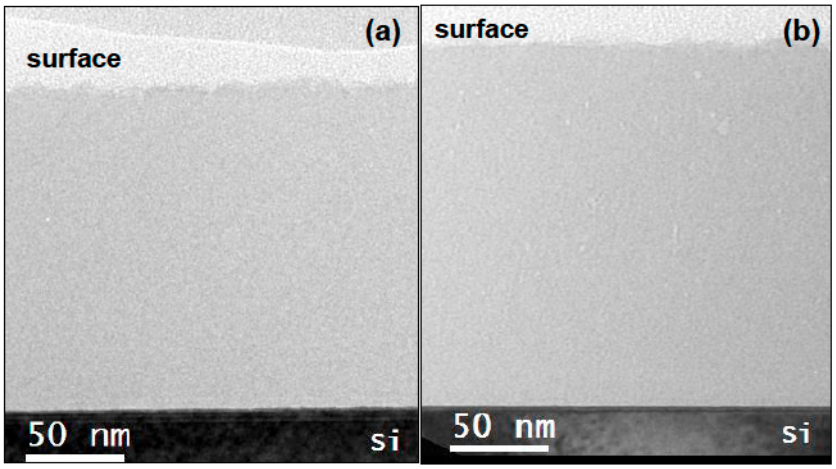

Figure 1.5: Bright-field TEM cross-sectional image of the sample $D2_{Si}$ before (a) and after (b) thermal annealing at 900 °C, 1 h in air ($D2_{Si}$_900).

From the HRTEM images (Fig.1.6(a)) the presence of a 2 nm thick native oxide layer can be seen on the interface between the deposited silica and the Si substrate. The thermally oxidized Si layer at the interface of the annealed sample cannot be distinguished from the Er-doped silica film indicating the good quality of the silica matrix upon annealing. It also interesting to note that there is no evidence of Er clustering phenomena after the 900 °C thermal treatment in air. The EDX compositional analysis confirms a uniform Er concentration over the entire film thickness.

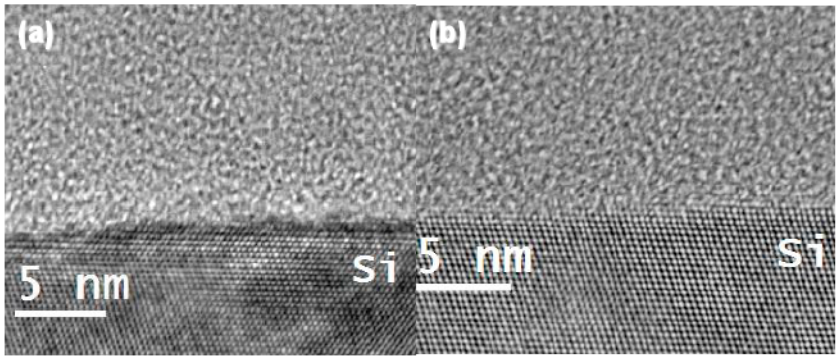

Figure 1.6: High-Resolution (HR) TEM image of the deposited film (a) before and (b) after air annealing near the Si interface. The lattice fringes of the crystalline Si substrate are well visible.

Er L_3-edge x-ray absorption spectra were recorded at the Italian beamline GILDA of the European Synchrotron Radiation Facility-ESRF in fluorescence mode. A grazing incidence geometry was used (incidence angle ~2 deg) to increase the fluorescence signal from Er, keeping at the same time the signal of the elastic scattering from the matrix as low as possible. The EXAFS analyses have been performed on sample D2 (see Table 1.1) annealed at two different conditions: 900 °C for 1 h in air (D2_900) and 900 °C for 1 h in air followed by an isochronal annealing at 1000 °C in air (D2_1000). The thickness of the film (165 nm) enables to have a

high signal to noise ratio in the EXAFS measurements.

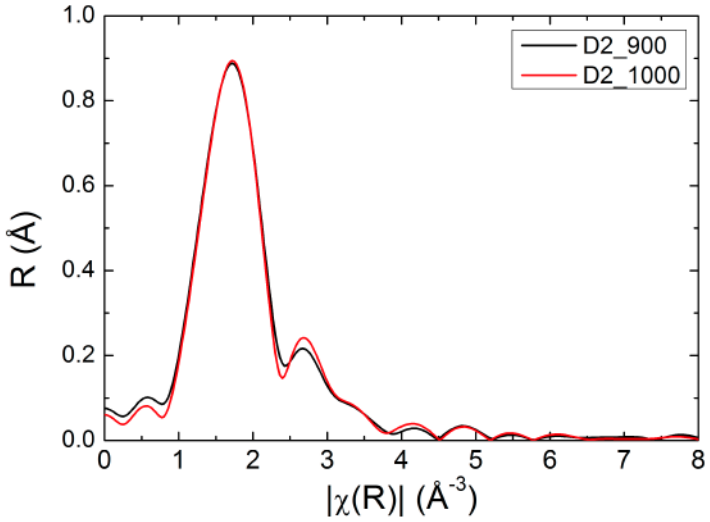

Figure 1.7: Comparison between the Fourier transform modulus of the EXAFS signal from the sample D2 annealed at 900 °C for 1 h in air (black line) and the sample D2 annealed at 900 °C for 1 h in air and subsequently for 1 h at 1000 °C in air (red line).

The EXAFS signals from all the measured samples are similar and exhibit one main oscillation that dumps down in the high-energy region of the spectrum: this feature, typical of a light backscatterer, is in this case related to the first shell of O atoms surrounding the Er ions. In Fig 1.7 the Fourier transform moduli of the EXAFS signals is reported. The peak is centered at ≈1.8 Å (first coordination shell). The quantitative analysis indicates that for both samples the coordination number of this O shell is about 6.5±1.1 and the Er-O distance is (2.24±0.02)Å; the Debye-Waller factor (σ^2) is (13±4)×10^{-3} Å^2. For comparison, in the Er_2O_3 crystal the first shell is formed by 6 O atoms at a distance of 2.24–2.27Å and the Debye-Waller factor is about one half of the value found here, indicating a more disordered Er site in the sputtered films. The observed Er-O distance, shorter than in the oxide, is in agreement with what has been found in similar systems ([43] and Refs. therein).

The EXAFS analysis is in good agreement with the PL intensity and lifetimes results. No appreciable difference in the local order of Erbium can be seen between the single thermal treatment at 900 °C 1h in air and the one at 900 °C 1h plus 1000 °C 1h in air. In conclusion, the annealing at 900 °C has been proven to be sufficient to restore the local order of the Erbium ion in a silica matrix for the co-sputtered system.

1.3.5 Er concentration

One of the major limitation to the realization of photonic devices based on Er-doped materials is the occurrence of concentration quenching phenomena. Concentration quenching is a manifestation of the Förster non-radiative energy-transfer phenomenon [44, 45], and it is characterized by the decrease in the luminescence quantum yield as the emitting species concentration is increased. Usually this model is presented in the context of donor-acceptor energy-transfer, where donor and acceptor are different species, but when the emitter satisfies the condition for the self-energy transfer (overlap of the excitation and emission spectra) energy can migrate through the material by a resonant interaction until a quenching center

is met [44]. For Er-doped silica, this migration will become more efficient at smaller Er-Er distances, hence at higher concentrations, but will only reduce the lifetime when the material contains impurities or defects that couple to an Er ion (e.g. OH impurities in Silica glass). The efficiency of the energy-transfer mechanism (k_t) is described by:

$$k_t = \frac{r^{-6}}{r^{-6} + {R_0}^{-6}}, \tag{1.4}$$

where r is the Er-Er separation distance and R_0 is the Förster radius. R_0 depends on the spectral overlap, the refractive index of the medium and the relative orientation of the emitters. Because of the rapid decay of the energy-transfer efficiency with increasing r, concentration quenching is significant only when r is less than or comparable to R_0. For Er in silica, the concentration limit when the separation distance between Er ions becomes comparable to the Förster radius is in the range 0.1-1 at%, depending on the matrix. [8, 9, 17].

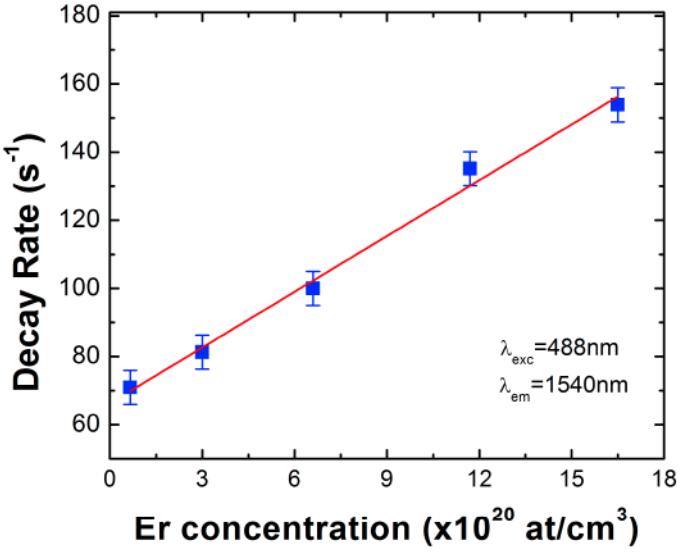

Figure 1.8: Decay rate of the transition ${}^4I_{13/2} \rightarrow {}^4I_{15/2}$ vs. Er concentration. The decay rate was measured under resonant excitation at λ=488 nm. The Er concentration measured with the RBS technique.

Since the control of Er^{3+} lifetime and the maximization of the quantum efficiency are of primary interest in the present work, a set of samples with increasing Er concentration has been prepared. The control on the Er concentration was obtained keeping fixed the power of the SiO_2 source and varying the power of the Erbium source in the range 1-7 W (cf. 1.1). All the samples were annealed at 900 °C for 2 h in vacuum, to ensure as previously discussed, the recovery of the matrix defects and minimize the OH concentration. As shown in the Fig. 1.8, the Er decay rate has a linear increase with the Er concentration. Moreover, all the samples are characterized by a single exponential decay, consistent with a homogeneous configurational distribution of Er ions in the co-sputtered film. In a simple model [17], the Er decay rate (Γ_{Er}) can be described by:

$$\Gamma_{Er} = C_{Er-Er}[d^*][Er], \tag{1.5}$$

where $[Er]$ is the Er concentration, $[d^*]$ is the concentration of non-radiative decay centers (mainly OH groups) and C_{Er-Er} is a coupling constant of the self-energy transfer of Er ions. Since there is no difference in the sample synthesis parameters nor in the thermal activation

process, $[d^*]$ can be considered constant obtaining the linear dependence of the decay rate with Er concentration as experimentally demonstrated.

1.3.6 Er^{3+} emission cross-section

The study of the emission cross-section is fundamental in the characterization of the optical properties of Er-doped systems. From the Fuchtbauer-Ladenberg equation, this parameter can be estimated when the fluorescent bandwidths, the spontaneous lifetime and the degeneracy of the excited and the ground state levels are known [46]. Being 1 and 2 the ground and the excited state of a two level system, the emission cross-section (σ_{21}) is given by:

$$\sigma_{21} = \frac{\lambda^2}{8\pi\mu^2} A_{21} g(\nu) \tag{1.6}$$

where λ is the wavelength of peak of emission, $g(\nu)$ is the line shape of the emission spectrum, A_{21} is the Einstein coefficient for spontaneous emission and μ is the refractive index of the host media. In absence of non-radiative decay channels, the Einstein coefficient for spontaneous emission becomes the measured decay rate ($A_{21}=1/\tau$). Since the line shape is in general not simple, the effective linewidth $\Delta\lambda_{eff}$ is defined through the relation

$$I_{pk}\Delta\lambda_{eff} = \int_0^\infty I(\lambda)d\lambda. \tag{1.7}$$

The line shape function may be written as

$$g(\nu) = \frac{I_{pk}}{\int I d\nu}, \tag{1.8}$$

so that:

$$g(\nu) = \frac{\lambda^2}{c}\frac{1}{\Delta\lambda_{eff}}. \tag{1.9}$$

The Fuchtbauer-Ladenberg equation becomes:

$$\sigma_{21} = \frac{\lambda^4}{8\pi\mu^2 c}\frac{1}{\tau\Delta\lambda_{eff}}. \tag{1.10}$$

From the spectrum reported in Fig 1.3(a) it is now possible to calculate the effective linewidth that results equal to 62.7 nm. The measured lifetime is 14.1 ms and can be considered completely radiative [8] The emission cross-section results $\sigma_{21}=4.1\times10^{-21}$ cm^2, in good agreement with the values reported in literature [8–11].

It is worth noting that the Fuchtbauer-Ladenberg equation is not the best approach to calculate the Er^{3+} emission cross-section since it assumes that all of the Stark components are equally populated. For rare earth embedded in a glassy matrix this is in general not exact since the populations are determined by the Boltzmann distribution. A more appropriate model to calculate the cross-section would be the McCumber approach [47], where the emission cross-section is calculated from the absorption cross-section and the radiative lifetime. Due to the low Er concentration and the small thickness of the Er-doped films, an accurate estimation of the absorption cross-section is very difficult. Nonetheless, as shown by Barnes et al. [46], the values calculated with the two approaches are of the same order of magnitude, so the value calculated with the Fuchtbauer-Ladenberg approach can be assumed as a good approximation.

1.4 Er implanted silica

A well known synthesis technique used to obtain thin doped layers in a glassy matrix is ion implantation. It offers several advantages, such as high control on the doping concentration, low temperature processing, variation of the dopant concentration profile without changing in the implantation fluence, overcoming of the solubility limit. Silica substrates (Herasil 1 by Heraeus; slide area of 7.5×2.5 cm) have been implanted at room temperature with an Er^+ ion beam at the Ion Implanation Facility of the Legnaro National Laboratories (Padova, Italy). An uniform doping of the silica matrix has been obtained performing sequential implantation at three different energies (50, 100, 190 keV), with current densities of about 0.05 $\mu A/cm^2$. A total fluence of 6.8×10^{14} Er^+/cm^2 was implanted as estimated by RBS measurements.

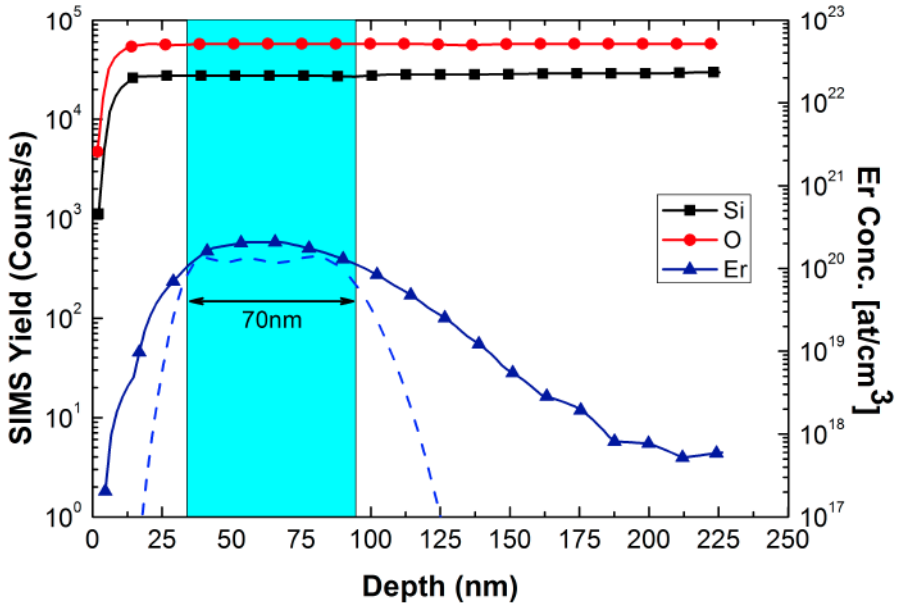

Figure 1.9: Elemental concentration profiles obtained by SIMS measurements on a silica glass implanted with Er and annealed at 800 °C in N_2 atmosphere for 1 h. Right scale reports the Er concentration estimated by RBS quantitative analysis. The dashed line represents the Er simulated concentration profile for the triple energy implantation scheme obtained with SRIM-2008 code [48].

An almost flat Er concentration profile in the implanted region is obtained with a plateau at 8.6×10^{19} at/cm^3 (Fig.1.9). The sample will be labelled I1 in the following. The Er concentration profile is centered at about 60 nm below the slab surface, the flat region is thick about 70 nm. The long tail of the Er concentration depth profile present in the SIMS curve has to be attributed to ion-intermixing induced by the measurement. It worth noting that for this sample the Er concentration is just above the concentration quenching limit which is of about 5×10^{19} at/cm^3 [44].

1.4.1 Erbium implanted silica: optical behaviour

As for the samples obtained with magnetron co-sputtering, no measurable PL emission has been obtained in the IR region for the Er-doped silica films after ion implantation. This is probably due to the radiation damage induced in the silica matrix during the implantation process. As already pointed out for co-sputtered samples, defects in the glassy matrix can

act as non-radiative centres for Er^{3+} de-excitation, quenching the PL signal. A thermal activation above 500 °C is required to recover the implantation damage in the silica matrix. As an example, Fig. 1.10(a) show the PL emission spectrum in the range 1400-1700 nm of sample I1 annealed at 800 °C in N_2, obtained by resonant excitation at λ=488 nm. The emission spectrum is peaked at 1541 nm and presents lineshape and FWHM similar to the D1 sample obtained with magnetron co-sputtering (see Fig.1.3), although the secondary peaks look less noticeable. As expected no PL signal arises under non-resonant excitation (λ=476.5 nm).

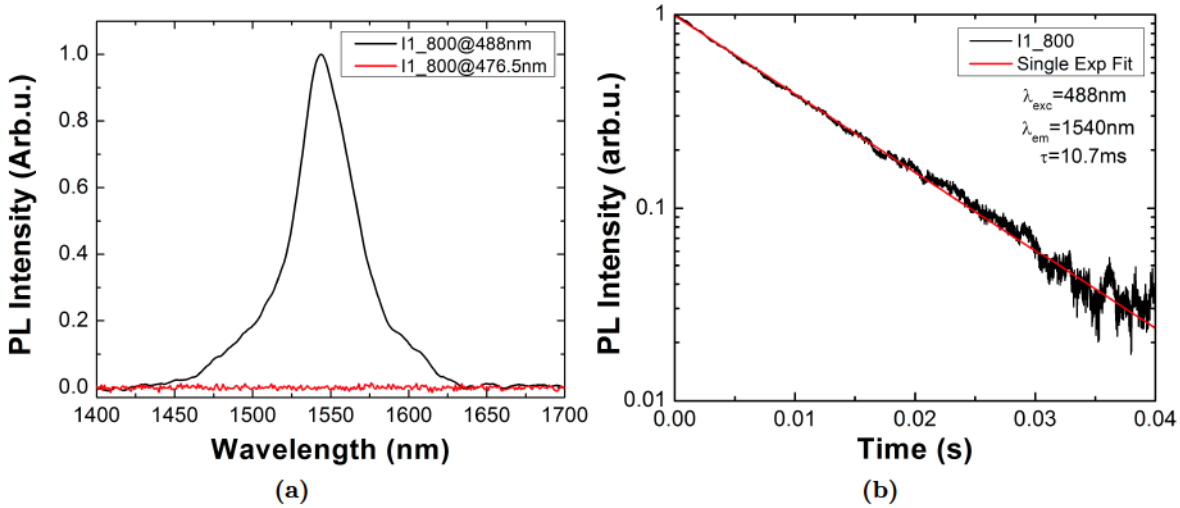

Figure 1.10: PL emission spectrum (a) and PL intensity decay (b) of sample I1 annealed at 800 °C 1 h in N_2.

It is interesting to analyse the PL dynamics characterizing the 1.54μm emission. From the PL decay curve of the sample I1_800 in Fig.1.10(b), it can be seen that the decay is purely exponential indicating a homogeneous population of emitting Er ions in silica. When the interaction of the excited species with the luminescence quenchers is distance indipendent, the de-excitation dynamics takes the form described by the Stern-Volmer model [49]:

$$I_{PL}(t) = I_{PL}(0)\mathbf{exp}(-\frac{t}{\tau}), \tag{1.11}$$

where $I_{PL}(0)$ is the PL intensity when the laser is switched off and the spontaneous lifetime τ corresponds to

$$\frac{1}{\tau} = \frac{1}{\tau_r} + \frac{1}{\tau_{nr}}, \tag{1.12}$$

with τ_r and τ_{nr} being respectively the radiative and non-radiative terms. The estimated lifetime (with single exponential fit) results τ=10.7 ms, slightly shorter than the one obtained for the co-sputtered sample D1_900, where the quantum efficiency approaches the unity. This difference may be attributed to the higher Er concentration of sample I1_800 that increases the probability of non-radiative decay and to the lower annealing temperature at 800 °C that probably was not sufficient to recover completely the ion implantation damage of the SiO_2 matrix.

1.4.2 Er activation: Thermal annealing

To evaluate the influence of annealing temperature and atmosphere on the optical properties of Er-implanted silica, two sets of isochronal (1h) thermal annealings have been carried out on the I1 sample. The first one has been performed in the 300-1100 °C temperature range in air, while the second set has been performed in N_2 flux exploring the 300-1000 °C temperature range. The PL intensity signal at 1540 nm as a function of the treatment temperature is plotted in Fig. 1.11. For both annealing atmospheres it has been found a similar trend: below 600 °C no measurable PL signal has been detected, while in the 600-900 °C range the PL intensity increases with the temperature reaching a maximum at 900 °C. Above this temperature the PL intensity falls off noticeably in both cases.

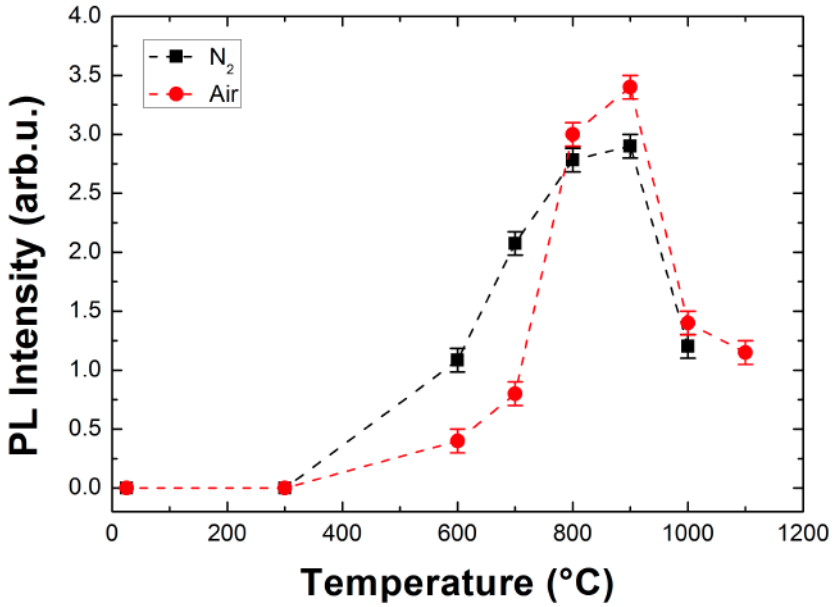

Figure 1.11: PL intensity at 1.54 μm of samples I1 as a function of the thermal annealing temperature. The annealing has been performed in a conventional furnace in air (red dots) and in N_2 (black squares) atmosphere for 1 h.

Fig.1.12 shows the radiative lifetime at 1540 nm under resonant Er^{3+} excitation, as a function of tthe annealing temperature for the samples thermally treated in air and in N_2 atmosphere. Regardless of the thermal treatment atmosphere, the lifetime increases continuously with the temperature, but more rapidly at low temperatures and just slightly above 900 °C. For all the measured samples a purely exponential PL intensity decay has been found, indicating a homogeneous configurational population of Er ions in the implanted layer.

It is interesting to note that the temperature at which the maximum of the PL intensity occurs is the same for the implanted and the co-sputtered samples. Even if the damage in the silica has a different origin, the temperature required for the recovery of the matrix is in both cases 900 °C and the mechanism proposed for the co-sputtered Er-doped silica samples can be applied also to the Er-implanted silica ones. Indeed, the increase of the PL intensity observed in the 600-900 °C is probably due to the increase of the Er^{3+} quantum efficiency due to the decrease in the number of silica matrix defects induced by the ion implantation process. Moreover, starting from 1000 °C the fall of the PL intensity can be attributed to the onset of an Er clustering phenomenon that decreases the concentration of Er^{3+} active ions. The

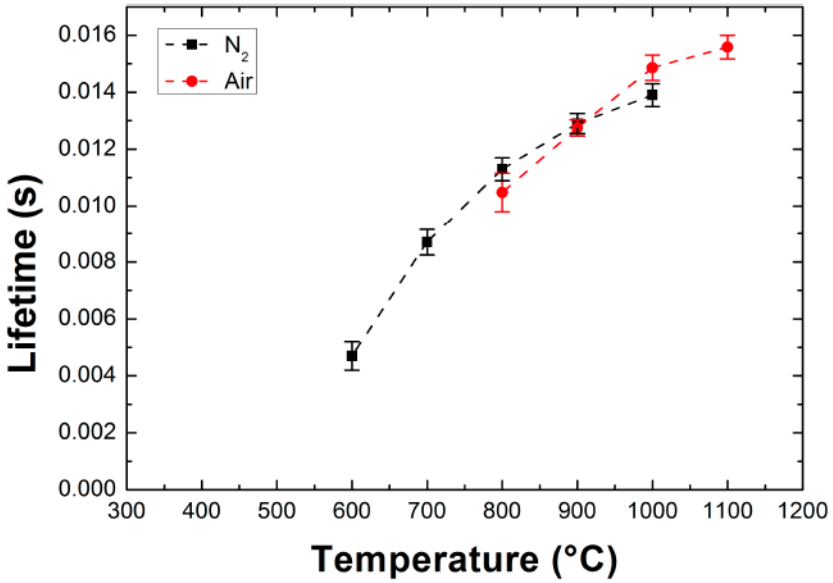

Figure 1.12: PL lifetime values at 1.54 μm for samples I1 as a function of the temperature for the thermal treatments performed in air and in N_2 atmosphere with a duration of 1 h. Sample excitation has been done by pumping with the 488 nm line Ar laser chopped at 6 Hz.

clustering phenomenon does not influence the lifetime that sightly increases due to a further recovery of matrix defects.

In the 600-700 °C temperature range, the N_2 atmosphere is more efficient on increasing the PL intensity, but the short values of the lifetime indicate that many non-radiative processes still take place in the samples. Conversely, in the 800-1000 °C temperature range the PL intensity of the samples annealed in air is slightly higher (I_{PL-air} ~1.2×I_{PL-N_2}). Since the difference in the measured lifetime for I1 samples annealed in two different atmospheres is smaller than the experimental accuracy, it emerges that the annealing atmosphere does not play a crucial role for the Er^{3+} PL emission of Er-implanted silica films.

1.5 Conclusions

It has been demonstrated that magnetron co-sputtering and ion implantation can be used as versatile techniques for the synthesis of Er doped silica thin films. No measurable PL signal in the IR region has been detected on the as-deposited and as-implanted samples, due the high amount of matrix defects that act as non-radiative centers for Er de-excitation. Exploring the trend of the PL intensity and the lifetime as a function of annealing temperature, it has been found that for both synthesis techniques a thermal treatment in the range 800–900 °C was necessary to maximize the PL intensity and minimize the non-radiative decay rate. The structural characterization performed with EXAFS and TEM measurements have pointed out that these annealing contritions are sufficient to promote the oxygen octahedral coordination around the Er ions and have excluded the occurrence of Er clustering processes. Moreover, it has been observed a beneficial effect of the vacuum atmosphere during the Er thermal activation of the co-sputtered samples, due to the enhanced out-diffusion of quenching species from the deposited layer. The occurrence of concentration quenching has been observed in the range 10^{19}–10^{21} Er/cm^3; the decay rate at 1540 nm increases linearly with the Er

concentration. Finally, a value of 4.1×10^{-21} cm^2 for the Er^{3+} excitation cross-section was determined through the Fuchtbauer-Ladenberg approach.

2 Modification of Er^{3+} radiative lifetime by interaction with thin films

2.1 Introduction

As already pointed out in the previous chapter, the long lifetime of characteristic transition $^4I_{13/2} \rightarrow ^4I_{15/2}$ of Er ions embedded in a glassy matrix is one of the major limitation in the realization of photonic and optoeletronic devices based on Er-doped materials, because the long permanence of the ion in the excited state makes it prone to non-radiative decay processes such as energy migration, cooperative up-conversion and concentration quenching. Since the early work of Purcell [4] it is known that the change in the local photonic density of state (LDOS) may influence the decay rate of an emitter. The presence of an interface in close proximity of an emitter ($d<\lambda$) can be seen as the simplest way to influence the local photonic density of states and thus, change the dynamics of the emission. A pioneering work of Drexhage and co-workers [50–54] has first demonstrated experimentally the influence of a silver mirror on the spontaneous emission of Eu^{3+} ions as a function of distance. More recently, a considerable amount of work has been carried out on the modification of spontaneous emission in the presence of a reflecting surface [55–57], however these systems are characterized by the presence of an emitting sources with an intrinsic high quantum efficiency (e.g., quantum dots).

The aim of the present chapter is to study the modification of Er^{3+} spontaneous emission in Er:SiO_2 thin layers (obtained by magnetron co-sputtering) by the interaction with thin films with different dielectric function. Moreover, the possibility of the coupling between the emitted radiation and surface plasmon polaritons (SPPs) on the metal-dielectric interface at the Er emission wavelength (λ=1540nm) is explored. A comparison between experiment and theory is also presented, showing that an excellent control on the radiative properties of Er ions has been achieved.

2.2 Theoretical model

The photoluminescence (PL) can be seen as the typical spontaneous emission process. The spontaneous transition decay rate ($\Gamma_{i,j}$) between an excited state (i) and a lower energy state (j) is given by the Fermi's golden role [58]

$$\Gamma_{i,j} = \frac{2\pi}{\hbar}|M_{i,j}|^2\rho_j, \tag{2.1}$$

where $M_{i,j}$ is a matrix element that connects the excited and lower energy levels and is determined by the wavefunctions associated with those levels; ρ_j is the density of states of the optical field at the transition frequency, hereafter referred to as the local photonic density of states (LDOS). Thus, the probability of the radiative transition can be modified acting on the LDOS as pointed out first by Purcell at Radio Frequency (RF) wavelengths in 1946 [4]. The presence of an interface in close proximity of an emitter will, in principle,

modify both the LDOS and the matrix element of the transition between the excited state and the ground state, but the wavefunctions will be influence only if the atoms of the interface are the closest neighbours (d∼1 Å). Even if the spontaneous emission can be considered as an archetypal quantum mechanical process where the LDOS is seen essentially as vacuum fluctuations, in a classical viewpoint it can be interpreted as the ability of the surrounding structure to support the emitted photons. One may expect that these two approaches are explanations in different regimes, on the contrary they are complementary explanations which provide the same quantitative answer [59]. The equivalence of the classical model and a full quantum-mechanical calculation has been established by Yeung and Gustafson [60].

In the classical viewpoint, the emitter is indeed considered as a forced damped dipole oscillator and the influence of the surface is taken into account by determining the total electromagnetic field acting on the dipole, including the dipole back-reflected field from the surface. The distance between the emitter and the surface is a crucial parameter for controlling the emitter lifetime, since the amplitude and the phase of the reflected field will determine whether the emission rate will be enhanced or suppressed. Moreover, a more complete description of the phenomenon must take into account that the emitter can loose energy via energy transfer to the interface (i.e. coupling with surface plasmon polaritons (SPPs) and lossy surface waves) [59]. The comprehensive analytical solution of the problem was first given by Chance, Prock and Silbey in 1975 [61]. They have followed two different approaches for the determination of the variation of the lifetime of an emitter close to an interface. The first one calculates the reflected electric field at the dipole position, while the second one uses the energy flux method. The result are equivalent but the second approach enables also to distinguish between the radiative and the non-radiative decay rate.

The purpose of this section is to present briefly the model proposed by Chance, Prock and Silbey ("CPS model" in the following) for an emitting dipole near an interface [62]. The emitter is considered as a forced damped dipole oscillator, which equation of the motion can be written as:

$$\frac{d^2\mu}{dt^2} + \omega^2\mu = \frac{e}{m}E_R - \gamma_0\frac{d\mu}{dt}, \tag{2.2}$$

where μ is the dipole momentum, ω is the oscillation frequency in the absence of all damping, m is the effective mass of the dipole, e the electric charge, E_R is the reflected field at the dipole position and γ_0 is the damping constant (decay rate) in the absence of the reflecting surface. The dipole moment (μ) and the reflected field (E_R) oscillate with the same (complex) frequency :

$$\mu = \mu_0 e^{-i[\omega+\Delta\omega]t} e^{-\gamma t/2}, \tag{2.3}$$

and

$$E_R = E_0 e^{-i[\omega+\Delta\omega]t} e^{-\gamma t/2}, \tag{2.4}$$

where $\Delta\omega$ and γ are the frequency shift and the decay rate in the presence of an interface, respectively. Substituting equations (2.3) and (2.4) into (2.2) and recognizing that γ^2 and the magnitude of the term $(e^2/\mu_0 m)E_0$ are very small compared to ω^2 [63], we have

$$\Delta\omega = \frac{\gamma^2}{8\omega} + \left[\frac{e^2}{2\mu_0 m\omega}\right]\mathbf{Re}(E_0), \tag{2.5}$$

$$\gamma = \gamma_0 + \left[\frac{e^2}{2\mu_0 m\omega}\right]\mathbf{Im}(E_0). \tag{2.6}$$

The frequency shift ($\Delta\omega$) is found to be quite small [62]. From equation (2.6) it is clear that the change of the decay rate of an emitter close to an interface is dictated by the out-of-phase component of the reflected field. The problem reduces now in the calculation of the reflected electric field at the dipole position which has been the topic of many interesting works, most of them uses the Hertz vector potential or the Green's Dyadic function [64]. Once the reflected field is determined (omitted here for brevity), the decay rate for any dipole orientation can be derived from the combination of perpendicular (γ_t) or parallel (γ_p) dipole components with respect to the interface:

$$\gamma_t = \gamma_0 \left\{ 1 - \frac{3}{2}\mathbf{Im}\left[\int_0^\infty R_p \frac{u^3}{a_1} \mathbf{exp}(-4\pi n_1 a_1 z/\lambda) du \right] \right\}, \tag{2.7}$$

$$\gamma_p = \gamma_0 \left\{ 1 + \frac{3}{4}\mathbf{Im}\left[\int_0^\infty \left[(1-u^2)R_p + R_t \right] \frac{u}{a_1} \mathbf{exp}(-4\pi n_1 a_1 z/\lambda) du \right] \right\}, \tag{2.8}$$

where the integration variable u is the component of the wave-vector (of the dipole field) in the plane of the interface, normalized with respect to the far-field wave-vector k_1 of the dipole radiation field in medium 1 embedding the emitter ($u = k_x/k_1$), n_1 is its refractive index, z is the distance of the emitter from the interface, λ the emitting wavelength. The parameter $a_1 = -i\sqrt{1-u^2}$ is related to the perpendicular component of the wave-vector at the interface, while R_p and R_t are the Fresnel coefficients for p- and s-polarized light at the interface respectively, evaluated as a function of u and can be expressed as:

$$R_t = \frac{a_1 - a_2}{a_1 + a_2}, \qquad R_p = \frac{\varepsilon_1 a_2 - \varepsilon_2 a_1}{\varepsilon_1 a_2 + \varepsilon_2 a_1}, \tag{2.9}$$

with ε_1 being the dielectric function of the surrounding medium of the emitter, ε_2 the complex dielectric function of the medium beyond the interface and $a_2 = -i\sqrt{\varepsilon_2/\varepsilon_1 - u^2}$.

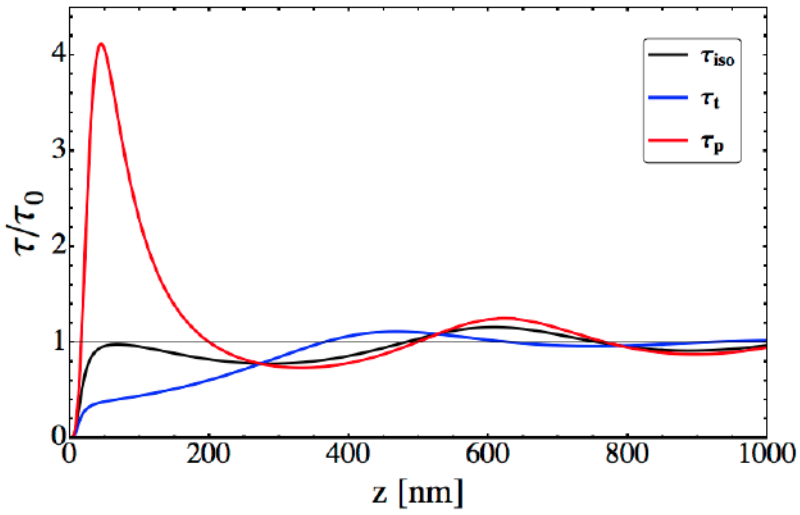

Figure 2.1: Variation of normalized lifetime as a function of the distance (z) from a Ag overlayer (ε_2=-115.75+9.60i) for an Er-like emitter (λ_{em}=1540 nm) embedded in silica. Parallel, perpendicular and isotropic orientation are obtained from eq. 2.8, 2.7 and 2.10, respectively.

Since the normalized wave-vector u may range over all positive values between 0 and infinity, the reflection coefficients have to be calculated for both real and complex angles of incidence,

which correspond to incident waves that are propagating and evanescent respectively. When the dipoles have an isotropic or random orientation configurations with respect to the interface, the decay rate (γ^{iso}) takes the form:

$$\gamma_{iso} = \frac{1}{\tau} = \frac{2}{3}\gamma_p + \frac{1}{3}\gamma_t = \frac{2}{3}\tau_p + \frac{1}{3}\tau_t \tag{2.10}$$

As an example, in Fig. (2.1) is reported the lifetime variation of an emitter ($\lambda_{em} = 1540$ nm) in front of a silver mirror as a function of the distance for the interface. The lifetime oscillates with increasing distance from the interface since the phase of the reflected field changes with the distance, the amplitude of this oscillation decrease at higher distances because the strength of the field emitted from the dipole (and thus the reflected field) fades with increasing distance from it. Furthermore, from Fig. (2.1) it can be noted that at small distances the lifetime is strongly reduced due to the coupling with surface plasmon polaritons and dissipation at the metal-dielectric interface.

2.3 Sample Synthesis

Since the study of the modification of the lifetime of the characteristic Er^{3+} emission at 1540 nm due to the proximity of an interface requires high control over the distances between the emitter and the interface, magnetron sputtering has been chosen as synthesis technique for Er:SiO_2 thin films. In this way not only the thickness of the doped layer can be tailored as required but also the distance between the Er:SiO_2 film and the interface can be controlled just switching off the Er sputtering source and depositing pure silica which acts as a spacer. The difference in the refractive index of pure and low-concentration Er-doped silica is negligible. Two different Er concentrations have been explored: 0.1% at. and 1.1% at. The first one below the concentration quenching limit [8], while the second one is at the threshold where the concentration quenching decreases the Er quantum efficiency. The films were deposited on 1 mm thick silica slides (HSQ300 by Heraeus). Before the deposition, silica substrates were cleaned in a "piranha" solution (30%H_2O_2, 70% H_2SO_4) for 20 min and copiously rinsed with Milli-Q water (18 MΩ resistivity). Prior to silica and Erbium co-deposition, a 75 nm thick buffer layer of pure silica was deposited. During the depositions, the sample holder was rotated to have a good homogeneity of the film composition and thickness. Er concentration was measured by Rutherford Backscattering Spectrometry (RBS), while the concentration profile was obtained by SIMS measurements. In order to restore the matrix defects induced during the Er:SiO_2 film deposition and activate the Er^{3+} luminescence at 1.54 μm, the samples were annealed for 2 hours at 900 °C in vacuum atmosphere (P$\sim 10^{-5}$ mbar). Er ions diffuse minimally under these conditions, as checked by SIMS. Photoluminescence measurements, both integrated and time resolved, were performed at room temperature by exciting the samples with a 6 Hz mechanically chopped cw Ar laser. Both in-resonance (λ_{exc}=488 nm) and out-of resonance (λ_{exc}=476.5 nm) excitation conditions were employed. The PL signal was analysed by a single grating monochromator and detected by a near-infrared photomultiplier tube cooled by liquid nitrogen. The time-resolved PL analysis was carried out by fixing the detected wavelength at 1540 nm and collecting the PL intensity evolution as a function of the time with a digital oscilloscope (Tektronix TDS 7104). As expected, no PL signal has been detected under non-resonant excitation at λ=476.5 nm.

Table 2.1: Sample synthesis parameters and measured lifetimes of the reference samples (S1, S2 and S3)

Sample	Film Thickness [nm]	Er conc. % at.	SiO_2 Spacer [nm]	Annealing °C	Lifetime [ms]
S1	75 ± 3	1.1	-	900	10.0 ± 0.2
S2	85 ± 4	0.1	-	900	13.0 ± 0.2
S3	20 ± 2	0.1	250	900	10.4 ± 0.2

From Table 1 can be immediately noted that sample S2 and S3, with identical Er concentration have τ=13 ms and τ=10.4 ms, respectively. Since the annealing conditions are the same, the only difference between the two samples is the distance of the Er-doped layer from the surface, therefore it is clear that not only absorbing media may influence the radiative lifetime of Er^{3+} ions but also the effect of "air interface" has to be taken into account since it plays a minor but detectable role in the modification of τ.

2.4 Calculation of Er^{3+} lifetime with the CPS model

In order to apply the model proposed by Chance, Prock and Silbey (CPS) to Er:SiO_2 thin films some important clarifications have to be done. Since the dipole moment of Er^{3+} ions in silica would have no preferred orientation, the dipole orientation with respect to the interface can be consider random, thus the equation (2.7) and (2.8) can be substituted into (2.10) obtaining the expression of the radiative decay rate (γ_r^{iso}) of a single emitter as a function of the distance (z) from the interface:

$$\gamma_{iso}^r(z) = \gamma_0^r \left\{ 1 + \frac{1}{2}\mathbf{Im} \int_0^\infty \left[-R_p \frac{u^3}{a_1} + \left((1-u^2)R_p + R_t \right) \frac{u}{a_1} \right] \mathbf{exp}(-4\pi n_1 a_1 z/\lambda) du \right\}, \tag{2.11}$$

whit γ_0^r the radiative decay rate in the medium without an interface [1].

The experimentally measured decay rate (Γ_0) can be considered as the sum of a radiative (Γ_0^r) and a non-radiative (Γ_0^{nr}) contribution, with the latter being unaffected by the presence of the interface. Since the Er-doped film has a finite thickness, the Er distribution in the film has to be taken into account. From SIMS measurements we have observed that Er diffusion during the thermal annealing is negligible, thus the Er concentration profile has been approximated with the characteristic function:

$$f(z) = \begin{cases} f_0, z \in [z_0, z_0 + z_{Er}] \\ 0, z \notin [z_0, z_0 + z_{Er}] \end{cases} \tag{2.12}$$

with z_0=z_{min} being the distance of the Er:SiO_2 film from the interface, z_{Er} the thickness of Er:SiO_2 film (so that the maximum distance of Er is z_{max}=z_0+z_{Er}) and f_0 the (constant) Er concentration.

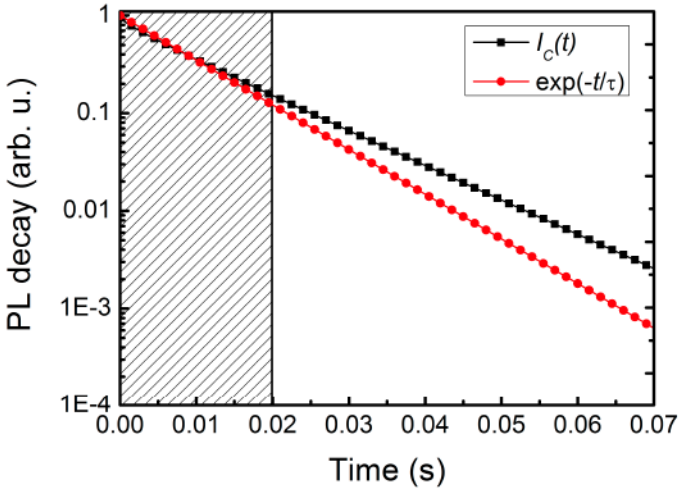

Figure 2.2: PL intensity time dependence. Comparison between the time dependence of the PL intensity calculated according to equation (2.13) and a single exponential decay

[1] In the following the notation γ_a^b stands for a single emitter (dipole), while Γ_a^b stands for the decay rate of a distribution of emitters (i.e. Er ions).

The time dependence of the PL intensity $I_{PL}(t)$ is therefore calculated as:

$$I_{PL}(t) = I_0 \int_0^{\infty} f(z) e^{-\gamma^r_{iso}(z)t} dz = I_0 f_0 \int_{z_{min}}^{z_{max}} e^{-\gamma^r_{iso}(z)t} dz \tag{2.13}$$

where γ^r_{iso} is the decay rate for an emitter at a distance z from the interface and I_0 the stationary emission intensity. Since the dependency is slightly non-exponential, following the approach of Bao et al. [65], we have determined the radiative decay rate ($\Gamma^r_{iso,calc}$) fitting the first 20 ms (where the agreement is quite satisfactory) of the normalized computed function with a single exponential curve (see Fig. (2.2)). Keeping constant the non-radiative decay rate (Γ^{nr}_0), the calculated Er lifetime becomes τ_{calc}=$1/(\Gamma^r_{iso,calc}+\Gamma^{nr}_0)$.

2.4.1 Radiative and non-radiative lifetime in Er:SiO_2

To determine the radiative (τ^r_0) and non-radiative lifetime (τ^{nr}_0) of the reference sample, the measured lifetime values listed in Table 2.1 have to be evaluated taking into account the distance from the surface of the Er-doped layer. It's worth noting that the presence of a dielectric medium, with no complex component of the dielectric function, will influence just the radiative lifetime of an emitter in close proximity of the dielectric-dielectric interface, since the dissipative contribution (SPPs and so called lossy surface waves) is governed by the complex part of the dielectric function. At a low Er concentration, the decay rate (Γ_0) of the $^4I_{13/2} \rightarrow ^4 I_{15/2}$ transition in a relaxed SiO_2 lattice is 70 s^{-1} (τ^r_0=14.2 ms) and it is mainly due to radiative emission (Γ_0=Γ^r_0) [8]. Using this value in the equation (2.11) and following the procedure described in the previous section (with ε_2=ε_{air}=1), the radiative decay rate Γ^r_{calc} can be obtained for the three reference sample. The difference between the experimental value ($\Gamma_{exp} = 1/\tau_{exp}$) and the calculated one is the non-radiative decay rate Γ^{nr}. (see Table 2.2).

Table 2.2: Radiative and non-radiative decay rate of the $^4I_{13/2} \rightarrow ^4 I_{15/2}$ transition for the reference samples. The influence of the distance from air-SiO_2 interface is evaluated with the model described in the text. Radiative efficiency is also reported

Sample	Γ^r_0 [s^{-1}]	$\Gamma^r_{iso,calc}$ [s^{-1}]	Γ_{exp} [s^{-1}]	Γ^{nr} [s^{-1}]	Radiative efficiency
S1	70	55.1	100 ± 3	44.9	0.55
S2	70	55.6	76.9 ± 3	21.3	0.72
S3	70	65.9	96.2 ± 4	30.3	0.68

Moreover, the radiative efficiency (q) can be evaluated from the calculated and experimental decay rates in the following way:

$$q = \frac{\Gamma^r}{\Gamma^r + \Gamma^{nr}} = \frac{\Gamma^r_{iso,calc}}{\Gamma_{exp}}. \tag{2.14}$$

Sample S1 has the highest non-radiative decay rate due to the high Er concentration, above the concentration quenching limit. Despite the equal Er concentration and the similar synthesis parameters, sample S2 and S3 present slightly different radiative efficiency (Δq ~4%); this can be likely attributed to the presence of some residual defects in the thicker silica deposited film (~270 nm) acting as non-radiative decay centres and not completely recovered during the thermal annealing performed to activate the Er ions.

2.5 Metallic overlayer

The modification of the lifetime of the transition $^4I_{13/2} \rightarrow ^4 I_{15/2}$ for Er^{3+} emission at 1540 nm has been studied for four different metallic films. It has been chosen to work with 2 plasmonic metals (i.e., Au or Ag) and with Cr or Ti. After the thermal activation process (900 °C 2 h in vacuum), the optically thick (t>200 nm) metallic films were deposited on sample S1 via magnetron sputtering (see Fig. 2.3).

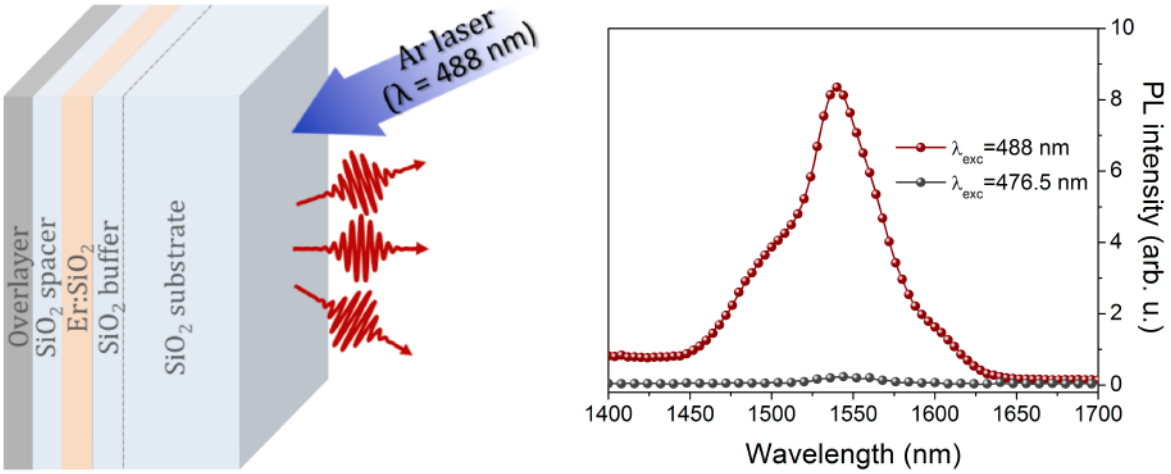

Figure 2.3: (a) Schematic representation of the structure of the samples and their orientation during photoluminescence measurements. (b) Typical Er^{3+} PL spectra of the samples measured at 1540 nm under resonant (λ_{exc}=488 nm) and out-of-resonance (λ_{exc}=476.5 nm) excitation conditions.

All film thicknesses were measured both with an atomic force microscope (NT-MDT Solver-Pro AFM) and a profilometer. Since a precise value of the dielectric function at 1540 nm of the metal film was necessary to compare the experimental results with the calculations, instead of using the values present in literature (such as [66, 67]), the dielectric functions were determined by means of a VASE of J. A. Woollam Co. spectroscopic ellipsometer. PL spectrum of the samples was obtained at room temperature (RT) by resonant excitation with the 488 nm line of a continuous-wave (CW) Ar laser, exhibiting the characteristic PL emission at 1540 nm related to the Er^{3+} $^4I_{13/2} \rightarrow ^4I_{15/2}$ transition in silica. No difference in the peak position was noticed after the metal deposition. Furthermore, under non-resonant excitation at 476.5 nm no measurable PL signal at 1540 nm has been detected, indicating no occurrence of energy-transfer mechanisms towards Er ions in the presence of the metallic overlayers (see Fig(2.3)).

Fig. (2.4) shows the PL decay curves of samples S1 with the different indicated overlayers, measured under resonant excitation conditions (λ_{exc}= 488 nm). All PL decay curves are characterized by a single exponential behaviour that has been fitted to determine the experimental Er lifetimes (see Table 2.3). Figure (2.4) clearly shows the effect on the shortening of the Er^{3+} lifetime for the characteristic emission at 1540 nm due to the close proximity of a metallic overlayer to the Er-doped 75 nm thick film. Samples with gold ($S1_{Au}$) and silver ($S1_{Ag}$) overlayer exhibit a reduction in the measured lifetime of about 1/2 of the value of the reference sample (S1), while samples with chromium and titanium films present a more pronounced

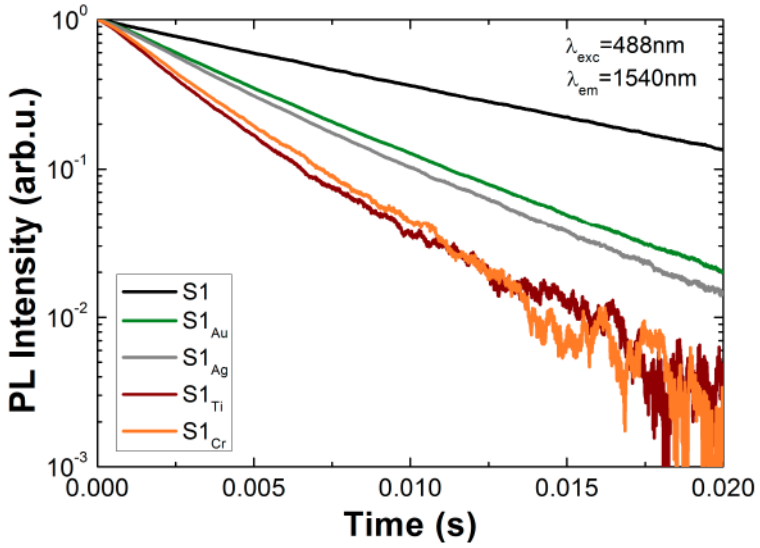

Figure 2.4: Room temperature PL decay measurements at 1540 nm performed under resonant excitation conditions of samples S1 with Au, Ag, Cr and Ti overlayers.

lifetime shortening, especially sample $S1_{Ti}$ that has τ_{exp}=2.9 ms. To better understand this lifetime variation the experimentally measured values were compared with those calculated with the CPS model and the obtained values are listed in Table 2.3. In general good agreement between the measured values and the calculated ones were found, especially for the $S1_{Ti}$ and $S1_{Cr}$ samples where the adhesion between the sputtered film and the silica substrate is strong. Since the quality of the interface has a primary importance in the interaction between the emitter and the metallic overlayer, it is reasonable assuming that the difference of about 1.5ms between the calculated and experimentally obtained values for the samples $S1_{Au}$ and $S1_{Ag}$ can be attributed to the well-known poor adhesion of the noble metals films on the Er:SiO_2 film. This will be shown in the next section.

Table 2.3: Samples characteristics and PL decay results. ε_{OL} is the dielectric function of the metallic films measured at λ=1540 nm by spectroscopic ellipsometry. In the last two columns the comparison between the experimentally Er lifetime measured at 1540nm (resonant excitation at λ=488 nm) and the value calculated according to the model described in the text is reported.

Sample	Er:SiO_2 film thickness [nm]	ε_{OL} (λ=1540nm)	τ_{exp} [ms]	τ_{calc} [ms]
S1	75 ± 3	1	10 ± 0.2	-
$S1_{Au}$	75 ± 3	-128.35 + 11.75 i	5.2 ± 0.3	6.7
$S1_{Ag}$	75 ± 3	-103.21 + 11.12 i	5.0 ± 0.4	6.3
$S1_{Ti}$	75 ± 3	2.427 + 29.59 i	2.9 ± 0.2	2.8
$S1_{Cr}$	75 ± 3	-6.37 + 41.16 i	3.3 ± 0.2	3.2

Improving the quality of the noble metal-SiO_2 interface

To better evaluate the difference between the experimentally measured lifetimes and the calculated values for the samples $S1_{Au}$ and $S1_{Ag}$, on the reference sample S2 (with higher radiative

efficiency) was deposited by magnetron sputtering a silver and a gold 250 nm thick films. To promote the adhesion and improve the quality of the interface between SiO_2 and the noble metal films, a thermal annealing at 250 °C for 2 hours in vacuum (P$\sim 10^{-5}$ mbar) was performed. Vacuum has been chosen to avoid possible oxidative reaction especially on silver film. The reference sample S2 was also annealed to verify that the "low" temperature annealing do not influence the optical properties of the Er:SiO_2 layer; as expected no difference has been detected in the measured lifetime before and after the annealing on sample S2. The dielectric function of the noble metal films were measured at 1540nm after the annealing by spectroscopic ellipsometry and the values are almost coincident with the one obtained for $S1_{Au}$ and $S1_{Ag}$ samples (cf. Table 2.3 and Table 2.4), demonstrating that no oxidation reaction has occurred during the annealing.

Table 2.4: Samples characteristics and PL decay results. ε_{OL} is the dielectric function of the metallic films measured at λ=1540 nm by spectroscopic ellipsometry. In the last two columns the comparison between the experimentally Er lifetime measured at 1540 nm (resonant excitation at λ=488 nm) and the value calculated according to the model described in the text is reported.

Sample	**Er:SiO_2 film thickness [nm]**	ε_{OL} **(λ=1540nm)**	τ_{exp} **[ms]**	τ_{calc} **[ms]**
S2	85 ± 3	1	13 ± 0.2	-
$S2_{Au}$	85 ± 3	-116.91 + 9.73i	8.5 ± 0.4	8.1
$S2_{Ag}$	85 ± 3	-115.75 + 9.60i	8.4 ± 0.4	8.1

As can the seen from Table (2.4), a much better agreement on the lifetime variation is now obtained, and the calculated values are in an almost perfect agreement with the measured ones. The fact that again no PL signal has been obtained from non-resonant excitation (λ=476.5 nm) can be considered as a proof that no diffusion and clustering of noble metal atoms in the Er-doped film has occurred, since Au and Ag sub-nanometric clusters are well-known sensitizers for Er-doped silica [36, 39].

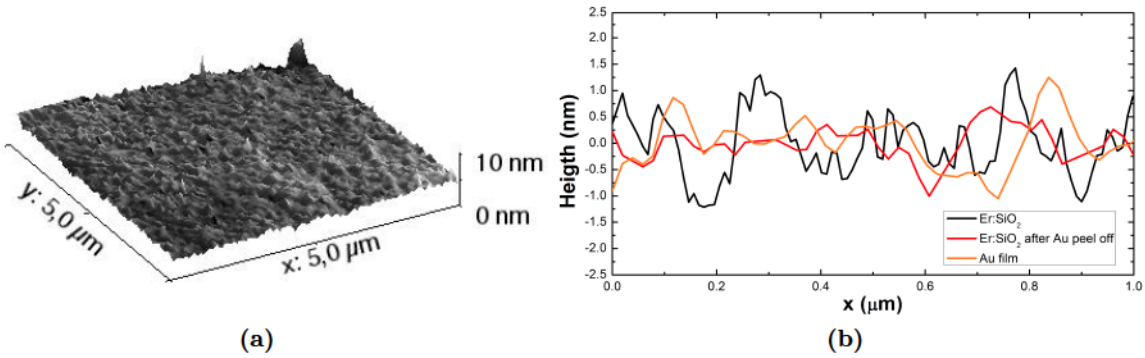

Figure 2.5: (a) AFM tomography of the Er:SiO_2 surface after the peel off of the gold film. (b) Roughness profile determined by AFM measurements of the Er:SiO_2 surface before the Au deposition and after the Au film peel off. The roughness of the Au peeled off film is also reported.

Moreover, the quality of the interface was also determined by means of AFM, measuring the roughness of the Er:SiO_2 deposited film and the same surface after the gold film deposition, a thermal annealing (250 °C for 4 h in Vacuum atmosphere) and the peel off of the film. In both

cases the roughness average ($R_a = \frac{1}{n}\sum_{i=1}^{n}|h_i|$) was found to be less than 1 nm (see figure (2.5)). The roughness of a peeled Au film was also determined to be less than 1 nm. Furthermore, the Er^{3+} lifetime was measured again on the $S2_{Au}$ sample after the peel off of the gold thin film and the τ_{exp} was found to be 12.9 ms, in perfect agreement with the S2 reference sample (13 ms). Hence any influence on the Er:SiO_2 film surface, structure and composition due to metal deposition can be excluded.

2.5.1 Intermediate distance range

As shown in Fig. (2.6) the oscillation of the lifetime as a function of the distance from a silver overlayer presents a minimum at a distance of about 260nm from the interface.

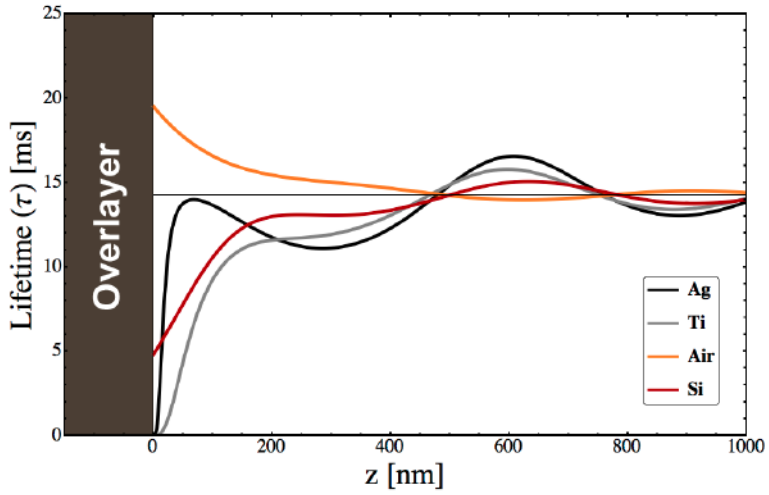

Figure 2.6: Theoretical dependence of Er^{3+} emission lifetimes in silica as a function of the distance z from a silver, air, silicon, titanium interface. The curve calculated with a gold surface overlaps to the silver one and it has not been reported.

At this distance the coupling of the emitted radiation with lossy surface waves (LSW) becomes weak and the shortening of the radiative lifetime can be attributed almost exclusively to the excitation of SPPs and the variation of photonic density of states due to the reflection of the emitted field on the silver interface (see figure (2.10)). To explore experimentally this phenomenon, on the sample S3 (where the thickness of the Er:SiO_2 was reduced down to 20 nm and a pure silica 250 nm thick film was deposited on top) a silver optically thick layer was deposited by magnetron sputtering and then thermally annealing at 250 °C for 2 hours in vacuum was performed to promote the adhesion of the noble metal film on the silica (ε_{Ag}=-115.75+9.60i). The lifetime measured under resonant excitation at λ=488 nm shows a significant reduction of 2.4 ms (τ_{exp}=8.0 ms) compared to the reference sample S3. Once more, the value is in perfect agreement with the lifetime calculated with the CPS model, showing that high control on the Er^{3+} lifetime can be achieved changing both the dielectric constant of the overlayer or the distance from the interface.

Table 2.5: S3 and $S3_{Ag}$ synthesis parameters with experimentally measured and calculated lifetimes.

Sample	Er:SiO_2 film thickness [nm]	SiO_2 spacer thickness [nm]	ε_{OL} (λ=1540nm)	τ_{exp} [ms]	τ_{calc} [ms]
S3	20 ± 1	250	1	10.4 ± 0.2	-
$S3_{Ag}$	20 ± 1	250	-115.75 + 9.60 i	8.0 ± 0.4	8.3

2.6 Semiconducting overlayer

After the investigation of the variation of the lifetime of the transition ${}^4I_{13/2} \rightarrow {}^4I_{15/2}$ of Er^{3+} ions embedded in silica matrix due to the presence of air and metallic interface, it is interesting now to evaluate also how the presence of a semiconductor interface will affect the lifetime of Er-doped thin films. The natural choice has been silicon. It has also the peculiar property of being (at 1.5 μm) a good reflector due to the high difference in the real part of the dielectric function, but a very weak absorber because of the almost null component of the complex term of the dielectric function at λ=1540 nm (ε_{Si}=12.09+8×10^{-6} i). To this purpose, a sample (named $S1_{Si}$) with the same synthesis characteristic of the sample S1 (Er conc.=1.1 at.%, Er:SiO_2 thickness=75 nm) was deposited on a silicon wafer with a silica spacer of 75 nm. The sample was annealed as well-established at 900 °C for 2 hours in vacuum atmosphere. The Er^{3+} radiative lifetime was shortened of about 2 ms with respect to the reference sample.

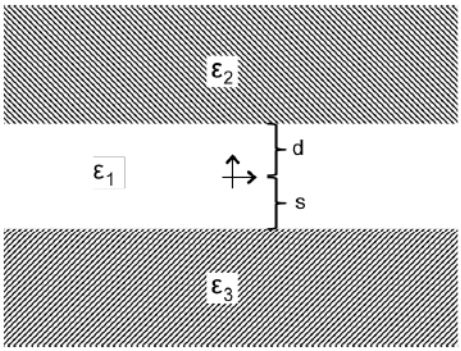

Figure 2.7: Geometry of the two interface problem, where d and s are the distances from the overlayer with dielectric function ε_2 and ε_3, respectively.

Since the Er-doped layer on the sample $S1_{Si}$ is placed between a double interface (air on one side and silicon on the other) the equation 2.11 doesn't hold any more. Omitting for brevity the details on the calculation, with the same procedure described for a single interface, Chance, Miller, Prock and Silbey [68] have derived the following equation that predicts the decay rate of a single emitter with perpendicular (γ_t) and parallel (γ_p) orientations with respect to the two interfaces (as in Fig. 2.7):

$$\gamma_t(d,s) = \gamma_0 \frac{3}{2} \mathbf{Im}\left[\int_0^\infty \frac{F(d,-R_p^{1,2})F(s,-R_p^{1,3})}{F(d+s,-R_p^{1,2}R_p^{1,3})}\frac{u^3}{a_1}du\right], \tag{2.15}$$

$$\gamma_p(d,s) = \gamma_0 \frac{3}{4} \mathbf{Im}\left[\int_0^\infty \frac{F(d,R_t^{1,2})F(s,R_t^{1,3})}{F(d+s,-R_t^{1,2}R_t^{1,3})}\frac{u}{a_1} + \frac{F(d,R_p^{1,2})F(s,R_p^{1,3})}{F(d+s,-R_p^{1,2}R_p^{1,3})}(1-u^2)du\right], \tag{2.16}$$

where $F(x,y) = 1 + y\ \mathbf{exp}(-4\pi n_1 a_1 x/\lambda)$, d and s being the distance from the interface 2 and 3 respectively (see Fig. (2.7)). The reflection coefficient are defined like those in (2.9):

$$R_t^{i,j} = \frac{a_i - a_j}{a_i + a_j}, \qquad R_p^{i,j} = \frac{\varepsilon_i a_j - \varepsilon_j a_i}{\varepsilon_i a_j + \varepsilon_j a_i}, \tag{2.17}$$

and $a_k = -i(\varepsilon_k/\varepsilon_1 - u^2)^{1/2}$. Once more, since Er ions do not have a preferential orientation with respect to the interface, the isotropic orientation configuration takes the form described by equation 2.10.

Since the total thickness of the deposited film is 150 nm (75 nm of Er:SiO_2 plus 75 nm of silica spacer), we can express the distance from the air overlayer as: s=150 − d; thus γ_{iso} becomes function of one variable and it is possible to evaluate τ_{calc} following the procedure described in section 2.4. The value of Γ_0^r and Γ_0^{nr} are the ones determined for sample S1 (see Table 2.2). As can be seen from Table 2.6, the experimental and the calculated values are in almost perfect agreement showing not only that the theoretical model presented by CPS can be applied to semiconductor interfaces but also that the lifetime shortening of Er:SiO_2 can be obtained by the presence of a semiconducting interface.

Table 2.6: S1 and $S1_{Si}$ synthesis parameters with experimentally measured and calculated lifetimes.

Sample	Er:SiO_2 film thickness [nm]	SiO_2 spacer thickness [nm]	ε_2 (λ=1540nm)	ε_3	τ_{exp} [ms]	τ_{calc} [ms]
S1	75 ± 3	-	1	-	10 ± 0.2	-
$S1_{Si}$	75 ± 2	75 ± 2	12.09+8x10^{-6} i	1	8.2 ± 0.4	8.5

2.7 The choice of an optimum overlayer - Re[ε_{OL}], Im[ε_{OL}] maps

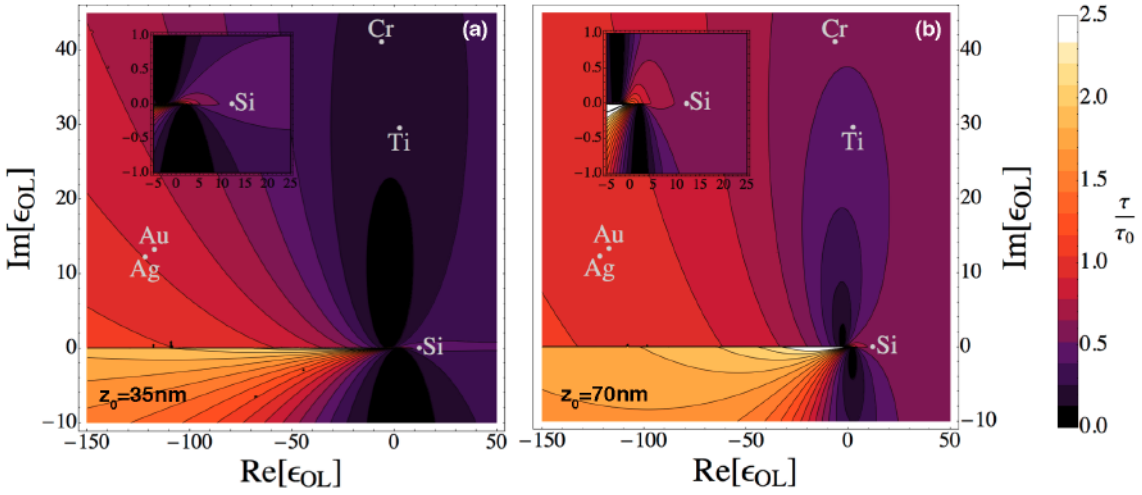

Figure 2.8: Normalized lifetime variation as a function of the real and imaginary component of the dielectric function of the overlayer for z_0=35nm (a) and z_0=70nm (b). The inset shows an enlarged view of the region around the origin.

After exploring both experimentally and theoretically the variation of the lifetime due to the presence of a dielectric (air), metallic (Au, Ag, Ti and Cr) and semiconducting (Si) overlayers,

it is possible now to generalize the model presented in the text and to draw a contour plot where at a fixed distance from the interface (z_0) the variation of the normalized lifetime (τ/τ_0) can be evaluated as a function of the real ($Re[\varepsilon_{OL}]$,) and the imaginary part ($Im[\varepsilon_{OL}]$) of the complex dielectric function of the overlayer. These maps can be an useful tool to predict the variation of the decay rate and to choose the optimum overlayer material.

2.8 Power dissipation and radiative efficiency with a noble metal overlayer

It is interesting now to try to separate the different pathways in which the decay can occur for an excited Er^{3+} close to an interface (i.e. radiative, SPP and non-radiative modes). Considering a geometry with an infinitely extended plane above the emitter ($z>z_0$) and another below the emitter ($0<z<z_0$, being z_0 the distance of the emitter from the overlayer), and calculating the energy flux through these two planes a rigorous separation between the energy flowing away by far-field radiation ($F_\uparrow$) and the energy transferred to the interface ($F_\downarrow$) can be given. The flux through each plane is obtained by integrating the normal component of the complex Poynting vector (S^*) over the plane [62].

Dividing then the energy flux by the total energy radiated by the dipole, the probabilities of the two mechanisms ($\gamma_\uparrow$, $\gamma_\downarrow$) are given by:

$$\gamma_\uparrow(z) = \Gamma_0^r \left\{ 1 + \frac{1}{2}\mathbf{Im} \int_0^1 \left[-R_p \frac{u^3}{a_1} + ((1-u^2)R_p + R_t)\frac{u}{a_1}) \right] \mathbf{exp}(-4\pi n_1 a_1 z/\lambda) du \right\}, \quad (2.18)$$

$$\gamma_\downarrow(z) = \Gamma_0^r \left\{ \frac{1}{2}\mathbf{Im} \int_1^\infty \left[-R_p \frac{u^3}{a_1} + ((1-u^2)R_p + R_t)\frac{u}{a_1}) \right] \mathbf{exp}(-4\pi n_1 a_1 z/\lambda) du \right\}, \quad (2.19)$$

Of course:

$$\gamma_\uparrow(z) + \gamma_\downarrow(z) = \gamma_{iso}^r(z) \quad (2.20)$$

As a first approximation, $\gamma_\uparrow$ may be seen as radiative decay rate (γ^r) and $\gamma_\downarrow$ as non-radiative decay rate (γ^{nr}). It is now possible to calculate the so called far-field radiative efficiency (q_F), that describe how many photons couples directly to far-field radiation divided by the total energy emitted by the dipole. As a function of the distance from the interface (z), the far-field efficiency is given by:

$$q_F(z) = \frac{\gamma^r(z)}{\gamma^r(z) + \gamma^{nr}(z)} = \frac{\gamma_\uparrow(z)}{\gamma_\uparrow(z) + \gamma_\downarrow(z)}. \quad (2.21)$$

q_F is not the actual radiative efficiency of the emitter since the contribution of surface plasmon polaritons is considered as non-radiative decay channels because they are seen as energy dissipated in the plane below the emitter, although SPPs are indeed EM modes propagating on the metal-dielectric interface that can be coupled out into far-field radiation or can re-excite the Er^{3+} ion that are located close to the interface and therefore contribute to the total emitted radiation [69].

Thus, to look in depth on how the energy goes away from an excited dipole, it is worth considering more in detail the near-field, a zone that extends roughly a distance λ_{em} from the emitter. In this way it is possible to evaluate how the electromagnetic power is radiated away from the emitter. The near-field emitted from a dipole contains components with a

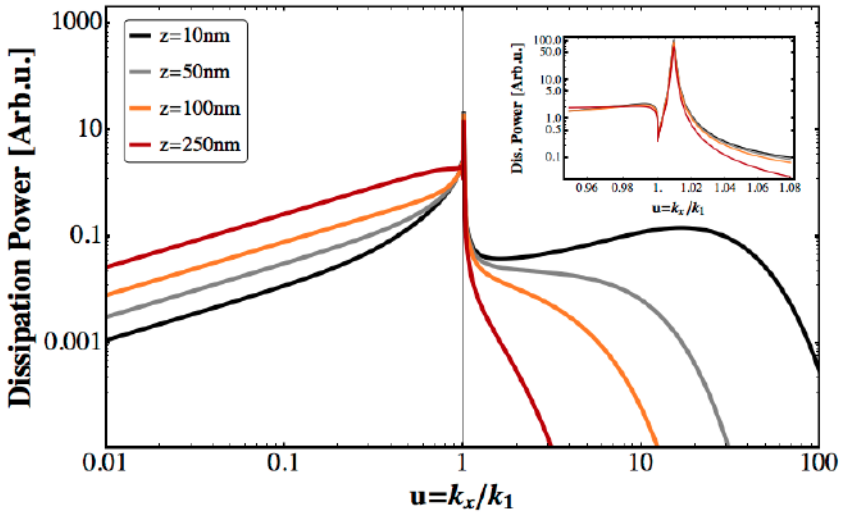

Figure 2.9: Power dissipation as a function of the normalized wave-vector u for an emitter (λ_{em}=1540nm) embedded in silica in front of a silver film. In the inset enlarges the region around the light line (u=1) to evidence the peak arising from the SPPs coupling.

large range of wave-vectors k, but only the components with $k<k_1$ (i.e., $u<1$) will propagate directly into the far-field (with k_1 being the far-field wave-vector in the media embedding the dipole). Importantly, for a dipole located near to a planar surface, a wide range of k_x also exists (k_x being the wave-vector in the plane of the surface), the dipole emitted radiation can couple to modes having in-plane momenta greater than k_1, such as SPPs in case of metal interface, modes that are not accessible to incident plane waves.

As pointed out by Ford and Weber in [70] the power dissipated by a dipole in the presence of a metal interface can be seen as the sum of three different contributions:

$$P = P_{photon} + P_{SPP} + P_{LSW} \tag{2.22}$$

where P_{photon} is the power radiated via photons, P_{SPP} via surface plasmon polaritons and P_{LSW} that via so called lossy surface waves. For a randomly oriented emitter, at a given distance from the interface (z) the power dissipation spectrum can be obtained plotting the imaginary part of the integrand in equation (2.11) as a function of the normalized wave-vector $u=k_x/k_1$ (see Fig (2.9) for a silver overlayer) [59].

In Fig. (2.9) three different regions corresponding to the different power contribution can be distinguished:

- in the region $0\leq u\leq 1$ the emitter couples to far-field propagating waves (P_{photon}), the value of u gives the direction of emission;
- just above the light line there is a narrow peak which corresponds to surface plasmon emission (P_{SPP}). The energy radiated from the emitter couples with SPPs on the metal dielectric interface. However, the process is still radiative in nature, since the energy is carried away by wave propagating along the surface. No loss in the metal is required for this process to occur [70];
- at $u\gg 1$, for small z, a broad peak associated with lossy surface waves arises (P_{LSW}).

The non-radiative decay is caused by the oscillating near-field of the dipole which induces electronic charge density oscillations that dissipate through scattering in the substrate.

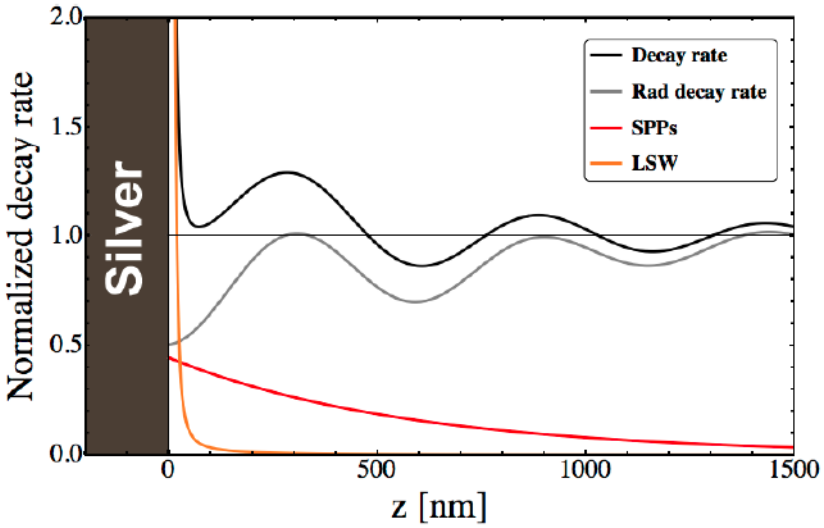

Figure 2.10: Modification of the decay rate for an emitter with $\lambda_{em} = 1540nm$ embedded in silica as a function of the distance from a silver overlayer (ε=-115.75+9.60 i). The total decay rate rate is split up into the three decay channels (i.e., radiative, SPPs modes and LSW.)

As an example, in Fig. (2.10) the different components of the normalized decay rate are plotted for an Er-like emitter (λ_{em}=1540nm) embedded in silica in front of a silver film (ε=-115.75+9.60 i). At small distances ($0<z<\lambda/50$) the non-radiative contribution due to the coupling with LSW is dominant. When the distance from the surface increases, LSW contribution becomes negligible, SPPs modes and local density of states fluctuation are responsible for the variation of the spontaneous emission lifetime. The coupling with SPPs modes fades with the distance from the overlayer but it is appreciable to a distance almost equal to the λ_{em}, showing how Er ions can efficiently couple to the Ag/SiO_2 interface when the distance between Er:SiO_2 and noble metal interface is optimized.

In order to quantify the SPP modes contribution (γ_{SPP}) to the total decay rate, the sharp peak just above the light line has to be integrated as a function of u (see Fig. 2.9). As a result, also the contribution of the lossy surface waves (γ_{LSW}) can be determined as follows:

$$\gamma_{LSW} = \gamma_{nr} - \gamma_{SPP}, \tag{2.23}$$

and the near-field radiative efficiency (q_F^*) is given by:

$$q_F^*(z) = \frac{\gamma_r + \gamma_{SPP}}{\gamma_r + \gamma_{SPP} + \gamma_{LSW}} \tag{2.24}$$

The two radiative efficiencies q_F e q_F^* can be seen as limiting cases. In an ideal case where all the energy associated with the surface plasmons can be coupled-out (either by Er^{3+} re-excitation or by the engineering the overlayer geometry), γ_{SPP} can be considered as an actual radiative decay channel also in the far-field [71].

Accounting the Er depth distribution ($f(z)$) as described in section 2.4, Γ_r, Γ_{SPP} and Γ_{LSW} can be calculated for an Er:SiO_2 thin film with a noble metal overlayer. The near-field and far-field radiative efficiency for the samples $S2_{Ag}$, $S2_{Au}$ and $S3_{Ag}$ are reported in Table 2.7.

Table 2.7: The values of Γ_r, Γ_{SPP}, Γ_{LSW} and a comparison of the radiative efficiency calculated with (2.19) and with (2.24) are reported for the sample $S2_{Ag}$, $S2_{Au}$ and $S3_{Ag}$

Sample	$\Gamma_r[s^{-1}]$	$\Gamma_{SPP}[s^{-1}]$	$\Gamma_{LSW}[s^{-1}]$	q_F	q_F^*
$S2_{Ag}$	38.6	27.5	35.6	0.38	0.65
$S2_{Au}$	38.7	27.2	35.5	0.38	0.65
$S3_{Ag}$	69.4	19.3	0.9	0.77	0.99

From the values listed in Table 2.7, it is clear that the SPP contribution is considerable in all the samples under study and that at Erbium emission wavelength no difference are appreciable between Au and Ag optically thick films. Remarkably, the near-field radiative efficiency (q_F^*) in the sample $S3_{Ag}$ reaches the 99% with a significant reduction of Er^{3+} lifetime.

2.9 Conclusions

The enhancement of Erbium radiative decay rate has been proven for four different metallic and a semiconductor overlayer, showing that a good control over the radiative properties of Erbium ions can be achieved acting on the distance between Er:SiO_2 film and the interface. A reduction up to 1/3 of the initial value of Erbium lifetime was observed due to the interaction with a Ti and Cr films. Moreover, for all the different overlayers the variation is in good agreement with a model that takes into account variations in the local density of states, excitation of surface plasmons and lossy surface waves. Thus, the efficient coupling between Er emission and propagating surface plasmons at the SiO_2–noble metal interface has been proven, showing that if the SPPs can be efficiently coupled out, the radiative efficiency of the Er^{3+} transition at 1540nm can be strongly enhanced.

3 Control of Erbium emission lifetime at 1540 nm by interaction with Nano Hole Arrays

3.1 Introduction

In the study of the variation of the Er^{3+} decay rate at 1540 nm due to the presence in close proximity of a metallic interface, it has been found that Er radiative emission can efficiently couple with SPP modes on the noble metal-silica interface. This coupling can significantly shorten the lifetime reducing the permanence of the ion in the excited state and thus the probability of non-radiative recombinations. The challenge still remains to couple out as efficiently as possible the surface plasmons in the far field radiation. One possible solution to the problem comes from plasmonic nanostructures that, due to the electromagnetic field confinement and the near-field enhancement, can in principle enhance the luminescent properties of emitters placed in close proximity. In recent years, a lot of work has been carried out on the interaction between an emitter and a plasmonic nanoparticle showing how the enhancement or the quenching of the luminescence is function of the distance from the nanoparticle [7]. Surprisingly, the Nanohole Array-emitter interaction, instead, has still to be deeply investigated and only few works are present in literature [?, ?, ?, ?, ?, ?]. The peculiar feature that makes them attractive for enhancement of the Er^{3+} PL emission at 1540 nm is the extraordinary optical transmission (EOT). EOT relates to the possibility of obtaining a huge enhancement in the light transmitted through an ordered array of sub-wavelength holes drilled in a otherwise totally opaque metallic film. EOT can be exploited in nanophotonics when resonantly coupled to the emission wavelength of the emitter so that a remarkable change of the local density of states (LDOS) can occur with a related possibility to change the quantum efficiency of the emitter. Moreover, SPPs modes propagating on the NHA-dielectric interface can couple out in far-field radiation without the use of prisms or additional gratings (i.e., NHA is itself a 2D grating). In the present chapter the Er^{3+}-NHA interaction will be investigated both experimentally and with finite element method (FEM) simulations, studying the lifetime variation as a function of NHA optical properties and the separation distance.

3.2 Surface plasmons

Due to the high absorption in the visible range, for long time the use of metals in the photonic field was limited; nonetheless in the last decades, metal structures have gain more and more importance because of their unique ability to confine light at length scales smaller than the wavelength. This peculiar feature emerges from the possibility of excitating surface plasmons that can confine electromagnetic fields over dimensions on the order of or smaller than the wavelength. The interaction processes between electromagnetic radiation and conduction

electrons at metallic interfaces or in small metallic nanostructures induces the enhancement of the optical near-field of sub-wavelength dimension [3].

Two different kind of surface plasmons have to be distinguish: Surface Plasmon Polaritons (SPPs) and Localized Surface Plasmons (LSPs).

Surface plasmon polaritons

When electromagnetic radiation couples with the oscillations of the electron plasma, electromagnetic surface waves may be excited. This is only possible at the interface between two materials with opposite sign in the real part of their dielectric function (e.g., a metal and an insulator). The excited wave is in this case trapped at the interface, evanescently confined in the perpendicular direction. The resulting excitations are called Surface Plasmon Polaritons. Due to the confinement of the radiation in sub-wavelength dimensions, the field is strongly enhanced at the interface.
The coupling of light with SPPs can be described starting from the wave equation:

$$\nabla^2\mathbf{E} - \frac{\varepsilon}{c^2}\frac{\partial^2\mathbf{E}}{\partial t^2} = 0. \tag{3.1}$$

Assuming a harmonic dependence of the field $\mathbf{E}$ (i.e., $\mathbf{E}(\mathbf{r},t) = \mathbf{E}(\mathbf{r})\,e^{-i\omega t}$) the Helmholtz equation can be written:

$$\nabla^2\mathbf{E} + k_0^2\varepsilon\mathbf{E} = 0, \tag{3.2}$$

where $k_0 = \omega/c$ is the wave-vector of the propagating radiation in vacuum. The simplest geometry sustaining SPPs is a single flat interface (placed at $z{=}0$) between a dielectric, non-absorbing half space ($z{>}0$) with positive real dielectric constant (ε_d) and an adjacent conducting half space ($z{<}0$) described by a dielectric function $\varepsilon_m(\omega)$ [3]. In this geometry propagating waves are described by the equation $\mathbf{E}(x,y,z) = \mathbf{E}(z)\,e^{i\beta x}$, with $\beta = k_x$ being a complex parameter called propagation constant, corresponding to the component of the wave-vector of in the direction of propagation.

Imposing correct boundary conditions on fields, the solution of the equation (3.2) (together with the one for $\mathbf{H}$) gives the dispersion relations of a SPPs propagating at the interface between the two half spaces:

$$\beta = k_0\sqrt{\frac{\varepsilon_m\varepsilon_d}{\varepsilon_m + \varepsilon_d}}, \tag{3.3}$$

This relation is valid for both complex and real ε_m, i.e., for metals with or without attenuation. In figure 3.1 is shown the dispersion relations of SPPs for a Drude metal with negligible damping at air and silica interface. The SPP excitations correspond to the part of the dispersion curve on the right side of the light line, thus direct SPPs is not possible due to the lack of an extra momentum and special techniques are needed for phase matching. The simplest techniques are the prism coupling and the grating coupling.

Localised surface plasmons

SPPs are propagating, dispersive EM waves coupled to the electron plasma of a conductor at a dielectric interface. Whereas Localized Surface Plasmons (LSP) are non propagating charge density oscillations confined to metallic nanoparticles or nanostructures. When light interacts with metallic particles much smaller than the incident wavelength, the electrons of

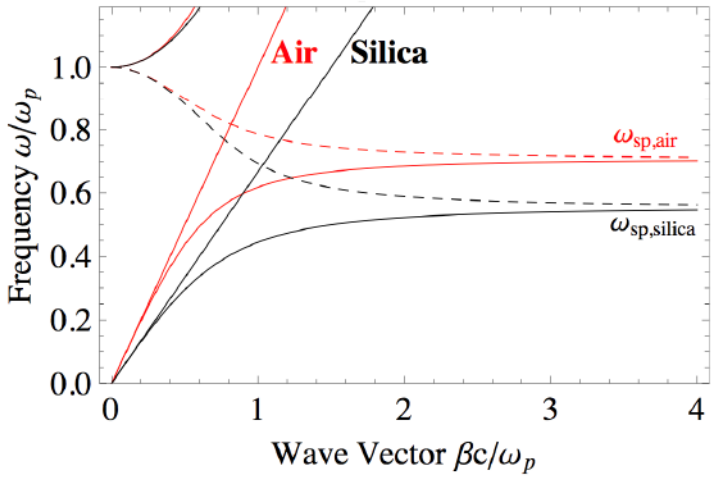

Figure 3.1: Dispersion relations at Drude metal/air (ε_d=1) and Drude metal/fused silica (ε_d=2.25) interface. The frequency (ω) is normalized to the plasma frequency (ω_p). Solid lines represent real wave-vector β, dashed lines represent imaginary wave-vector. The light lines ($\omega = kc$) are also shown [3].

a nanostructure can couple to the electromagnetic field. The curved surface of the particle exerts a restoring force on electrons, so that resonances may arise when the particle is placed in an oscillating EM field. These resonances promote a field enhancement both inside the particle and in the near-field zone around it. In contrast to SPPs, LSPs can be excited by direct light, without any special technique. The frequency of the resonance depends on the metal, the shape and the size of the particles and from the dielectric constant of the medium embedding the nanoparticles. For spherical particles the Mie theory allows a full treatment of the scattering problem by a single non-interacting spherical particle [?, ?]. However, when the shape of a particle has not particular symmetries or when dealing with ensembles of particle, the problem becomes very complex, a general analytic solution does not exist and computational methods become necessary.

3.2.1 Nanohole array

A Nanohole Array (NHA) is a (metal) thin film, whose thickness usually ranges from some tens to some hundreds of nanometres, having passing-through holes arranged in an (ordered) 2D array. Optically, NHAs have two interesting features, strictly relate one to the other. The first one is the ability to couple photons to surface plasmons without the need of a prism, thus acting as a grating. The second feature is the so-called Extraordinary Optical Transmission (EOT) [?, ?, 6]. In EOT, although the thickness is larger than the attenuation length for photons, and the holes diameter is smaller than the $\lambda/2$ Abbe's limit for transmission, light can pass through the NHA in a way which is forbidden by geometrical optics. The EOT was first observed by Ebbesen et al. in 1998 [6] and since then has attracted an increasing interest. The properties of Nanohole Arrays are related to their ability to efficiently convert light into surface plasmons by providing the necessary momentum for the conservation in the coupling. The extraordinary transmission process can be divided into 3 phases: the coupling of light to the SPP on the incident surface, the transmission through the hole and the re-emission from the second surface. Thus, the EOT reside on the coupling relations on both surfaces, and the

transmission maximum condition can be derived from the conservation of momentum:

$$\mathbf{k}_{sp\parallel} = \mathbf{k}_{\parallel} \pm m\mathbf{G}, \tag{3.4}$$

where $G_x = G_y = 2\pi/a_0$ are the lattice base vectors for square lattice and $k_x = 2\pi/\lambda$ is the momentum of the incident light. For lattices with hexagonal symmetry, the maximum condition for normal incident light is given by:

$$\lambda_{max} = \frac{a_0}{\sqrt{\frac{4}{3}(i^2 + ij + j^2)}} \mathbf{Re}\left[\sqrt{\frac{\varepsilon_m \varepsilon_d}{\varepsilon_m + \varepsilon_d}}\right], \tag{3.5}$$

where ε_m and ε_d are the dielectric function of the metal and of the dielectric in contact with it, and i and j are the scattering orders. Given the dispersion of the metal, its dielectric function is not constant, therefore the relation must be used exclusively to get the maximum wavelength. This relation does not take into account the shape of the holes, thus the losses at the edges of the holes are not considered and may modify the position of the maximum. Experimentally, it has been observed [?, ?] that, due to this effect, the resonances result slightly red-shifted with respect to those predicted by eq. (3.5). Moreover, the relation is valid for a single interface. When the NHA is in contact with a second surface with a different dielectric constant, the wavelength of the EOT peaks would be modified, and in the transmittance spectrum two set of peaks will arise, one for each interface. This is the usual case for a nanohole array on glass, with air at the other interface. The size and shape of the holes have also an important role in the extraordinary transmission of light, changing holes shape from circular to square also the transmission pattern of the NHA will be modified [?, ?]. The hole shape, indeed, will affect both the cut-off wavelength and the LSP modes associated with each hole. However, the SPP modes determined by the periodicity of the array dominate in the transmittance spectrum formation [?]. One interesting feature of hole arrays is the fact that each hole on the output surface acts like a new point source for the light. Therefore, if a plane wave impinges on the input surface, then a plane wave is reconstructed through classical interference as the light travels away from the output surface [?]. Due to these peculiar optical properties NHAs are finding many potential application ranging from subwavelength optics [?, ?, ?, ?] and optoelectronics [?, ?, ?] to chemical and biosensing [?, ?, ?, ?, ?]. The presence (and the ability of photon coupling) of plasmonic and holes modes is the key in the modification of Local Density of Optical States (LDOS).

3.3 Nanohole Array fabrication

With the rapid development in recent years of nano-fabrication techniques, many different methods can be used to fabricate NHAs depending on the size regime. The most common are Electron Beam Lithography (EBL) and Focus Ion Beam (FIB); both of them can produce apertures with arbitrary shape and size down to few of nanometers due to the high resolution. Nonetheless the main disadvantages of these techniques are that they are extremely expensive in terms of both time and cost and the patterned area is rather small (usually less then 1 mm^2). A possible alternative is represented by the NanoSphere Lithography (NSL) combined with Reactive Ion Etching (RIE). In the present work it was adopted this approach. The synthesis process for the fabrication of NHAs with these techniques can be divided in three main steps: (i) self-assembly of a single layer colloidal nanosphere of Polystyrene on the substrate surface,

(*ii*) reduction of the sphere size by RIE process and (*iii*) metal deposition via sputtering technique. In the following a brief description of the synthesis process will be given.

3.3.1 NanoSphere Lithography

NanoSphere Lithography (NSL) can be considered as an inexpensive, high-throughput self-assembly technique that produces triangularly shaped nanostructures with typical size that ranges from about 20nm to 1μm. One of the main advantages is that the patterned area can extend over several cm^2 or even more [**?**]. NSL was developed by Van Duyne and co-workers and provides a method to fabricate nanoparticle arrays with a tunable localized surface plasmon resonance (LSPR) [**?**, **?**, **?**]. It is based on the self-assembly of a monolayer of size-monodisperse spherical nanoparticles to form a colloidal crystal on the substrate surface, that in turn is used as a mask for the metal deposition. Many methods can be used for deposition of the nanoparticles on the substrate like spin coating, drop coating, dip coating and thermoelectrically cooled angle coating. The chosen method is based on the works of Schatz [**?**] and uses a colloidal suspension of polystyrene (PS) nanospheres in ultra-pure water and alcohol. The first step is the cleaning of the substrate in a "Pirahna" solution (a 3:1 mixture of concentrated sulphuric acid with 30% hydrogen peroxide). The substrate is then rinsed with Milli-Q water and dried in a stream of nitrogen. The suspension of PS nanoparticles and isopropylic alcohol is poured on the clean substrate and slowly immersed in a large glass vessel filled with Milli-Q water. PS particles self-assemble at the meniscus between alcohol dispersion and water bath, the resulting compact monolayer floats on the water surface, and it is collected on the substrate surface and slowly pulled out and dried at room temperature. As the liquid evaporates the capillary forces pull the PS nanosphere together forming a close-packed colloidal crystal with hexagonal symmetry that is used as a template for the successive steps of the fabrication process. In Fig. 3.2(a) is shown a sketch of the Schatz's NSL technique, while in Fig. 3.2(b) a SEM image of a self-assembled monolayer of PS nanoparticles with diameter d=900 nm; it is worth observing that the single domain colloidal crystal extends over tens of μm^2.

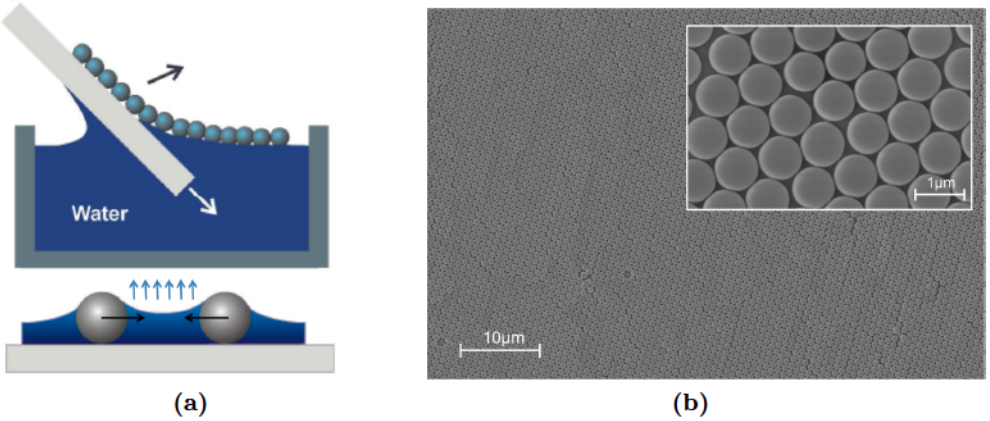

(a) **(b)**

Figure 3.2: (a) Schematic representation of the NLS process. (b) SEM image of a self-assembled monolayer obtained in the present work with PS nanoparticles with size d=920 nm.

3.3.2 Reactive Ion Etching

For the fabrication of the NHAs, the diameter of the PS nanoparticles of the colloidal crystal has to be reduced keeping unchanged the lattice position of the spheres to obtain on the sample surface a 2D periodic non-closed-packed array of PS nanoparticle, that will be used as a mask for the subsequent metal deposition. Therefore any chemical wet etching technique has to be avoid because it will alter the periodicity and the order of colloidal crystal. Reactive Ion Etching, instead, can reduce the nanosphere size without altering their order. RIE is a well established dry micro- and nano-fabrication technique that uses a chemically active plasma; it combines the mechanical erosion from the plasma with the chemical reactivity of the ionized species that react with the substrate forming volatile by-products. The etching is anisotropic and chemically selective, and the gas mixture determines the etched species. The most important parameters controlling the etching rate are the gas composition, plasma energy and working pressure. To reduce the PS nanoparticle size it has been chosen to work with a mixture of Ar (55%) and O_2 (45%) gas at a pressure of 4×10^{-2}mbar with an applied power of 25 W. Fig. 3.3(a) shows the nanosphere diameter (initial size d_0=(720±5) nm) as a function of etching time. The trend is monotonic but non linear since the etching direction is perpendicular to the sample surface and produces nanoparticles with a characteristic double-lens shape (see SEM cross section in Fig. 3.3(b)). A parabolic function (red dashed line in Fig. 3.3) fits well the experimental data. Thus, the NHA hole size can be easily tailored acting on the etching duration.

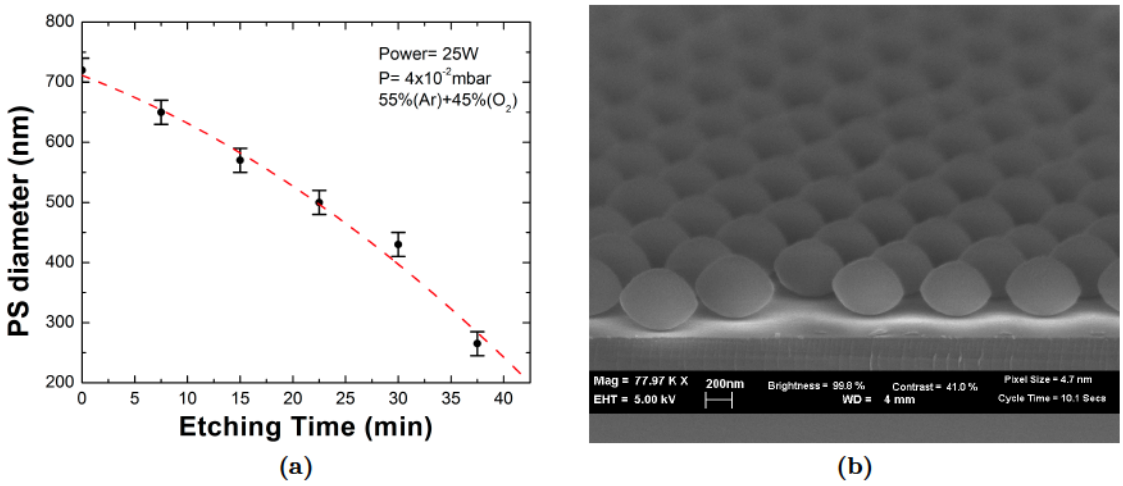

(a) (b)

Figure 3.3: (a) Etching rate for PS nanospheres with d=720 nm. The experimental date were fitted with a parabolic function (red dashed line). (b) SEM cross section image of an etched self-assembled monolayer of PS NPs with d_0=720 nm. RIE duration: 22 min.

3.3.3 Metal deposition

Once the 2D periodic array of PS nanoparticles has been obtained, it has been used as a template for a noble metal deposition. The metal will deposit both on the top of the nanoparticles and on the surface of the substrate, in the gap region between the etched spheres. The noble metal deposition was performed by means of a direct current (DC) source of a magnetron sputtering system. The sample holder was placed in front of the DC source, parallel to the

surface of the target in order to have a collimated sputtered atom flux that can replicate the pattern of the etched mask. The power of the source has to be kept as low as possible to avoid the heating of the sample and thus the melting of the PS nanoparticles. After the film deposition, the PS nanospheres can removed by ultrasound sonication in toluene, leaving a metallic nanohole array on the samples surface. As an example, Fig. 3.4(a) shows a SEM image of a gold NHA obtained from PS nanoparticle with a diameter d=920 nm, the RIE process has been carried out in Ar+O_2 atmosphere for 40min and the deposited metal thickness is t=120 nm. It is worth noting that the defect-free 2D periodic hole array with hexagonal symmetry extends over several μm^2. Fig. 3.4(b) reports the transmittance spectra at normal incidence of three gold NHAs with different lattice parameters (a_0=722, 920, 1340 nm); the broad peak in the NIR region associated with the (1,0) Bragg resonance EOT is function of the lattice parameter, and its wavelength maximum can be tailored simply by choosing the proper diameter of PS nanoparticles (d=a_0).

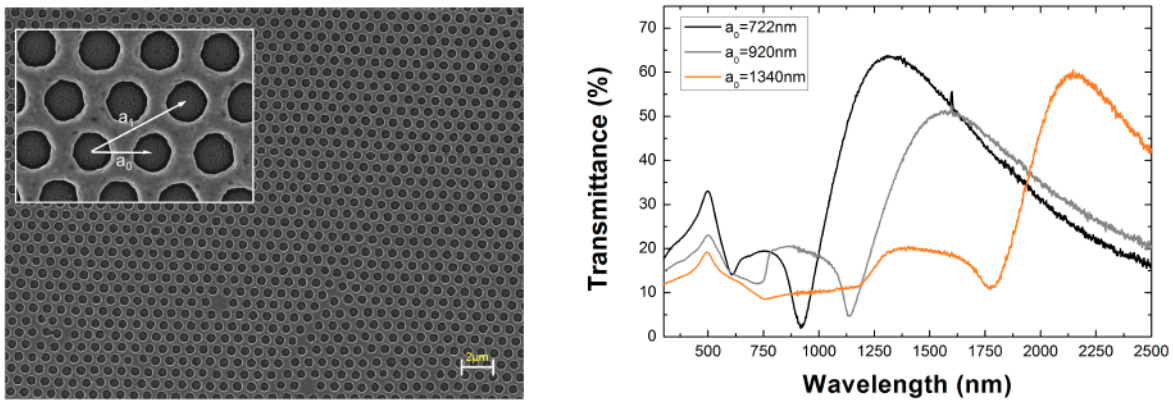

(a) (b)

Figure 3.4: (a) SEM image of a gold NHA with a_0=920 nm. (b) Optical transmittance spectra at normal incidence of Au NHAs on silica substrate with different lattice parameters (i.e., a_0=722, 920 and 1340 nm).

3.4 Finite Element Method simulations

Since a theoretical model that predicts the variation of the emission properties of an emitter close to a NHA has still to be developed, finite elements method (FEM) simulations were used to both predict the lifetime variation and gain more information about the near-field of the emitter, otherwise not accessible with experimental methods. FEM simulations were performed with the commercial software COMSOL Multiphysics 4.3b [**?**] in the frequency domain (Finite Difference Frequency Domain (FDFD)). Simulations have been carried out considering one dipole at a time. The signal from an arbitrary distribution of dipoles and their variations of decay rates were then recovered by integrating the results from differently placed dipoles. For this purpose the common approach used for the simulation of periodically ordered structures, consisting in the modelling of a unit cell with periodic boundary conditions was not suitable Er:SiO_2-NHA geometry. This approach, indeed, would generate a mirror dipole in each cell, thus the simulation would describe a system where dipoles have the same periodicity of the nanostructure, which is not the case. The alternative is to extend the simulation domain

to include several unitary cells together, using Perfectly Matched Layer (PML - an additional (artificial) domain that absorbs the incident radiation without producing reflections) at the boundaries to suppress backscattering. For the correct implementation of the model, the minimum size of the domain has to be the one that ensures that near-field from the dipole emission vanishes before reaching the boundaries.

As a first step, the effect of a semi-infinite film have been modeled to determine the domain minimum size and to validate the method using as a benchmark the electrodynamical derivation proposed by Chance et al. [62], and discussed in the section 2.4. A simulation domain surrounded by a sphere of radius (R$\sim 3\lambda_{em}$) was found to be enough for the correct modelling of the emitter lifetime variation in close proximity of an interface, as it will be shown in the following. To simulate an Er-like emitter (λ_{em}=1540 nm) interacting with the film, the domain have been divided into two hemispheres, one representing the silica matrix, the other representing the film. The interface has been placed at the z=0 plane. Dipoles have been placed so that their projection on the interface plane falls in the center of the simulated sphere (x=0, y=0). The z coordinate of the dipoles (i.e., the distance from the interface) have been varied from 1 nm to 1000 nm.

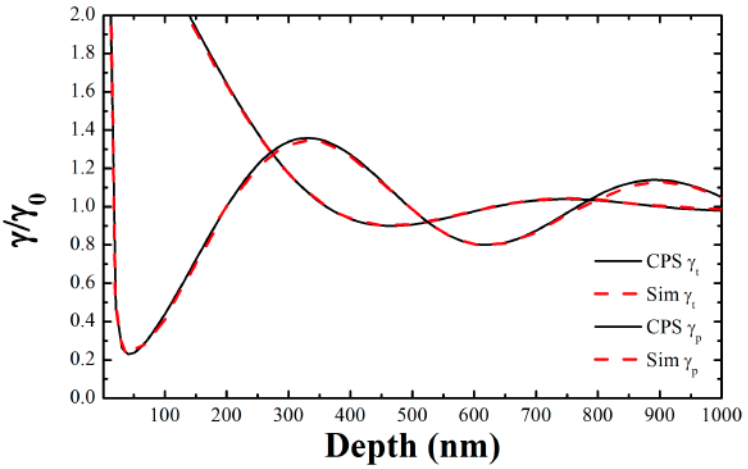

Figure 3.5: Comparison between simulation (Sim) and CPS model for the variation of the normalized decay rate of an Er-like emitter (λ_{em}=1540 nm) as a function of the distance from a gold film.

For each z position, the decay rate for a dipole with parallel (γ_p) and perpendicular (γ_t) orientation with respect to the interface was calculated. The normalized decay rate was evaluated integrating the Poynting vector (**S**) on a closed surface (Σ) encircling the dipole and dividing by the decay rate (γ_0^r) calculated without the interface (ε_1=ε_{SiO_2}= 2.085) :

$$\frac{\gamma^r}{\gamma_0^r} = \frac{\int_\Sigma \mathbf{S}\, d\sigma}{\int_\Sigma \mathbf{S_0}\, d\sigma} \tag{3.6}$$

In Fig. 3.5 the resulting values of γ_t and γ_p are plotted as a function of the distance from a gold film (ε_2=-116.91 + 9.73i). The simulated variation of the decay rate (red line) for both orientations is in perfect agreement with the result obtained by the CPS model (black line), thus validating the simulation parameters chosen for the modelling of emitter-film interaction. To take into account the Er distribution in the z direction typical for the Er:SiO_2 co-sputtered films, the procedure described in section 2.4 has been used, leading as expected to the same calculated lifetime values.

The simulations of the emitter-NHA interaction have been carried out in an analogous way. In this case, the whole simulated domain is constituted by silica (c.f. section 3.5.1), except for the NHA film extending in the XY plane, and centred at z=0, as shown by Fig. 3.6. Unlike the film geometry, the translational invariance in the XY plane doesn't hold any more and it has to be replaced with the periodic Honeycomb lattice resulting from the NSL process. As already discuss, the periodic boundary conditions can not be used for the correct evaluation of the decay variation due to the replication of the emitter. Thus, 19 XY unit cells have been modelled, in order to obtain the domain size determined for the film geometry. Because the periodicity of the lattice, the behaviour of the emitter can be sampled in one unitary cell only. Moreover, due to the symmetries in $\hat{x}$ and $\hat{y}$ direction, the hexagonal unit cell can be reduced to only a quarter, as shown by Fig.3.7(a).

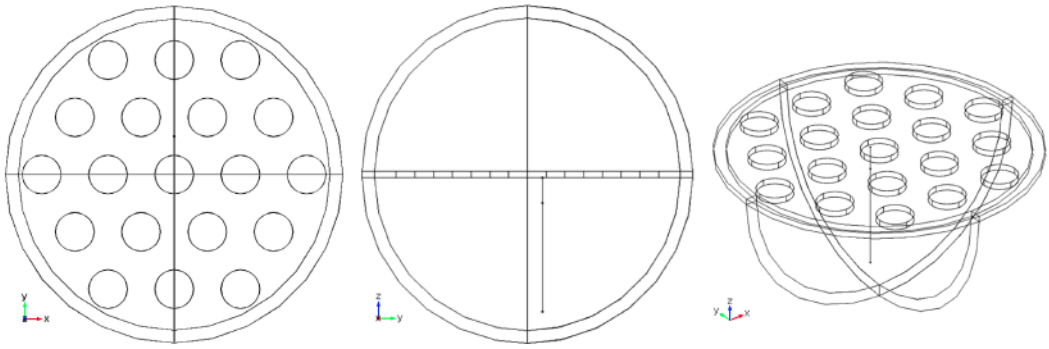

(a) **(b)** **(c)**

Figure 3.6: Wireframe views of the NHA-emitter interaction model: XY top view (a), YZ cross model (b), XYZ 3D view (c)

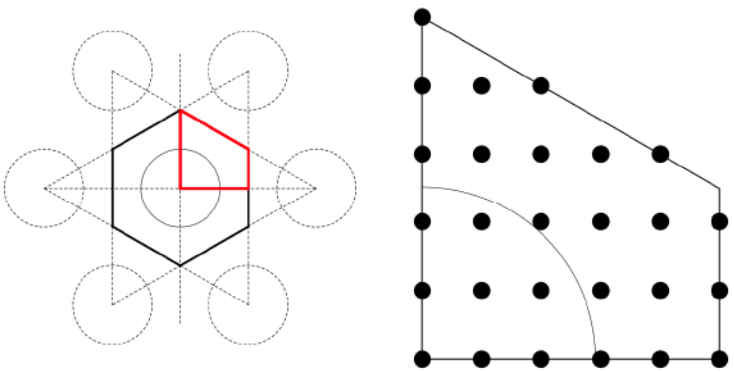

Figure 3.7: (a) Construction of the Wigner-Seitz (WS) cell. Dashed lines represent the symmetry planes; black line is the WS cell; red line encircles the sampled cell exploiting lattice symmetries and $\hat{x}$ and $\hat{y}$ symmetries. (b) Sampling grid in the minimal cell: 27 points. Points on the edges and vertices have a coefficient c_{ij}<1 in averages.

Once the minimum cell has been defined, for each z value a grid with 27 points representing the dipole position in the XY plane have been defined according to Fig. 3.7(b), to sample as accurately as possible the whole cell. Moreover, for each position in the XY plane 3

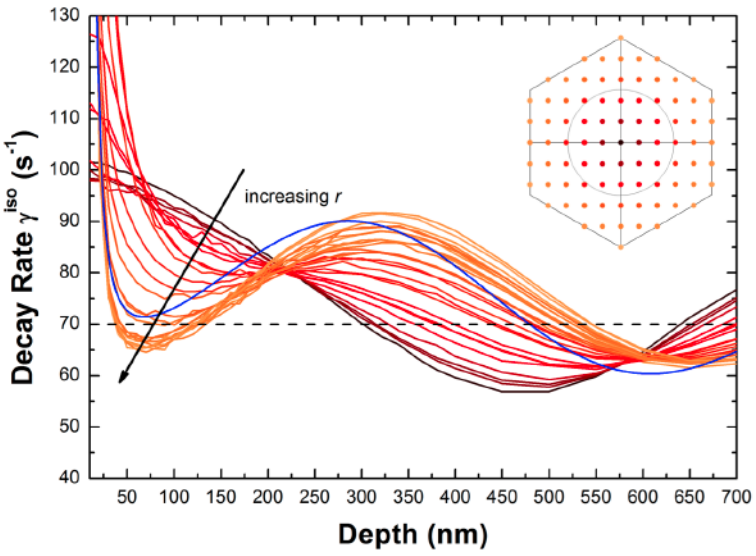

Figure 3.8: Simulated γ(z) as a function of the distance from a Au NHA for an Er-like emitter (γ_0=70s^{-1} (dashed line), λ_{em}=1540 nm) placed at different positions in the XY plane. The color gradient represents the projected distance ($r = \sqrt{x^2+y^2}$) form the centre of the hole. NHA lattice parameter is a_0=1030 nm, hole diameter d=600 nm and metal thickness t=120 nm.

different dipole orientation have to be taken into account, since in addition to the perpendicular orientation, the parallel one has to considered along $\hat{x}$ and $\hat{y}$ the axes of the NHA. Thus, when the emitters have an isotropic orientation configuration the decay rate becomes $\gamma_{iso} = 1/3(\gamma_t + \gamma_{px} + \gamma_{py})$. As an example, Fig. 3.8 shows the decay rate (γ_{iso}) for the 27 positions of an Er-like emitter as a function of the distance from a NHA with lattice parameter a_0=1030 nm; the black line represents the dipole at the center of the hole. The colors are as lighter as the projected distance ($r = \sqrt{x^2+y^2}$) from the center of the hole increases and the variation of the decay rate becomes more prominent for small distances from the NHA. As a comparison, the blue represents the result obtained in the plane Au film case. Furthermore, it is worth noting that in the range $0<z<\lambda_{em}/2$ there are two regions at z ~200 nm and z ~600 nm where the modification of the lifetime is almost insensitive to the position of the emitter in the XY plane.

To average dipole emission in this case, the equation 2.13 must be rewritten considering the differences given by the XY position of the emitter. The integral is still present in the $\hat{z}$ direction, while in the XY plane, the integration is substituted by a sum over the 27 emitter positions sampled in the minimum cell and denoted by the couple of i and j indices:

$$I_{PL}(t) = I_0 A \sum_{i,j} c_{ij} \int_0^{+\infty} f(x_i, y_j, z) e^{-\gamma^{iso}(x_i, y_i, z)t} dz, \tag{3.7}$$

where the coefficients c_{ij} account for the normalization of the points shared by adjacent cells and $A = 1/\sum_{ij} c_{ij}$ is a global normalization factor.

3.5 Er-NHA interaction

The presence of a nanostructure in close proximity to Er ions can in principle both enhance or quench the characteristic emission at 1540 nm. It has been demonstrated that when a

plasmonic nanoparticles is close to an emitter two competitive mechanisms take place: the near-field enhancement and the reduction of the quantum efficiency due to energy transfer to the nanostructure. Conversely, due to the lack of a developed theoretical description of the phenomenon, the influence of a NHA the emissive properties of optically active species has still to be deeply investigated. To this purpose in the present section the variation of Er^{3+} lifetime at 1540 nm will be investigated both experimentally and with computer simulation as a function of the distance and the NHA optical properties.

3.5.1 Sample synthesis

The Er:SiO_2 thin films were deposited on 2.5×2.5 cm^2 silica substrate (HSQ300 by Heraeus) by means of a magnetron co-sputtering system. In addition to the high control over both the film thickness and the dopant concentration, sputtering deposition technique offers the possibility to deposit undoped silica on top of the Er:SiO_2 film in a single process, thus the distance between the Er doped layer and the sample surface can be finely tailored. Before the deposition, silica substrates were cleaned in a "piranha" solution (30%H_2O_2, 70% H_2SO_4) for 20 min and copiously rinsed with Milli-Q water (18 MΩ resistivity). The RF-power to the 2 in. diameter silica target was fixed at 250 W while the DC power to the Erbium 2 in. diameter target was 3 W for obtaining an Er concentration of 1.0% at. (determined by RBS measurement). During the depositions, the sample holder was rotated to have a good homogeneity of the film composition and thickness. For all the samples the Er:SiO_2 film thickness was 20 nm, while silica spacers with three different thicknesses (t_{SiO_2}) were deposited on top, correspondingly the samples were labelled as A10 (t_{SiO_2}=10 nm), A30 (t_{SiO_2}=30nm) and A100 (t_{SiO_2}=100 nm). The samples were then cut in three pieces, one was left as a reference, on the other two Au NHAs with two different lattice parameter were fabricated (a_0=1030 and 1280 nm). The reference samples were annealed at 900°C for 2 hours in vacuum and the Er^{3+} lifetime (τ) was determined via PL measurements under resonant excitation at λ=488 nm at room temperature. The measured τ values were 11.8, 11.7 and 10.6 ms for the samples A10, A30 and A100, respectively. As already discussed, the lifetime variation has to be attributed to the different distances of the Er:SiO_2 film from the air interface (i.e., surface of the sample). With the procedure described in section 2.4.1 the non-radiative decay rate (Γ_0^{nr}) was determined to be (32±3) s^{-1}.

The NHAs were fabricated on the surface of the not-annealed samples with increasing silica spacer with a combination of NSL and RIE techniques, as described in section 3.3. PS nanoparticles with diameters of 1030 nm and 1280 nm were used for the NSL. RIE treatment was performed to reduce the diameter of the PS nanospheres, retaining their original ordered lattice arrangement. The etching time have been set 43 min and 48 min for the 1030 nm and 1280 nm sphere, respectively. The radius of the etched nanospheres (and thus the radius of the obtained nanoholes) was reduced by a factor about 2/3 from the original size. After the etching, a gold film layer 120 nm thick has been deposed by DC sputtering on the NSL-patterned surface. Finally, the PS nanospheres were removed by ultrasound sonication in toluene, leaving a gold nanohole array on the samples surface. The samples will be labeled following the notation used for the reference samples with the addition of the NHA lattice parameter (i.e., sample A30-1030, has a silica spacer (distance between Er:SiO_2 and NHA) of 30 nm and Au NHA with a_0=1030 nm). To prevent shape modification during the 900 °C annealing necessary for the Er^{3+} PL activation, a 400 nm thick silica film was deposited on top on of the NHAs. In Fig. 3.9(b) are shown the transmittance spectra at normal

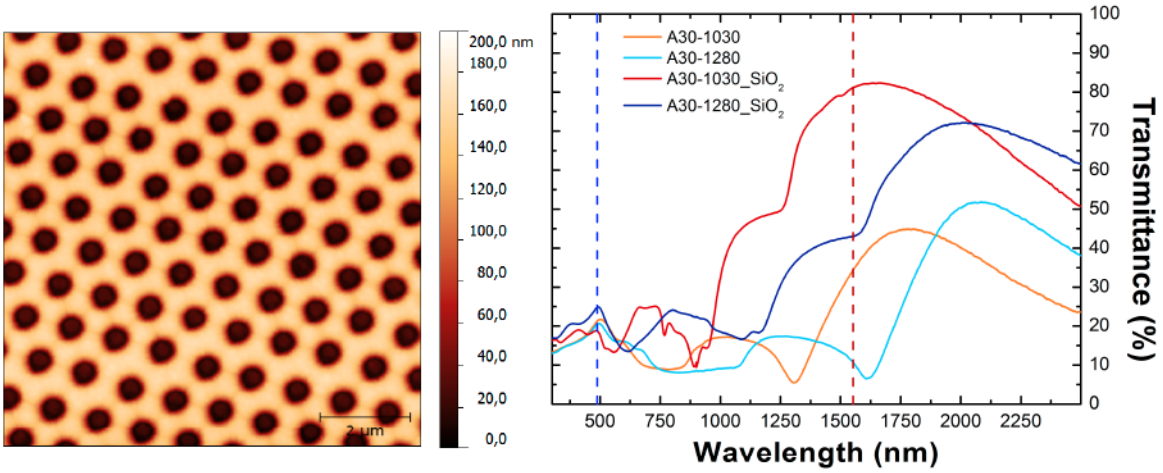

Figure 3.9: (a) AFM topography of the sample A100-1030 after the silica deposition and the Er^{3+} activation annealing. The image has been acquired in a semi-contact mode by means of a NT-MDT Solver-Pro AFM. (b) Optical transmittance spectra at normal incidence for the sample A30-1030 and A30-1280 before and after the silica deposition and the annealing. The vertical dashed lines indicate the Er^{3+} excitation and emission wavelengths, in blue and red respectively.

incidence for the A30-1030 and A30-1280 samples before and after the silica deposition and the 2 h 900 °C annealing in vacuum. The silica-capped samples show a blue-shift of the EOT peak with a significant increase of the maximum transmittance. The set of samples with a_0=1030 nm exhibit a (1,0) Bragg resonance EOT peak maximum that matches the Er^{3+} characteristic emission wavelength (λ=1540 nm), while for the a_0=1280 nm samples the EOT peak is shifted to larger wavelengths. It worth noting that despite the multi-step synthesis process, no difference in the transmittance spectra were detected between samples with the same lattice parameter, showing the good reproducibility of the nano-fabrication process. Fig. 3.9(a) shows an AFM topography of the A100-1030 sample after the silica deposition and the Er^{3+} activation annealing, it is interesting noting that despite the thick silica film (t=400 nm) the surface of the sample is still patterned with the NHA geometry.

3.5.2 PL measurements

To characterize the Er^{3+} luminescent emission properties of the samples and investigate the interaction mechanisms between the Er ions and Au NHAs, photoluminescence (PL) measurements were performed (both integrated and time-resolved) at room temperature using resonant (λ=488 nm) and out-of-resonance (λ=476.5 nm) Er excitation conditions. A CW Ar laser was used as excitation source. The laser lines were selected by interference filters. The experimental set-up is described in section 1.3.1.

Under resonant excitation no difference in the PL peak position or shape were detected. Fig. 3.10 reports the PL decay curves at λ=1540 nm of the two sets of samples with different NHA size and the reference sample A30. All the samples are characterized by single exponential decay that has been fitted with the function $I_{PL} = I_0 \mathbf{exp}(-t/\tau)$ to determine the Er lifetime. With both NHA lattice size a significant reduction of the Er lifetime at 1540 nm has been observed. Their reduction is a function of the distance between the Er:SiO_2 film and the NHA

and the effect is higher as the distance decreases. The transmittance spectra were measured at normal incidence with respect to the NHA plane, while the rare earth emission in a glassy matrix is in general angularly isotropic, therefore it is difficult to estimate *a priori* the matching of the EOT peak with Er^{3+} emission wavelength. Nonetheless, it is interesting noting that as the distance decreases, the samples with (1,0) Bragg resonance EOT matching the Er emission at normal incidence exhibit a stronger shortening of the lifetime as compared to the NHA with a_0=1280 nm (λ_{EOT}=2020 nm), and particularly the sample A10-1030, which shows the shortest lifetime with a reduction by a factor 2.5 with respect to the reference sample. No PL intensity has been detected under non-resonant excitation (λ=476.5 nm), indicating that in the absorption of exciting radiation no energy transfer mechanism occurred between the nanostructured gold film and Er ions.

An interesting feature for possible photonic applications (e.g. optical planar amplifiers or filters) arising from the peculiar NHA optical properties is that the PL signal can be detected from both sides of the sample. Collecting the signal through the NHA, it can act as a filter selecting only the wavelengths matching the EOT peaks. Therefore, since both samples exhibit a significant transmittance at λ=1540 nm, the PL time resolved spectra were measured also collecting the light through the NHA. No difference in the lifetime has been detected with respect to detection from the front, indicating that Er^{3+} PL dynamics is the same whether the emitted radiation couples directly in the far-field radiation or it is first coupled with the NHA surface plasmons and then coupled out into far-field radiation.

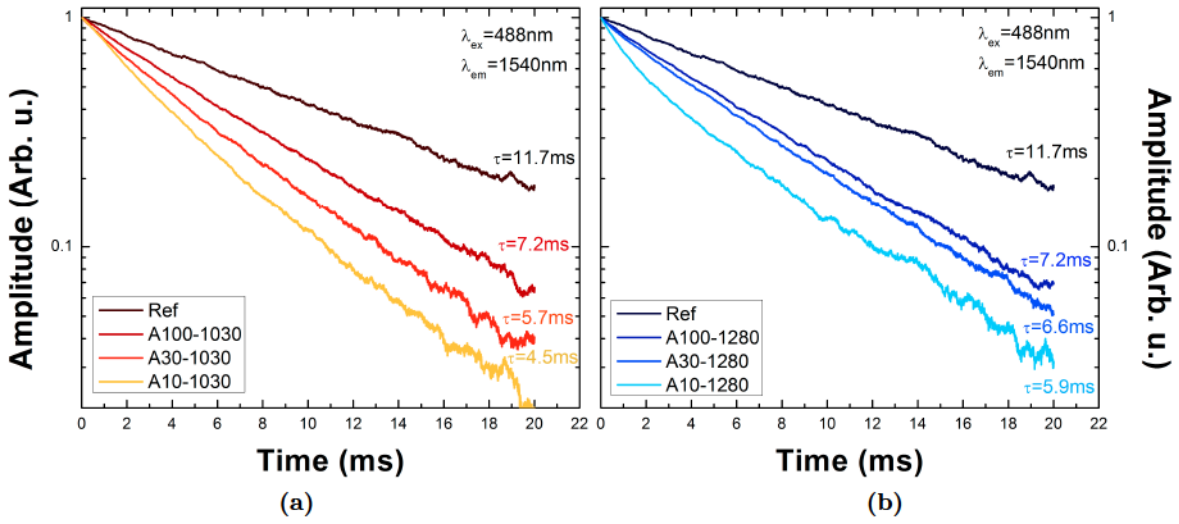

Figure 3.10: Room temperature PL decay measurements at 1540 nm performed under resonant excitation conditions of the two sets of samples: NHA with a_0=1030 nm (a) and a_0=1280 nm (b). In (a) and (b) the black curve is the reference sample A30.

3.5.3 Effective medium approximation

The first attempt to find a model that predicts the modification of the radiative properties of an emitter in close proximity to a NHA, has been carried out following the CPS model used for the film geometry and describing the NHA as an effective medium (EMA). Since the dielectric function of the NHA can not be experimentally determined with ellipsometric

measurements due to the complexity of the patterned surface, a possible solution could be represented by the effective medium approximation. The dielectric function of sputtered and annealed gold (ε_{Au}=-116.913+i 9.73525) and silica (ε_{SiO_2}=2.085) were independently characterized and three different formulation for the EMA were evaluated. The simplest model is the so called Newton formula that consists in a linear combination of the two dielectric functions weighed with the volumetric fraction of the two materials (f_{SiO_2} and f_{Au}=1-f_{SiO_2}), the effective dielectric function (ε_{CL}^{eff}) is given by:

$$\varepsilon_{CL}^{eff} = f_{SiO_2}\varepsilon_{SiO_2} + f_{Au}\varepsilon_{Au}. \tag{3.8}$$

A more accurate description can be given by the Maxwell-Garnett formulation of the effective medium approximation, where ε_{M-G}^{eff} is given by:

$$\frac{\varepsilon_{M-G}^{eff} - \varepsilon_{Au}}{\varepsilon_{M-G}^{eff} + 2\varepsilon_{Au}} = f_{SiO_2}\frac{\varepsilon_{SiO_2} - \varepsilon_{Au}}{\varepsilon_{SiO_2} + \varepsilon_{Au}}. \tag{3.9}$$

An alternative model to calculate the effective dielectric function (ε_{B}^{eff}) for topology with dense mixing of the two materials is the Bruggemann formula:

$$f_{Au}\frac{\varepsilon_{Au} - \varepsilon_{B}^{eff}}{\varepsilon_{Au} + 2\varepsilon_{B}^{eff}} = -f_{SiO_2}\frac{\varepsilon_{SiO_2} - \varepsilon_{B}^{eff}}{\varepsilon_{SiO_2} + 2\varepsilon_{B}^{eff}}. \tag{3.10}$$

The metal and silica volumetric fractions are function of the hole size and for both NHAs under study were determined to be f_{SiO_2}=0.31 and f_{Au}=0.69. Independently of the considered model, one may immediately observe that the optical transmittance of the NHAs can not be predicted since the periodicity of the lattice that determines the EOT wavelength can not be taken into account. At Er^{3+} emission wavelength the effective dielectric functions calculated with Newton, Maxwell-Garnett and Bruggeman formula are -80+i 6.72, -31.65+i2.83 and -60.62+i5.21, respectively. Again, the difference in the Er^{3+} lifetimes obtained with the two NHAs can not be correctly predicted with the EMA; indeed, applying the CPS model to the two set of samples, the lifetime shortening is always overestimated by a factor 2-3 depending on the effective dielectric function. In conclusion, neither the far-field nor the near-field optical properties of the NHAs can be evaluated with the effective medium approximation, hence FEM simulation have been implemented.

3.5.4 Comparison between experimental results and FEM simulations

To better understand the interaction between Er:SiO_2 thin films and NHAs, FEM simulation were carried out and compared with the experimental data. As a first step, the far-field properties of a modeled gold NHAs on silica (without any emitter in close proximity) were compared with optical transmittance spectra obtained with a set of 5 different experimentally fabricated NHAs with different lattice parameters (a_0). The hole radius and the metal thickness were determined via SEM and AFM measurements to ensure the correspondence of the NHA geometrical parameters with the simulated model. Table 3.1 reports the wavelength of the (1,0) Bragg resonance EOT peak and the relative transmittance at 1540nm (T_R=T_{1540nm}/T_{max}). In general good agreement between experimental data and FEM simulation can be found, although it is worth to underline that the simulated transmittance spectra have a narrower

Table 3.1: Gold NHA far-field optical properties: geometric parameters and measured and simulated EOT wavelengths. The simulated wavelength range is 300–1800 nm.

Lattice parameter (a_0) [nm]	Holes radius R [nm]	λ_{max}^{exp} [nm]	λ_{max}^{sim} [nm]	T_R
722	240	1170	1240	0.22
920	260	1385	1400	0.63
1030	300	1570	1520	0.97
1280	375	2020	>1800	0.55
1340	400	2142	>1800	0.12

EOT peaks since the experimental samples have a distribution of domain orientations over the investigate area ($\sim$1 cm^2).

To compare the variation of the Er^{3+} lifetime obtained by FEM simulations with the two set of samples described above, the approach already discuss for the film geometry has been implemented. The two NHA geometry (a_0=1030 nm and a_0=1280 nm) were modelled on the experimentally measured gold thickness (t=120 $\pm$ 3nm) and hole size ($\sim 0.6 \times a_0$). To find out the total decay rate Γ^{tot}, and has to add to the calculated radiative decay rate (Γ^r_{FEM}), obtained by fitting the first 20 ms of the equation 3.7 with a single exponential function, the non-radiative decay (Γ_0^{nr}) due to not fully recovered Er ions coordination in the silica matrix in the following way:

$$\Gamma^{tot} = \Gamma^r_{FEM} + \Gamma_0^{nr} \tag{3.11}$$

Since the presence of the NHA array do not alter the local Er environment or induces additional defects in the matrix, it is reasonable to assume that Γ_0^{nr} do not change from the one obtained from the reference samples and therefore for all the evaluated samples it was assumed to be 32s^{-1}. The calculated lifetime therefore can be expressed in the following way:

$$\tau_{calc} = \frac{1}{\Gamma^r_{FEM} + \Gamma_0^{nr}} \tag{3.12}$$

In Table 3.2 the calculated lifetimes are compared with the experimentally measured ones, and an almost perfect agreement can be observed, proving how the implemented model accurately predict the lifetime modifications of emitters due to the coupling with nanostructured noble metal film.

Table 3.2: Er^{3+} lifetime at 1540 nm. Comparison between the experimentally measured and the simulated lifetime values for the two Au NHAs. Lifetime of the reference sample is also reported.

Sample	Reference	NHA a_0=1030 nm		NHA a_0=1280 nm	
	τ_{exp} [ms]	τ_{sim} [ms]	τ_{exp} [ms]	τ_{sim} [ms]	τ_{exp} [ms]
A10	11.8	5.5	4.5	6.1	5.9
A30	11.7	5.8	5.7	6.4	6.6
A100	10.6	7.0	7.2	7.1	7.2

It is now possible gain more information on how the energy radiates away from Er ions interacting with noble metal NHA. For this purpose the radiative efficiency of a Er-like emitter placed at z=50 nm was calculated via FEM simulation. Neglecting the non-radiative decay

rate in the bulk silica, the far-field radiative efficiency (q_F) is defined as the ratio between the power radiated in the far-field (P_{ff}) and the total power (P_{tot}) emitted from a dipole:

$$q_F = \frac{P_{ff}}{P_{tot}} = \frac{\gamma_r}{\gamma_r + \gamma_{nr}} \tag{3.13}$$

where P_{ff} is the integral of the Poynting vector over the sphere encircling the simulated domain and γ_{nr} in this case takes into account the losses in the metal. Table 3.3 lists the computed radiative rates for air interface, optically thick (t=200 nm) gold film and compared with those obtained for a dipole placed at the centre of the hole of NHAs with a_0=1030 nm and a_0=1280 nm. The three different dipole orientation with respect to the interface have to be considered and the radiative far-field efficiency for an isotropic dipole distribution (q_F^{iso}) can calculated by:

$$q_F^{iso} = \frac{\gamma_r^x + \gamma_r^y + \gamma_r^z}{\gamma_{tot}^x + \gamma_{tot}^y + \gamma_{tot}^z} \tag{3.14}$$

Table 3.3: Computed far-field radiative efficiencies (q_F) of an Er-like emitter close to an overlayer. Comparison between air, gold film and Au Nanohole Arrays with a_0=1030 nm and a_0=1280 nm are presented. The dipole is placed 50 nm below the overlayer and in the NHA case at the centre of the hole. Three different orientation together the isotropic orientation distribution were evaluated.

Dipole orientation	**Air**			**Au film (t=200 nm)**		
	Forward	**Backward**	**Total**	**Forward**	**Backward**	**Total**
X	0.167	0.833	1	0	0.52	0.52
Y	0.167	0.833	1	0	0.52	0.52
Z	0.126	0.874	1	0	0.34	0.34
ISO	0.159	0.841	1	0	0.368	0.368

Dipole orientation	**NHA a_0=1030 nm**			**NHA a_0=1280nm**		
	Forward	**Backward**	**Total**	**Forward**	**Backward**	**Total**
X	0.42	0.56	0.98	0.43	0.55	0.98
Y	0.42	0.56	0.98	0.43	0.55	0.98
Z	0.25	0.75	1	0.23	0.76	0.99
ISO	0.363	0.623	0.987	0.36	0.623	0.983

It's worth highlighting that the far-field radiative efficiency for both NHAs is close to 100%, indicating that the Er^{3+} emission can be efficiently enhanced without almost any loss in the overlayer (<2%). The comparison with the film geometry shows that the far-field emission is increased by a factor about 2.5; this can be attributed to two main effects: the NHA configuration reduces significantly the coupling with lossy modes and the SPP modes propagating on the metal-dielectric interface can be re-emitted as photons in the far-field due to the 2D NHA periodicity, which in the film configuration is not possible due to the lack in the momentum. Furthermore, the NHAs permit an efficient forward emission that is increased by 2 to 3 fold with respect to the air interface, where the higher dielectric constant drives the emission in the silica half-space. The efficiency does not vary appreciably between NHAs characterised by EOT resonant and non-resonant with Er^{3+} emission wavelength. On one hand, this suggests that even in resonance the strong coupling does not mean large losses due to the plasmon decay

in the metal; on the other hand, this opens the possibility to combine in-resonance and out-of-resonance NHAs to get smart excitation-emission configurations without losing efficiency. q_F has been also calculated for dipoles placed in different positions of the Wigner-Seitz cell, and variation of the efficiency was found to be negligible since the computed values for all the positions are well above the 90%, indicating that the position of the emitter in the XY plane does not influence the efficiency of the system, thus in the design of a device the effort to place the emitting species just under the hole of the NHA to avoid losses is useless.

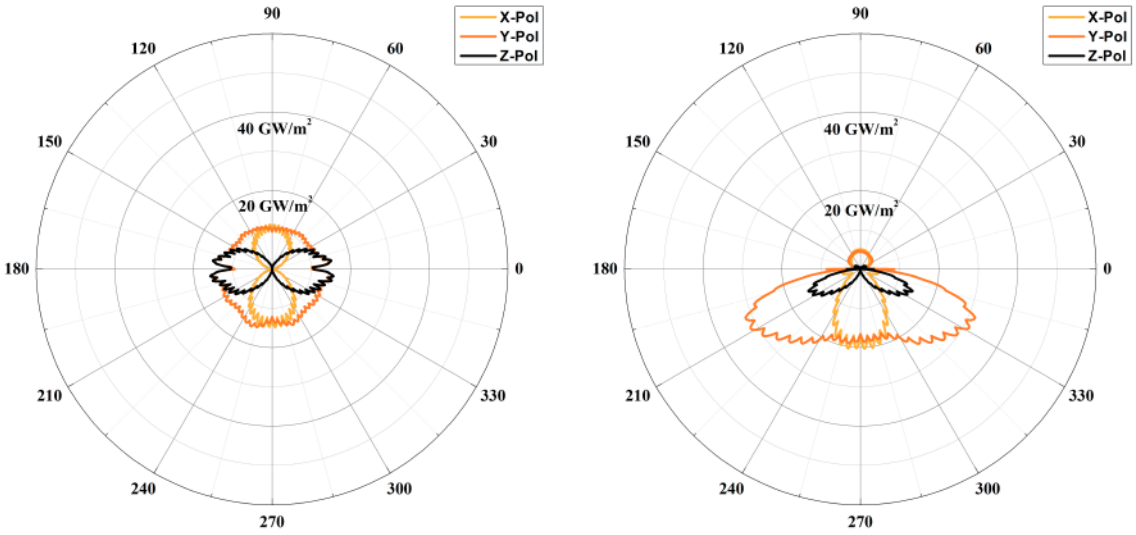

(a) SiO_2 **(b)** Air

Figure 3.11: Power outflow as a function of the angle evaluated at the outer edges of the simulated domain for an Er-like emitter embedded in silica (a) and placed 50 nm below an air interface (b). The polarization indicates the direction along which the dipole oscillates.

An interesting information derivable from FEM simulations is the angle-resolved far-field radiation pattern of an emitter placed under different overlayers. Fig. 3.11 shows how the radiation pattern is influenced by the proximity of the surface of the sample (i.e., 50 nm below the air interface). Due to the higher refractive index, the emission is deformed for all dipole orientations towards the silica half-space and just a small fraction exits in the upper semi-space. In Fig. 3.12 the emitter is placed 50 nm below chromium and gold overlayers, comparing the radiation patterns it can be observed that parallel orientations with respect to the interface (X and Y) are almost insensitive to the nature of the metal, while the perpendicular one is remarkably enhanced by the presence of a noble metal due to the coupling with SPP modes. Any emission in the upper half-space is suppressed because of the complete absorption of the photons by the metal film.

The great advantage of the emitter-NHA coupling can be understood from Fig. 3.13, where the emission pattern of the Er-like dipole at the centre of the hole, 50 nm below the gold nanostructure is shown for the two lattice parameters experimentally explored. The power outflow is strongly enhanced for all the polarizations and the emitted light can be collected from both sides. Interestingly, for the NHA with a_0=1030 nm where the EOT peak is resonant with the Er emission wavelength, the power outflow of the emitters oriented perpendicularly to

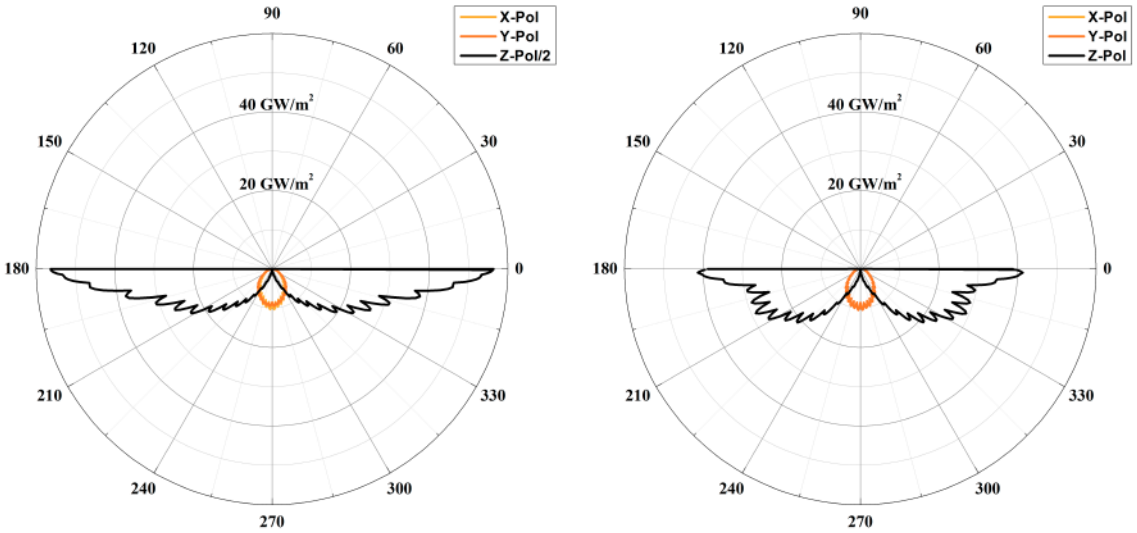

(a) Au film (t=200nm) **(b)** Cr film (t=200nm)

Figure 3.12: Power outflow as a function of the angle evaluated at the outer edges of the simulated domain for an Er-like emitter placed 50 nm below a 200 nm thick gold (a) and chromium (b) film. The polarization indicates the direction along which the dipole oscillates.

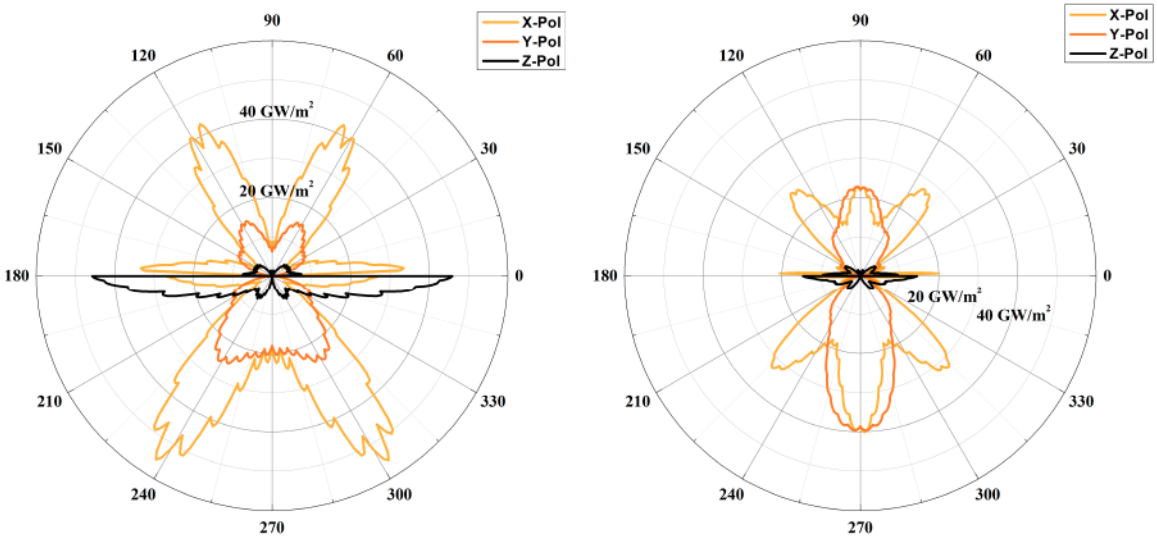

(a) Au NHA (a_0=1030nm) **(b)** Au NHA (a_0=1280nm)

Figure 3.13: Power outflow as a function of the angle evaluated at the outer edges of the simulated domain for an Er-like emitter placed in the centre of the hole, 50 nm below a Au NHA with a_0=1030 nm (a) and a_0=1280 nm (b). The polarization indicates the direction along which the dipole oscillates. For the Au film the power outflow of z orientation has been halved to fit the scale.

the interface is much higher than in the NHA with a_0=1280 nm, due to the stronger coupling with SPP modes.

3.6 Conclusions

It has been demonstrated that a combination of NSL and RIE can be used as a versatile and high throughput nanofabrication technique to produce highly ordered NHAs on an area much larger than the one obtainable with EBL or FIB. The optical properties can be easily tuned acting on the self-assembling PS nanoparticle size, RIE duration and metal thickness. Thus, it was possible to tailor the EOT peak and make it resonant with Er^{3+} emission wavelength. From the evaluation on how the proximity of a resonant and non-resonant NHA influence the lifetime of the characteristic emission at 1540 nm, it has been found out both experimentally and with FEM simulations that as the distance decreases the shortening of the lifetime is enhanced. Moreover, the resonant coupling of the emitters with noble metal NHAs yields a stronger enhancement of the emission especially for short distances. Simulated radiation patterns demonstrate that efficient coupling between Er emission at 1540 nm and SPP modes on NHA-dielectric interface can be obtained especially when the EOT peak is resonant with the emitted radiation. Contrary to the film case, the computed quantum efficiency shows that the enhanced emission from Er ions is not modulated by a large absorption in the metal, thus the higher photon flux is in principle almost entirely available in the far-field. In conclusion, the enhancement of the radiative emission with negligible losses in the nanostructure (less than 5%) together with the ability of collect light from both sides of the doped film, makes NHA very promising for realization of new photonic devices.

4 Er^{3+} luminescence enhancement by interaction with Au sub-nanoclusters

4.1 Introduction

Strong limitations to the realization of efficient Er-based optoelectronic devices are related to the small cross-section for Er excitation, which is typically of the order of $10^{-21} - 10^{-19}$ cm^2, depending on the matrix [8, 9, 18]. The interaction with sensitizing species to enhance the Er pumping efficiency represents a possible solution to this problem and different approaches have been explored in these years using other rare-earths [19–21], silicon nanocrystals [22–27], organic complexes [28–32] or metallic nanostructures [33–39]. Concerning metallic nanoclusters (NCs), recent works have demonstrated that ultra-small molecular-like Au nanoclusters (made of less than 20 atoms) act as very efficient sensitizers for the Er emission and the dominant pumping mechanism for the Er ions was demonstrated to be a non-resonant energy-transfer process mediated by the broad-band interband absorption of the sub-nanometer Au clusters. The absorbed energy is then partially transferred to a nearby Er ion that subsequently de-excites radiatively at 1.54 μm. Plasmonic field enhancement effects due to the metallic nanoparticles as well as a possible role of implantation-induced defects on the Er sensitization process have been also ruled out in [38, 39, 72].

However, the energy-transfer is a complex process that is expected to depend on a variety of factors, involving the Au clusters (size distribution, numerical density, cluster structure), the Er site and the matrix structure. In a very recent work, by studying the luminescence properties of molecule-like Au nanoclusters obtained by ion implantation in silica it was suggested that the process is triggered by the formation of an Au-related luminescence band, resonant with the corresponding Er^{3+} absorption level, that acts as a preferential de-excitation channel through which the energy is transferred from the Au NCs to the Er ions. [73] Nevertheless, several aspects are still to be clarified concerning the specific role of the synthesis parameters (ion implantation conditions and thermal treatments) and the optimal [Au]/[Er] concentration ratio to obtain the most efficient Er sensitization. In spite of these results, a detailed investigation of the interaction distance that characterize the energy-transfer mechanism from molecule-like Au aggregates to the Er ions as well as the estimation of the characteristic cross-section of the process is still lacking.

The aim of the present chapter is to study in detail the Er-related luminescence properties of Er-Au co-doped silica samples obtained by ion implantation at different fluences followed by thermal treatments in specific atmospheres and to better understand the nature of the energy-transfer process between Au NCs and Er ions. Systematic photoluminescence characterizations (integrated and time-resolved) were performed both for resonant and out-of-resonance Er excitation conditions that allowed to develop a phenomenological model through which the effective cross-section for the energy-transfer as well as the interaction distance of the process could be estimated. Furthermore, structural characterizations of the co-implanted samples were performed by EXAFS analyses to better understand both the Au clustering phenomenon,

the ion induced damage due to the Au implantation and its subsequent recovery as a function of the increasing temperature annealing.

4.2 Er^{3+} sensitizers

Since the topic of the present chapter is the sensitizing effect of Au sub-nanoclusters, a brief summery of the results of the other sensitizing species is presented in the following.

Ytterbium was the first Er sensitizer to be studied, since at λ=980 nm the Yb^{3+} ion has one order of magnitude higher absorption cross-section then Er^{3+} ion. The resonance of the $^2F_{7/2} \rightarrow ^2F_{5/2}$ Yb^{3+} transition with the $^4I_{15/2} \rightarrow ^4I_{11/2}$ Er^{3+} transition makes the energy-transfer process possible. The excitation mediated by the absorption of light by Yb ions and the subsequent energy-transfer to Er is more efficient than the direct Er^{3+} excitation in many host materials. However, the inverse process is also possible (the back-transfer from Er^{3+} to Yb^{3+}) thus reducing the efficiency of the sensitization process; many works have been carried out to minimize this undesirable effect [19–21, 74].

In recent years silicon nanocrystals (Si-NCs) have emerged as efficient Er^{3+} sensitizers in silica [24–27]. When silica is doped with an excess of Si, nanometer-sized Si-NCs can grow and due to the three dimensional confinement of silicon produced by the SiO_2-Si boundary, Si-NCs can emit light in the visible near-IR region. When a Si-rich silica system is co-doped with Er ions, the interaction between the two optically active species gives rise to an intense luminescent emission in the 1.5 μm spectral region. With a fine control on the synthesis parameters of the Si-NCs, the non-radiative channels typically limiting the Er luminescence in bulk silicon (energy back-transfer process) may be drastically reduced. Moreover, indirect excitation of Er photoluminescence via coupling between the absorption bands of the Si-NCs and the Erbium excited states has been demonstrated by a number of groups, revealing that Si-NCs enable the excitation of Er ions at wavelengths away from Er absorption bands. The excitation mechanism starts when a photon is absorbed by the nanocrystal, which generates an bound exciton in the Si-NC. This step is followed by rapid excitation exchange to the Er ions and consequent luminescence at 1.5 μm from the Er^{3+} metastable state. As a consequence, luminescence from Si-NCs is in competition to that from the Er ion and by using a sufficiently high Er concentration Si-NC luminescence can be effectively quenched and Er effective cross-section increased by some orders of magnitude [24, 75].

Another sensitizing method studied for Er ions is the use of organic complexes and molecules to enhance Er radiative properties [28–32]. In this case the advantage could be two-fold: to increase the Er absorption cross-section via energy-transfer processes and to promote Er encapsulation in a polymeric matrix. Even if the results obtained by [29] are very promising, the radiative efficiency is still small due to the quenching effect of -OH groups in organic molecules.

Förster theory of energy-transfer

The interaction process involved in Er-sensitizer coupling is usually discussed in the framework of the Förster theory of energy-transfer process. Here, a short summary of this phenomenon is given, which is helpful for understanding the basic mechanisms involved in Er sensitization. By definition, Förster resonance energy-transfer (FRET) is a non-radiative transfer of an electronic excitation from an excited specie termed as donor (D) to an acceptor (A) that is initially in its ground state:

$$D^* + A \rightarrow D + A^* \tag{4.1}$$

The first theoretical formulation of resonant energy-transfer that successfully identified the inverse sixth power distance dependence (with which the process itself is now almost universally associated) was made by Förster in 1948 [45], and experimentally verified by Latt et al. [76]. Förster's theory develops on an approach based on electric dipole-dipole interaction, which has been extended by Dexter in 1953 [77] to include higher-order multipole interaction. In the framework of Dexter's electronic transfer, the process requires a wave-function overlap between the donor and the acceptor and the coupling carries an exponential decay with the distance.

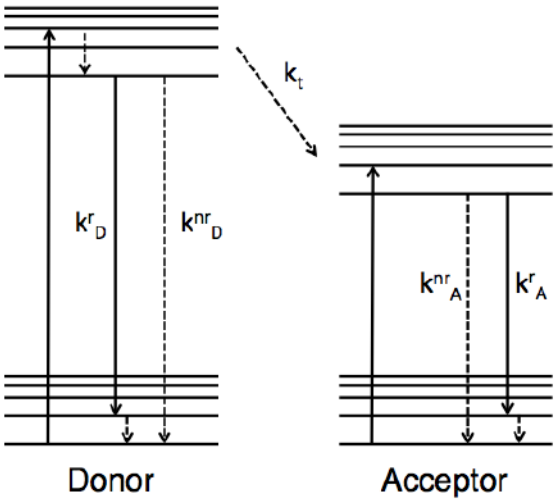

Figure 4.1: Simplified energy scheme of the resonant energy-transfer process. Continuous lines represent radiative decay rates while dashed ones are non-radiative. Subscripts D, A and t stands for donor, acceptor and transfer, respectively.

As schematically illustrated in Fig. (4.1) the process can be summarized as follows: a donor (D) absorbs a photon and generates an electronically excited species (D*). If the acceptor is in the near-field region, the energy released when the electron returns to the ground state may simultaneously excite the acceptor (A*). After the energy-transfer, the excited acceptor decays either in a further transfer event, or by other means such as photon emission (fluorescence). In a simple picture, the near-field volume of an emitter can be represented by a sphere of a radius $0.1\times\tilde{\lambda}$ with

$$\tilde{\lambda} = \frac{\lambda}{2\pi n} \tag{4.2}$$

where λ is the wavelength of the donor luminescence and n represents the refractive index of the matrix material. Considering an Erbium-sensitizer interaction involving Er^{3+} levels in the visible-near-IR spectral region (wavelength range 400-1000 nm) and a refractive index of 1.4–1.6 (typical of silica-based hosts) we can estimate $\tilde{\lambda}$ to be around 100 nm. Therefore the Förster zone represents a sphere with a radius of 5–10 nm around the donor (sensitizer). Acceptors (Er ion) within this range will be a potential partner for the Förster transfer.

In general, for achieving a Förster transfer between a donor and an acceptor the following conditions should be fulfilled:

- the donor and acceptor should have strong transitions from the ultraviolet to near infrared;
- there should be a spectral overlap between the donor and acceptor states;
- the distance between donor and acceptor should be below the Förster zone.

From Fig. (4.1) it can be seen that the transfer efficiency η_t for the energy-transfer is given by the fraction of absorbed energy by the donor which is transferred to the acceptor:

$$\eta_t = \frac{k_t}{k_t + k_D^r + k_D^{nr}} \tag{4.3}$$

where k_t is the transfer energy rate, and the decay rates k_D^r, k_D^{nr} are the radiative and non-radiative decay rates of the donor, respectively.

When the acceptor is in the near-field zone of the donor, the Förster theory gives the following expression for the rate of energy-transfer k_t, in systems where the host material for the donor and the acceptor has refractive index n:

$$k_t = \frac{9c^4\kappa^2}{8\pi\tau_D^0 n^4 R^6} \int F_D(\omega)\sigma_A(\omega)\frac{d\omega}{\omega^4}, \tag{4.4}$$

where $F_D(\omega)$ is the emission spectrum of the donor (normalised to unity), $\sigma_A(\omega)$ is the linear absorption cross-section of the acceptor, R is the donor-acceptor distance, τ_D^0 is the lifetime of the excited donor in the absence of transfer ($\tau_D^0 = 1/(k_D^r + k_D^{nr})$), c is the speed of light and κ depends on the orientations of donor and acceptor with respect to each other (for randomly orientated dipole moments $\kappa^2 = 2/3$). The integral in the equation (4.4) account for the spectral overlap between the donor emission spectrum and the acceptor absorption spectrum.

The Förster rate equation is often cast in an alternative equivalent form,

$$k_t = \frac{1}{\tau_D^0}\left(\frac{R_0}{R}\right)^6 \tag{4.5}$$

where it is introduced the concept of a critical distance (R_0), a separation at which the energy-transfer rate (k_t) and the decay rate ($k_D^r + k_D^{nr}$) by the donor are equal (known as the Förster distance). The associated transfer efficiency (η_t) becomes:

$$\eta_t = \frac{1}{1 + (R/R_0)^6} \tag{4.6}$$

In conclusion, it can be pointed out that, for a fixed κ and n, the transfer efficiency η_t increases with increasing quantum efficiency of the donor (sensitizer) and with increasing the overlap of the respective optical spectra, and it decreases rapidly (R^{-6}) with the distance between the interacting objects.

4.3 Energy-transfer from Au NCs to Er^{3+}

Sub-nanometric molecule-like gold nanoclusters have been proven to be efficient sensitizers for the Er^{3+} photoluminescent emission in silica matrices through a non-resonant broad-band energy-transfer mechanism [39]. In a very recent work reported in Ref. [73] it was demonstrated that such energy-transfer process is triggered by the formation of a near-infrared luminescence band (at 980nm) related to the ultra-small Au nanoclusters that, being resonant with the corresponding Er^{3+} absorption transition ($^4I_{15/2} \rightarrow ^4I_{11/2}$), represents a preferential channel for the transfer of electromagnetic energy to the Er^{3+} ions.

Two distinct paths have been envisaged for this process. In the first case the energy-transfer may occur in a non-radiative way (i.e., not involving emission of photons) by short-range mechanisms as multipole-multipole interactions (Förster mechanism [45]) or exchange processes (Dexter mechanism [77]) owing to the overlap of the wavefunctions associated to the 980 nm band of the ultra-small Au clusters and the $^4I_{11/2}$ level of the Er^{3+} ions. In the second case a long-range interaction may occur mediated by the radiative de-excitation of the Au nanoclusters through their luminescent emission at 980 nm and the subsequent absorption of the emitted photons by the Er^{3+} ions. Recently Julsggard and co-workers [78] demonstrated that for the Er sensitization by Si nanocrystals the coupling occurs at short-range with a characteristic interaction length comparable to interatomic distances.

The present section is therefore focused on the elucidation of the photophysical nature of the energy-transfer process between molecule-like Au nanoclusters and Er^{3+} ions in order discriminate between radiative or non-radiative processes, short- or long-range coupling.

4.3.1 Sample synthesis

For this study the samples have been synthesized with the following approach. First, sequential Er implantations were performed on silica slabs (Infrasil by Haereus) at three energies (50, 100 and 190 keV) with an Er total fluence of 2.7×10^{14} Er^+/cm^2. An almost flat Er concentration profile about 70 nm thick, centered at about 60 nm below the slab surface is obtained in this way. After the Er implantations a further silica layer was deposited by radiofrequency magnetron sputtering on two selected samples. The thickness of this layer was of 35 nm and 160 nm, respectively (as measured by a profilometer). All the Er-implanted samples were then annealed at 800 °C in N_2 atmosphere for 1 hour. This thermal treatment is used both to completely recover the samples from Er implantation damage and restore the Er octahedral coordination necessary for its efficient luminescent emission, but also to adjust the sputtered silica layer from possible deposition defects and under-stoichiometry effects. Triple energy (60, 110 and 190 keV) Au implantations were then performed on the samples at a total Au fluence of 6.7×10^{14} Au^+/cm^2. Subsequently, the samples were thermally treated at 650 °C in N_2 atmosphere for 1 h to induce the Au implantation damage recovery and to promote the formation of Au nanoclusters in the silica matrix. The sputtered SiO_2 layer acted as a spacer for the Au implantations and its thickness was properly chosen to obtain three samples characterized by a different degree of overlap between Er and Au concentration profiles: complete overlap (no silica spacer, sample A), partial overlap (35 nm spacer, sample B) and complete separation (160 nm spacer, sample C). A schematic representation of the samples' structure is shown in Fig. 4.2.

The Er and Au total fluences were estimated by Rutherford Backscattering measurements (RBS) while the concentration profiles were obtained by SRIM simulations [48]. The Er-

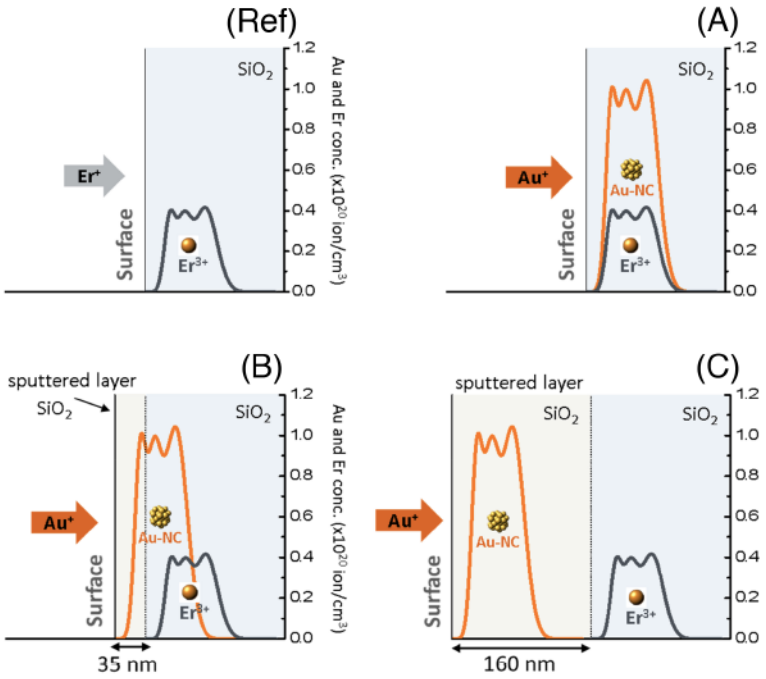

Figure 4.2: Schematic representation of the samples' structure: (Ref) reference sample (no Au implantation); (A) no sputtered SiO_2 spacer (complete overlap between Er and Au concentration profiles); (B) 35 nm SiO_2 sputtered layer (partial overlap); (C) 160 nm SiO_2 sputtered layer (complete separation between Er and Au concentration profiles).

implanted sample annealed at 800 °C (i.e., before the silica sputtering deposition and the Au implantations) was also characterized and it will be referred to in the following as the reference sample.

4.3.2 PL intensity as a function of spacer thickness

To characterize the Er^{3+} luminescent emission properties of the samples and investigate the interaction mechanisms between the Er ions and the Au nanoclusters, photoluminescence (PL) measurements were performed (both integrated and time-resolved) at room temperature using resonant (at 488 nm) and out-of-resonance (at 476.5 nm) Er excitation conditions. The experimental set-up is described in section 1.3.1

Fig. 4.3 shows the room temperature PL spectra of the different samples measured in the wavelength range 1450–1650 nm for resonant (closed symbols) and out-of-resonance (open symbols) pumping conditions. Since a lower power was delivered by the laser at 476.5 nm than at 488 nm, to allow for a direct comparison the spectra are rescaled to the power at 476.5 nm. The spectra of the Er-implanted reference sample were also measured at both pumping conditions resulting completely overlapped to those of sample C (thickest spacer) and thus they are not reported in Fig 4.3. For resonant excitation conditions all the samples exhibit the characteristic PL band at 1540 nm related to the $^4I_{13/2} \rightarrow {}^4I_{15/2}$ Er^{3+} transition in silica. The intensity of this band increases by decreasing the thickness of the sputtered SiO_2 layer. With respect to the reference sample (or equivalently to sample C) an increase of the integrated PL signal of a factor of 5 in the sample without the sputtered silica layer (sample A) was measured. This enhancement of the Er^{3+} luminescence is consistent with the sensitization

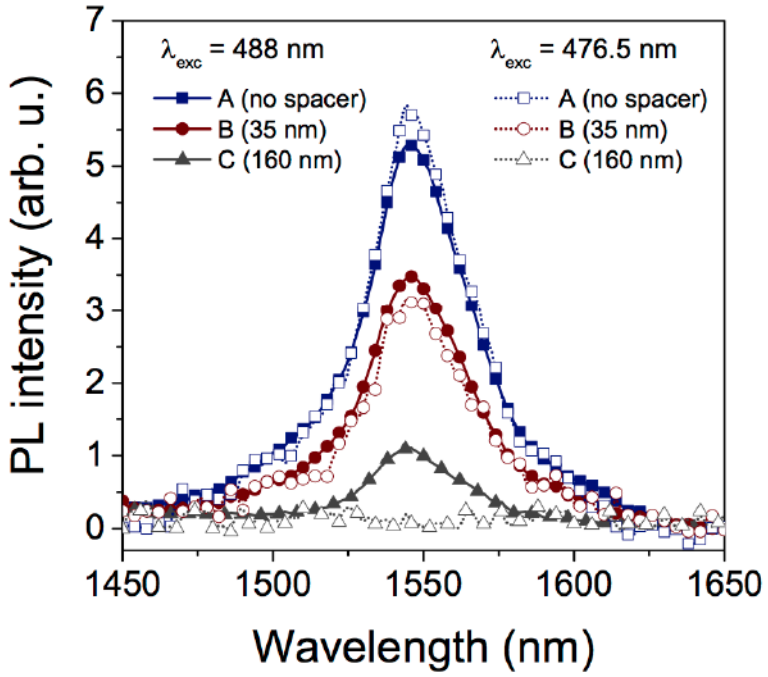

Figure 4.3: Room temperature Er^{3+} PL emission spectra of the samples resonantly excited at 488 nm (closed symbols) and with out-of-resonance pumping conditions at 476.5 nm (open symbols). The spectra are normalized to the same pump power. The labels report in brackets the thickness of the SiO_2 sputtered layer. For both excitation conditions the spectra of the Er-implanted reference sample overlapped completely to those measured from sample C.

effect obtained in [36,39] from similar Er-Au co-implanted systems and that was demonstrated to be induced by the formation upon annealing of sub-nanometric Au aggregates that act as sensitizers for the Er emission. This effect is further confirmed by the PL results obtained for out-of-resonance pumping conditions. Indeed, while no PL emission was revealed from the reference sample for non-resonant excitation at 476.5 nm, the PL signal detected from sample A by pumping at this wavelength resulted even more intense, in agreement with the slightly higher Au absorption cross-section at 476.5 nm than at 488 nm. A markedly different behavior was observed instead from sample C (i.e., the sample with the thickest silica spacer). As mentioned above, for both excitation conditions the PL spectra collected from this sample were identical to those of the reference sample. No enhancement effect of the Er^{3+} luminescent emission was observed in this case. This suggests that the thickness of the sputtered silica layer in this sample is large enough to hinder the interaction between Au nanoaggregates and Er ions: the overlap between the Er- and Au-containing regions is necessary for the ultra-small Au nanoclusters to "talk" to nearby Er^{3+} ions and thus for the energy-transfer process to occur. Further insights on this mechanism can be obtained by analyzing the luminescence properties of sample B in which a partial overlap between the Er and Au concentration profiles is obtained. As shown in Fig. 4.3 the behavior of this sample is intermediate between that of sample A and sample C.

To highlight this effect and get quantitative information in Fig. 4.4 is reported the integrated PL emission measured at 1540 nm as a function of the photon flux for the three samples. In the explored range the PL intensity scales linearly with the photon flux. The solid and dashed lines are linear fits of the experimental data measured with resonant excitation at 488

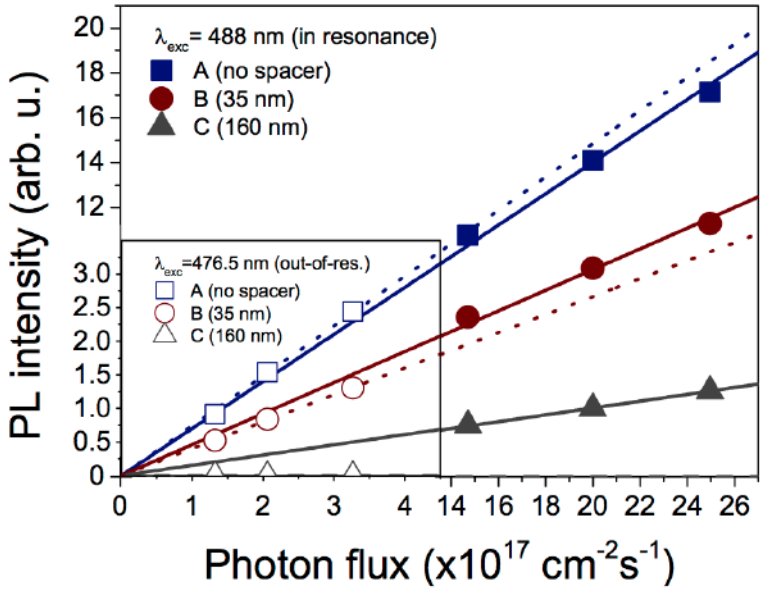

Figure 4.4: PL emission at 1540 nm as a function of the photon flux of the samples resonantly excited at 488 nm (closed symbols) and with out-of-resonance pumping conditions at 476.5 nm (open symbols). The solid and dashed lines are linear fits of the data measured with excitation at 488 nm and 476.5 nm, respectively.

nm (closed symbols) and non-resonant pumping at 476.5 nm (open symbols), respectively. Interesting considerations can be derived analyzing the results obtained for excitation at 476.5 nm. At this wavelength the only excitation mechanism of the Er^{3+} ions is the indirect pumping mediated by the energy-transfer from the Au nanoclusters. Moreover, the PL emission intensity is proportional to the fraction of optically active Er ions in the sample that can be indirectly excited through the energy-transfer process. Up to the highest pumping intensities, no luminescent emission can be revealed from sample C for these excitation conditions, that is no Er^{3+} ion can be reached by the transfer of energy from the Au nanoclusters as a consequence of the separation distance between the Er and Au concentration profiles. Concerning sample B instead, it is worth noting that the ratio between the slope of the linear trend in the PL intensity as function of the photon flux of sample B (red dashed line) and sample A (blue dashed line) results 0.54±0.05. This value can be considered as the fraction of Er^{3+} ions indirectly sensitized by the Au nanoclusters that are present in sample B with respect to the total number in sample A and results consistent with the ratio between the areas of overlap of the Er and Au concentration profiles in the two samples (about 0.5). Therefore, due to the partial overlap between Er and Au concentration profiles sample B can be considered as composed by a linear combination of sample A and sample C: $I_B = w_A I_A + w_C I_C$, with weighting factors w_A=0.54 and w_C=0.46 (w_A+w_C=1) A further confirmation of this scenario can be found in the PL intensity results of sample B obtained for excitation at 488 nm (red dots). As shown in Fig. 4.4 the slope of the linear fit obtained in this case (red solid line) is higher than that at 476.5 nm. For resonant pumping at 488 nm indeed the Er^{3+} ions can be excited directly by the laser beam through the $^4I_{13/2} \rightarrow ^4I_{15/2}$ Er absorption transition. The higher slope measured at this wavelength in sample B therefore accounts for the contribution to the PL emission of the fraction of optically active Er ions that are outside the overlap region between the Er and Au concentration profiles, or, in other words, from the part of sample C

that composes sample B.

4.3.3 Er^{3+} lifetime at λ=1540 nm

The lifetime measurements performed on these samples give further support to this description. In Fig. 4.5 is reported the temporal decay curves of the PL emission at 1540 nm obtained from time-resolved PL measurements of the samples excited at 488 nm. Same results were obtained also for excitation at 476.5 nm, but due to the lower laser intensity available at this wavelength the measurements were characterized by a lower signal-to-noise ratio and have not been plotted. A stretched exponential function of the form

$$I_{PL}(t) = I_{PL}(0)\mathbf{exp}\left[-\left(\frac{t}{\tau}\right)^{\beta}\right] \tag{4.7}$$

was used to fit the the experimental data, with τ and β used as free parameters. In the expression, τ is the PL lifetime while β is the stretching factor, which ranges between 0 and 1. The stretched exponential describes the PL decay curve of a population of emitters whose decay rates distribution is Gaussian. Therefore the stretching parameter describes the dispersion in the excited state lifetimes, which is a signature of an inhomogeneous Er population given by the distribution of Er-Au NCs distances. The solid lines are the best-fitting results to the experimental data according to the equation (4.7). When the stretched exponential is used, the effective lifetime (τ_{eff}) can be calculated through the function:

$$\tau_{eff} = \frac{1}{I_{PL}(0)}\int_0^{\infty} I_{PL}(t)dt = \frac{\tau}{\beta}\Gamma\left(\frac{1}{\beta}\right). \tag{4.8}$$

where Γ is the Eulerian gamma function. Sample A is characterized by an effective lifetime $\tau_{eff,A} = 6.4 \pm 0.4$ ms ($\beta = 0.84$). Conversely a single exponential decay ($\beta = 1$) was measured from sample C with a longer lifetime $\tau_{eff,C} = 10.9 \pm 0.6$ ms. The shortening effect on the lifetime observed in sample A is consistent with the results obtained from similar Er-Au co-implanted samples and has to be ascribed to the co-presence in the Er-containing region of Au nanoclusters that act as sensitizers for the Er emission. The formation of non-radiative recombination centers related to implantation-induced defects have been ruled out for these systems [72].

The lifetime of the Er reference sample was also measured and reported in Fig. 4.5 (green curve). A single exponential fit was done in this case obtaining $\tau_{ref} = 13.8 \pm 0.6$ ms. It is worth noting that such long lifetime is consistent with the Er^{3+} emission lifetime reported by Polman and co-workers [8] for low concentration Er-doped silica systems, indicating the absence of concentration quenching effects in our sample due to the low Er implantation fluence (corresponding to a peak Er concentration below 0.2 at.%) as well as of residual implantation damage not completely annealed out by the 800 °C thermal treatment that may couple to the Er ions opening non-radiative decay channels. With respect to the reference sample, sample C is characterized by a slightly shorter lifetime. This shortening effect is due to the sputtering deposition of the silica spacer that changes the refractive index of the medium just above the Er implanted region and thus the radiative lifetime, as already discussed in section 2.4.1. Instead the presence of a damage tail related to the subsequent Au implantation can be ruled out: the same lifetime was measured from sample C before and after Au implantations. Finally concerning sample B, its PL temporal decay (gray curve in Fig. 4.5) is well represented

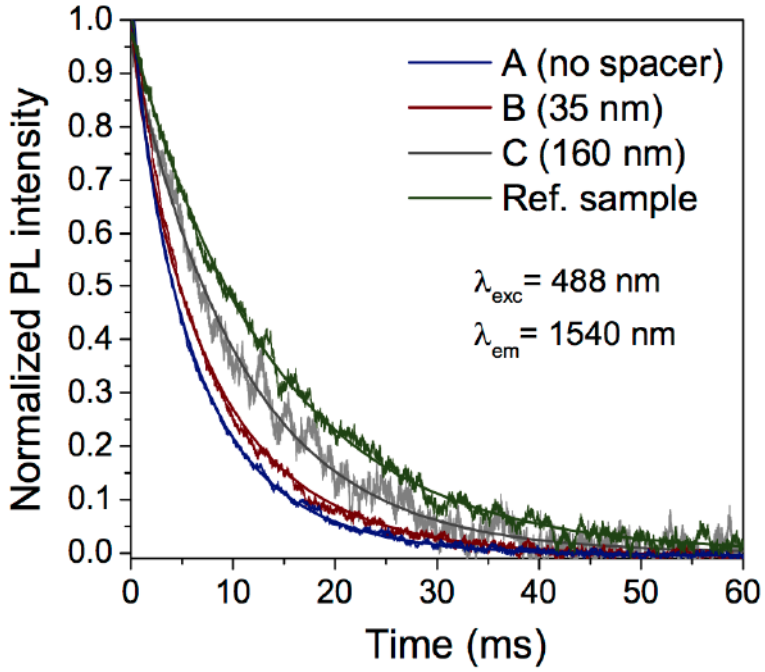

Figure 4.5: Temporal decay curves of the PL signal at 1540 nm for the different samples, resonantly excited at 488 nm. The time decay curve of the Er-implanted reference sample is also reported for comparison. The solid lines are best-fits to the experimental data.

by the linear combination of the results of samples A and C with the same weighting factors (w_A and w_C) obtained from the measurements of the integrated PL emission (Fig. 4.4), thus further confirming the description of sample B as formed by two components: about half of the sample behaves as sample A and the other half as sample C.

4.3.4 Energy-transfer as short-range interaction

Fig. 4.6 shows a schematic representation of the Er^{3+} PL emission at 1540 nm of the three samples for the two indicated excitation conditions: in-resonance (upper panel) and out-of-resonance (lower panel). The data are shown as a function of the Er and Au coupling ratio, i.e., the intersection area between the Er and Au concentration profiles (gray area) relative to the total Er-containing region. As mentioned above, the Er^{3+} ions can emit as a consequence of both direct (resonant) excitation and indirect (non-resonant) sensitization through the energy-transfer mediated by the Au nanoclusters. The two mechanisms are highlighted in Fig. 4.6 with blue and gray arrows, respectively. For the different pumping conditions the behavior of the samples results by the combination of these two processes. In sample A the dominant excitation mechanism for the Er^{3+} ions is the indirect Au nanoclusters-mediated sensitization and occurs with the same efficiency for both pumping conditions. On the contrary, in sample C the Er^{3+} PL emission occurs only for direct excitation at resonant pumping. No luminescence can be detected for out-of-resonance excitation. The separation distance between the Er and Au-containing regions in this sample (160 nm) is large enough to prevent any indirect excitation of the Er^{3+} ions by the Au nanoclusters. As a consequence, this demonstrates that the energy-transfer process from the Au nanoclusters to the Er ions is a short-range coupling mechanism and can be described in the framework of the Förster energy-transfer theory.

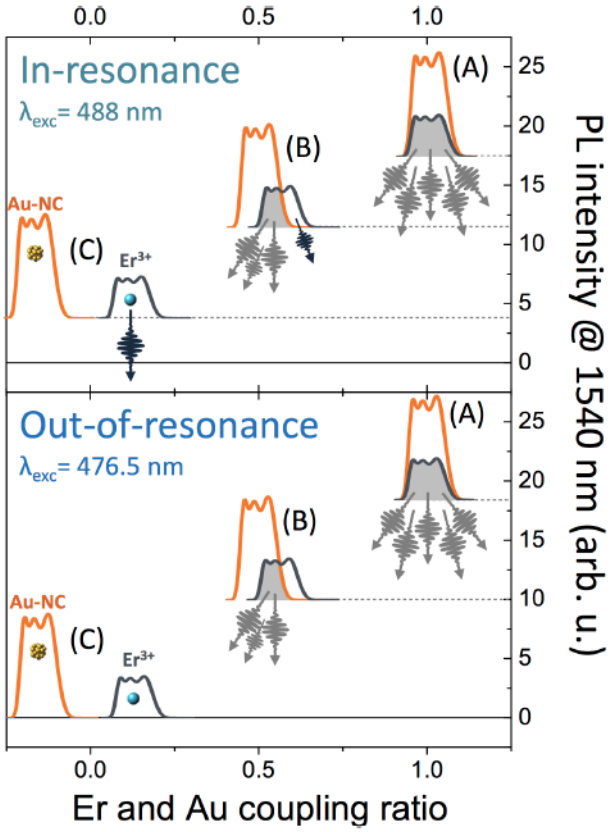

Figure 4.6: Schematic representation of the PL emission at 1540 nm of the three samples as a function of the Er and Au coupling ratio for resonant (at 488 nm, top panel) and non-resonant (at 476.5 nm, bottom panel) Er^{3+} excitation conditions.

Long-range interaction effects as those mediated by the emission of photons from the Au nanoclusters subsequently absorbed by the Er ions can be ruled out. Further confirmations of the short-range nature of the energy-transfer process arise from the results obtained for sample B (partial overlap). This sample can be effectively described as formed by two parts that behave independently: the portion of sample B corresponding to the overlap region (gray area) behaves as sample A, while the remaining fraction (white area) acts as sample C. The PL signal of this sample results by the combination of the luminescence properties of sample A and sample C weighted on the corresponding geometrical proportions. In particular, for out-of-resonance excitation conditions at 476.5 nm the PL emission arises only from the Er^{3+} ions that are present in the overlap region (gray area); those lying outside this region (white area) do not contribute to the PL signal: they cannot be directly excited due to the non-resonant pumping, nor they are indirectly sensitized by the Au nanoclusters. This result is particularly important since it reinforces the statement that the energy-transfer mechanism from the Au nanoclusters to the Er ions is a short-range interaction process demonstrating that the coupling length has to be of the order of the interatomic distances.

4.4 The role of Au NCs size and density on Er^{3+} PL enhancement

In the present section several aspects concerning the determination of the best conditions (in terms of implantation parameters and thermal treatments) to maximize the Er sensitized emission will be discussed. In particular it will be investigated in detail how the ratio between the Au/Er implanted dose can influence both the PL intensity and the lifetime of the Er radiative emission at λ=1540 nm. The optical properties will also be related to the annealing temperature and atmosphere to elucidate the relation between the PL enhancement and the Au NCs growth in silica, using EXAFS analysis to have a structural characterization of selected set of samples. Moreover, the Er^{3+} effective excitation cross-section and the interaction distance were estimated from the characterization of the PL intensity as a function of pumping photon flux.

4.4.1 Sample synthesis

Triple energy (60, 110 and 190 keV) Au implantations were performed on silica slides (Herasil I by Haereus) that were previously implanted with Er at a total fluence of 6.7×10^{14} cm^{-2} and annealed at 800 °C in N_2 atmosphere, to activate the luminescence of the Er ions, otherwise hindered by the implantation-induced defects (as discussed in section 1.4.2). Er and Au implantations produce an almost constant concentration profiles of the two elements in an implanted region about 70 nm thick. With this implantation scheme the overlap of the Au and Er depth profile is obtained independently from the ion implantation fluence. Different sets of samples were produced in which the [Au]/[Er] concentration ratio was spanned over the range 0.5–10. The implantation fluences were measured by Rutherford Backscattering Spectrometry (RBS).

After Au implantations the samples were heated at temperatures in the range 300–800 °C in N_2 atmosphere to induce Au clustering and to recover the silica matrix from radiation damage. For the samples with the two extreme concentration ratios ([Au]/[Er] = 0.5 and 10) thermal treatments in reducing atmosphere ($Ar+H_2$) were also performed. An Er-implanted silica sample (annealed at 800 °C in N_2 atmosphere) but without Au doping was used as a reference for the measure of the photoluminescence intensity and decay rate. This reference sample will be indicated as Er800. In the following section the sample label will indicate the Au and Er concentration with respect to Er concentration of the reference sample ($\sim 9.1 \times 10^{19}$ at/cm^3), the annealing temperature and atmosphere: e.g., for the sample Er1Au5-N600 the Er concentration was equal to Er800 sample, while Au concentration was about 5 times higher and the sample was annealed at T=600 °C in nitrogen atmosphere.

Extended X-ray Absorption Fine Structure (EXAFS) experiments were performed at the Au L_3-edge in fluorescence mode at the ID26 beamline of the European Synchrotron Radiation Facility (Grenoble, France). The monochromator was equipped with a couple of (111) Si crystals; a couple of multi-segmented piezoelectric bimorph mirrors allowed to reject harmonics and to focus the beam onto the sample. The samples were cooled at 20 K to avoid radiation damage and to reduce as much as possible thermal vibrations.

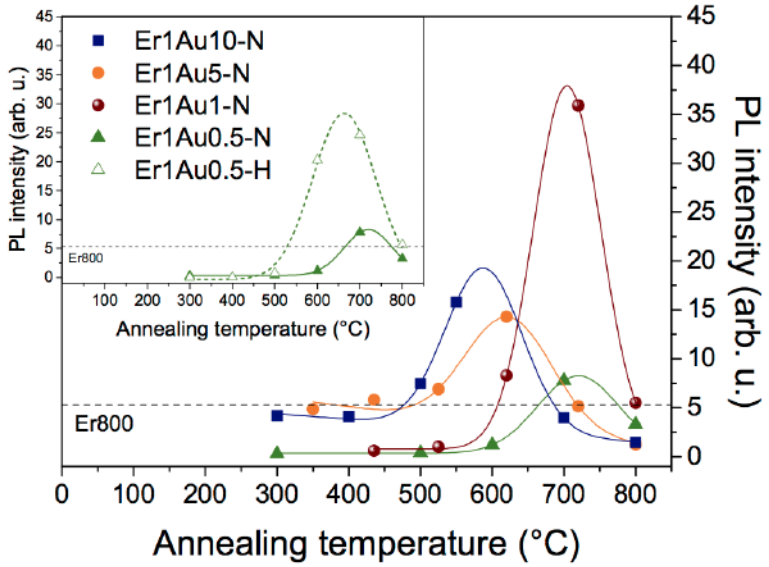

Figure 4.7: Room temperature PL emission at 1540 nm (resonantly excited at 488 nm with a pump power of 22 mW) as a function of the annealing temperature for Er-Au co-implanted samples thermally treated in inert N_2 atmosphere. Inset: comparison of the PL emission trend of the Er1Au0.5 samples annealed in inert N_2 atmosphere (Er1Au0.5-N) and reducing $Ar+H_2$ atmosphere(Er1Au0.5-H). The solid lines are Gaussian fits as described in the text. The legend reports the nominal [Au]/[Er] concentration ratio. The horizontal dashed lines indicate the PL intensity of the Er800 reference sample.

4.4.2 Influence of Au NCs size and distribution on PL intensity

Fig. 4.7 reports the evolution of the room temperature PL emission intensity measured at λ=1540 nm as a function of the annealing temperature for the Er-Au co-implanted silica samples thermally treated in nitrogen atmosphere. For all the sample series the Er peak concentration was $\sim 9.1\times10^{19}$ at/cm^3, while Au concentration was varied from 4.3×10^{19} at/cm^3 to 9.6×10^{20} at/cm^3 in order to obtain [Au]/[Er] concentration ratios that span over more than one order of magnitude. The PL measurements have been performed with resonant excitation at λ=488 nm, as described in section 1.3.1. The inset shows the comparison of the PL emission trend for the samples with the lowest implantation dose (Er1Au0.5 series) annealed in inert (N_2) and reducing ($Ar+H_2$) atmospheres. The horizontal dashed line indicates the PL signal of the reference sample (Er800), that is the Er-doped silica sample prior to Au implantation.

In the whole range of Au concentrations explored and for both annealing atmospheres, the temperature evolution of the PL intensity is characterized by an increase up to a maximum value, and a subsequent significant decrease down to PL signals similar to or lower than the value of the reference sample. In order to reproduce this trend the experimental data were fitted with a Gaussian function (solid lines in Fig. 4.7). For the samples with the highest Au concentrations (Er1Au5 and Er1Au10) a polynomial background has been also added to the Gaussian function to fit the low temperature data. This background is needed to account for the PL signal that can be measured in these samples already at low annealing temperatures (T<500°C) which is instead negligible in the samples implanted at lower Au fluence (Er1Au1 and Er1Au0.5 series). These fits have been used as a guide for the eye and to extract the peak parameters (PL peak temperature and peak intensity). The first increase of the PL intensity

has to be related to the progressive aggregation of dispersed Au atoms in small clusters as well as to the recovery of the matrix from radiation damage, while the observed decrease at higher temperatures is related to the further Au cluster growth that reduces the overall number of cluster per unit volume and increases the average size [39]. Both effects promote a progressive reduction of the efficiency in the energy-transfer mechanism because the increase of the average distance between Au NCs and Er ions decreases the Förster like energy-transfer efficiency, and the transition from molecular-like to "bulk" character of the aggregates has been demonstrated to have a detrimental effect on Er sensitization [73]. Nonetheless from the data in Fig. 4.7 it emerges also clearly that both the Au implantation fluence and the annealing atmosphere have a remarkable effect on the temperature evolution of the PL emission, in particular on the peak position (peak temperature) and the maximum intensity.

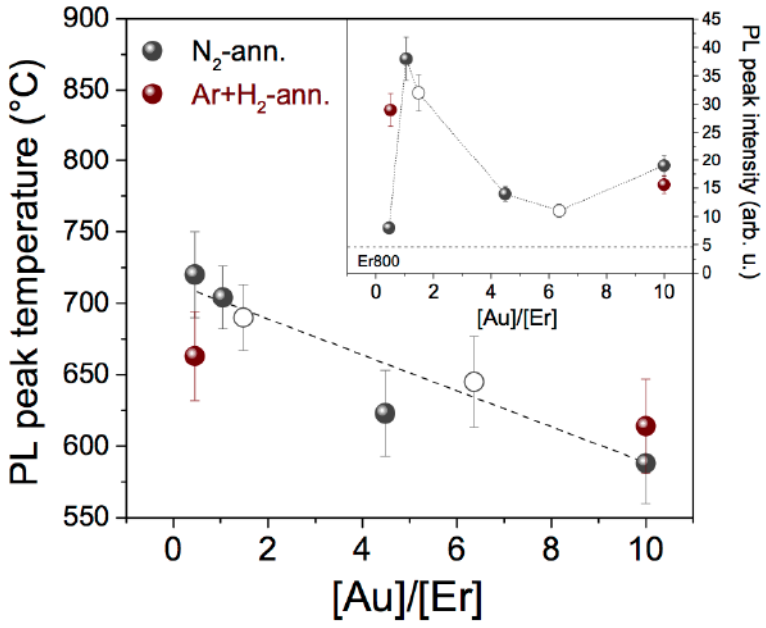

Figure 4.8: PL Peak temperature (main panel) and PL peak intensity (inset) as a function of the [Au]/[Er] concentration ratio of sample series annealed in N_2 atmosphere (gray dots) and Ar+H_2 atmosphere (red dots). The open circles are the data obtained from the two sample series Er0.7Au1 and Er0.7Au5.

In order to analyze this effect the PL peak temperature and the peak intensity obtained from the Gaussian fits were plotted as a function of the [Au]/[Er] concentration ratio in Fig. 4.8. The open circles represent the results obtained from two different series of Er-Au co-implanted samples (Er0.7Au1 and Er0.7Au5) annealed in N_2 atmosphere in which Er was implanted at a lower fluence (4.7×10^{14} cm^{-2}). These data can be treated consistently with those of all the other sample series confirming that the mechanisms to be considered are indeed dependent on the relative concentration of Au sensitizers and Er ions and independent of the absolute Er concentration when it is kept below the concentration quenching limit. As shown in Fig. 4.8, the peak temperature is characterized by a monotonic decrease for increasing the [Au]/[Er] ratio. The dashed line is a linear fit of all the data relative to samples annealed in nitrogen atmosphere (gray dots and open circles). This result can suggest that the thermal energy required to obtain the optimum Au NCs size distribution decreases linearly with the increase of the Au relative concentration. The data of the samples annealed in Ar+H_2 atmosphere

(red dots) seem to lie on a similar linear trend but with a smaller slope, probably because the reducing atmosphere decreases the Au clustering rate in silica [39]. On the contrary, the evolution of the peak intensity as a function of the relative Au concentration with respect to Er (see inset in Fig. 4.8) is definitely not monotonic but exhibits a maximum for an [Au]/[Er] ratio equal to 1, i.e., when the Au concentration equals the Er one. It is worth highlighting that selecting properly the [Au]/[Er] ratio and the annealing temperature the PL signal of the characteristic $^4I_{13/2} \rightarrow ^4 I_{15/2}$ Er^{3+} radiative transition can be enhanced by an order of magnitude.

In order to get structural information on the samples, x-ray absorption spectroscopy measurements (EXAFS) of some selected Er-Au co-implanted samples have also been performed. The data show a progressive increase of the average Au cluster size in the samples by increasing the annealing temperature and, for a given temperature, by increasing the Au implantation fluence. Au clusters made of about 50 atoms are formed in the Er1Au10-N800 sample, representing the largest NCs produced in all the sample series. By comparing the PL results with the EXAFS data it emerges that for each sample series the maximum of the Er^{3+} luminescence is obtained at annealing temperatures that induce the formation of ultra-small Au nanoclusters made of less than 10–20 atoms. Moreover, the maximum of the PL emission corresponds to the formation of Au clusters whose average size decreases by decreasing the Au implantation fluence (i.e., about 20 atoms for the series Er1Au10-N, 17 atoms for Er1Au5-N and about 10 atoms for Er1Au0.5-N). This behavior can be understood taking into accounts that the Au implantation process followed by thermal treatments is expected to induce the growth of Au clusters with a distribution of sizes that is dependent on the Au fluence being narrower for lower Au concentrations, thus resulting in an average Au cluster size, as estimated by EXAFS, smaller for lower Au fluences. All these results allow to clarify the trend of the PL peak temperature shown in Fig. 4.8. The increase of the peak temperature for decreasing [Au]/[Er] concentration ratios is indeed related to the growth of the Au NCs in the optimal size range for the Er sensitization (10–20 atoms) that occurs at increasing annealing temperatures for decreasing Au concentrations.

4.4.3 Influence of Au NC size and distribution on Er^{3+} lifetime

Further insights into the role of the Au sub-nanometric clusters as Er sensitizers can be gained by studying the temporal decay of the Er^{3+} luminescent emission at 1540 nm. To this aim time-resolved PL measurements were performed on all the investigated samples. Due to its non-exponential character, the PL temporal decay of the samples was fitted with a stretched exponential decay function leaving the lifetime (τ) and the stretching parameter (β) as free parameters for the calculations. The effective lifetime (τ_{eff}) of the Er^{3+} luminescent emission was then estimated through the equation (4.8). In Fig. 4.9 the results of these fittings obtained from the samples annealed in nitrogen atmosphere for resonant pumping conditions at 488 nm are reported. Out-of-resonance (at λ=476.5 nm) lifetime measurements were also performed providing in all cases the same results.

In both panels in Fig. 4.9 the horizontal dashed line indicates the results from the Er800 reference sample. A single exponential decay ($\beta = 1$) was measured in this case with a lifetime τ^*=(10.7±0.2) ms. Considering the data reported in Fig. 4.9(a) it can be observed that for all the sample series the PL effective lifetime increases by increasing the annealing temperature. This behavior is consistent with a progressive recovery upon annealing of irradiation defects that may act as non-radiative recombination centers, thus increasing the probability for the

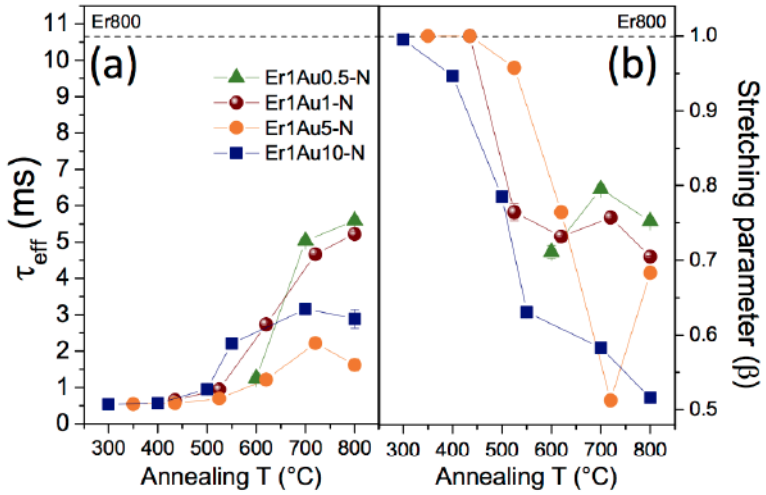

Figure 4.9: (a) Effective lifetime (τ_{eff}) and (b) stretching parameter (β) of the Er^{3+} PL emission at 1540 nm as a function of the annealing temperature for the Er-Au co-implanted samples annealed in N_2 atmosphere. The samples were resonantly excited at 488 nm.

Er de-excitation. It is worth noting that even for the lowest Au fluence (Er1Au0.5 series) it is not possible to completely recover the emission lifetime of the Er800 reference sample. The recovery of the silica matrix due to the implantation damage will be discuss in detail in the next section, but it is worth anticipating that the lifetime shortening due to the not completely recovered silica host does not produce stretched exponential PL decay curves and that at high annealing temperature the damage is fully recovered (i.e. the lifetime reaches the value before ion irradiation). Thus, this shortening effect on the Er^{3+} lifetime in the co-implanted samples has to be ascribed to the presence of Au clusters in the samples acting as Er sensitizers and not to the formation of non-radiative recombination centers related to irradiation defects. Moreover, at the highest annealing temperatures, the samples implanted at lower Au fluences are characterized by a τ_{eff} which is about twice the value determined from the samples implanted at higher Au fluences, probably due to the higher Au cluster size and density in the samples implanted at higher Au fluence. Lastly, it is worth considering that a minor effect due to the modification of the local dielectric environment around the Er ions induced by the presence of the Au nanostructures cannot be definitely ruled out. Nonetheless, due to the ultra-small Au cluster size and the size distribution induced by the Au implantation process, a quantitative estimation *a priori* of such effect is very difficult and its possible role can only be guessed.

Further information can be gained from the values of the stretching parameter (β) determined from the different samples (see Fig. 4.9(b)). The stretching parameter indeed accounts for a dispersion in the relaxation rates of the Er ions caused by local inhomogeneities in the Er ion local environment induced by the Au incorporation [39]. For all the Au fluences investigated, the values of β are close to 1 (single exponential decay) for the samples annealed at low temperatures (T<500 °C) and decrease for increasing annealing temperatures. This suggests that the Au cluster growth occurring at increasing annealing temperatures is accompanied by a corresponding increase of configurational disorder which is more pronounced when the Au fluence is higher. On the other hand, at the annealing temperatures that induce the maximum PL emission of the different sample series the stretching parameter results higher when the

Au concentration is lower, indicating again a narrower dispersion of the Er relaxation rates when lower Au fluences are implanted. Furthermore, it is worth noting that for the lowest Au concentration (Er1Au0.5 series) β results higher upon annealing in reducing atmosphere than in inert one (particularly in correspondence to the maximum of the PL emission), suggesting the presence of a lower configurational disorder in the first case.

4.4.4 Effective cross-section

A very important parameter that characterizes the energy-transfer process from Au NCs to Er ions is the effective cross-section for Er sensitization, σ_{eff}. In the aim of providing an estimation of this parameter for the Er-Au investigated samples, the Er^{3+} luminescent emission at 1540 nm was measured as a function of the photon flux with out-of-resonance excitation (at λ=476.5 nm). For the different sample series the measurements were performed on the samples annealed at the conditions that produce the highest PL emission at 1540 nm, i.e., characterized by the strongest sensitization effect ("best-performing" samples). For out-of-resonance pumping conditions the excitation of the Er ions occurs only indirectly, mediated by the energy-transfer from the Au clusters. From a phenomenological point of view, the process can be described by the following rate-equation [24]:

$$\frac{dN_{\text{Er}}^{*\text{s}}}{dt} = W_{\text{s}} - \frac{N_{\text{Er}}^{*\text{s}}}{\tau}, \tag{4.9}$$

where $N_{\text{Er}}^{*\text{s}}$ is the concentration of excited Er ions sensitized through energy-transfer by the Au NCs and τ is the Er emission lifetime in the Er-Au co-implanted samples, that takes into account both the radiative and the non-radiative lifetime. W_{s} represents the sensitization rate and describes the effective increase in the excited Er population due to the sensitization process from the Au NCs. W_{s} is proportional to the photon flux (ϕ) and can be written in the form $W_{\text{s}}=\sigma_{\text{eff}}\phi\,(f_{\text{s}}N_{\text{Er}} - N_{\text{Er}}^{*\text{s}})$, where σ_{eff} is the effective cross-section when Er ion excitation is mediated by the Au sensitizers, and f_{s} is the fraction of the total population of optically active Er ions (N_{Er}) that can be indirectly sensitized by the Au nanoclusters. By taking the steady-state solution of equation (4.9) and considering that the Er luminescent intensity is proportional to the excited Er population (i.e., $I_{PL} \propto N_{\text{Er}}^{*\text{s}}/\tau_{\text{rad}}$ with τ_{rad} the radiative lifetime of the Er excited state in the Er-Au co-implanted samples, different from the one determined for Er doped silica) the Er PL intensity will be given by the equation:

$$I_{PL}\,(\phi) \propto f_{\text{s}}N_{\text{Er}}\frac{\tau}{\tau_{\text{rad}}}\frac{\sigma_{\text{eff}}\phi}{1+\sigma_{\text{eff}}\tau\phi} = f_{\text{s}}N_{\text{Er}}Q\frac{\sigma_{\text{eff}}\phi}{1+\sigma_{\text{eff}}\tau\phi}. \tag{4.10}$$

Q=τ/τ_{rad} is the quantum yield of the Er emission transition at 1540 nm in the Er-Au co-implanted samples. The effective cross-section σ_{eff} for Er sensitization can be estimated by fitting the experimental data with equation (4.10). As an example in Fig. 4.10(a) the PL intensity is plotted as a function of the photon flux of the samples Er1Au1-N720, Er1Au5-N620 and Er1Au10-N600. The solid lines are the best-fit results according to equation (4.10).

The effective cross-sections estimated for all the "best-performing" samples are reported in Table 4.1. The numerical results have been calculated by using the Er emission lifetimes τ_{eff} reported in Fig. 4.9. The data are plotted in Fig. 4.10(b) versus the [Au]/[Er] concentration ratio. As in Fig. 4.8, different symbols are used to indicate the samples annealed in N_2 atmosphere (gray dots), in Ar+H_2 atmosphere (red dots) and samples with a lower Er content (open circles). The dashed line has to be used as a guide for the eye. The data in Fig. 4.10(b)

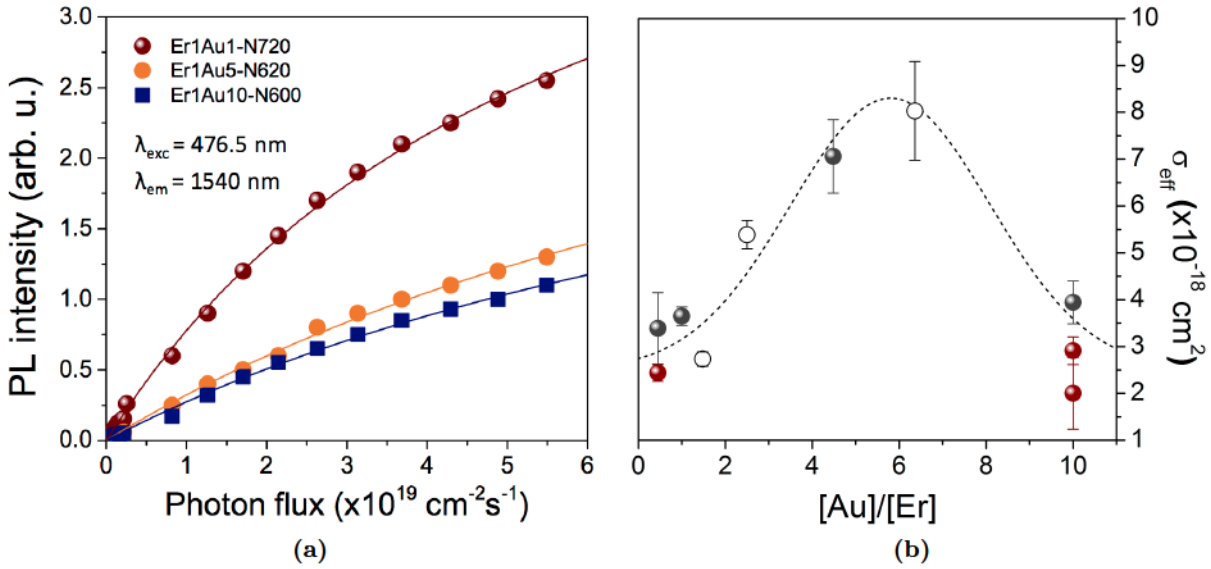

Figure 4.10: (a) PL intensity measured at 1540 nm as a function of the photon flux of the samples indicated in the legend. The measurements have been performed with out-of-resonance excitation at 476.5 nm. The continuous lines are best-fits to the data according to the model described in the text. (b) Effective cross-sections measured at 476.5 nm as a function of the [Au]/[Er] concentration ratio. The values were estimated from the samples that exhibit the maximum PL emission of each sample series. The different symbols indicate samples annealed in N_2 atmosphere (gray dots), in $Ar+H_2$ atmosphere (red dots) and samples with a lower Er content (open circles), respectively. The dashed line is reported as a guide for the eye.

show that the trend of σ_{eff} as a function of the [Au]/[Er] concentration ratio is not monotonic: a maximum (of the order of 8×10^{-18} cm^2) is obtained for a concentration ratio [Au]/[Er] of about 5.

4.4.5 Fraction of sensitized Er ions and Au NCs volume of interaction

For resonant pumping conditions (at λ=488 nm), the excitation of the Er ions may occur through two paths: indirectly, mediated by the energy-transfer from the Au NC sensitizers and directly by the pumping beam through the $^4I_{15/2} \rightarrow {}^4F_{7/2}$ Er^{3+} transition. To account for these two mechanisms, the PL emission intensity at 1540 nm measured by excitation at 488 nm can be written as a function of the photon flux as:

$$I'_{PL}(\phi) \propto f'_s N_{\text{Er}} Q \frac{\sigma'_{\text{eff}}\phi}{1+\sigma'_{\text{eff}}\tau\phi} + f_d N_{\text{Er}} Q \sigma \phi. \tag{4.11}$$

The first term in the right-hand side of equation (4.11) describes the contribution to the PL signal arising from the fraction f'_s of the optically active Er ions indirectly sensitized by the Au nanoclusters, while the second term is introduced to take into account the direct excitation of the remaining fraction f_d ($f'_s + f_d = 1$). In this case the sensitized fraction is indicated as f'_s to distinguish it from the corresponding value in equation (4.10), since different sensitized fractions have been estimated for resonant and non-resonant Er excitation conditions. The explanation of this result will be discussed in detail further in the text. σ'_{eff} is the effective cross-section of the sensitization process for excitation at 488 nm. Since the energy-transfer

Table 4.1: Fitting results according to the model described in the text of the Er-Au co-implanted samples annealed at the conditions corresponding to the highest PL emission at 1540nm. N is the average number of Au atoms per cluster as estimated by linear interpolation of the EXAFS results.

Samples	[Au] [$\times 10^{20}$at/cm^3]	N	σ_{eff} (476.5nm) [$\times 10^{-18}$cm^2]	f_s [%]	f'_s [%]	f_d [%]	Q [%]	R_{int} [nm]	R'_{int} [nm]
Er1Au0.5-N700	0.43	9±3	3.4±0.8	0.50	0.39	99.61	25.70	0.65	0.61
Er1Au0.5-H700	0.43	9±3	2.4±0.2	0.75	0.50	99.50	73.04	0.74	0.65
Er1Au1-N720	1.0	12±4	3.6±0.2	1.00	0.74	99.26	72.92	0.69	0.63
Er0.7Au1-N720	1.0	12±4	2.7±0.2	1.64	1.28	98.72	33.54	0.80	0.74
Er1Au5-N620	4.3	16±6	7.1±0.8	0.29	0.16	99.84	50.54	0.43	0.41
Er0.7Au5-N620	4.3	16±6	8.0±1.1	0.26	0.16	99.84	43.62	0.42	0.40
Er1Au10-N600	9.6	20±10	3.9±0.5	0.73	0.51	99.49	30.28	0.50	0.48
Er1Au10-H600	9.6	11±4	2.9±0.3	1.02	0.67	99.33	27.48	0.40	0.38

process from the Au NCs to the Er ions was demonstrated to be mediated by the broad-band interband absorption transitions of the Au nanoclusters (see Ref. [39]), σ'_{eff} can be related to the value estimated at 476.5 nm (σ_{eff}) considering the expression $\sigma'_{eff} = (\alpha'/\alpha)\,\sigma_{eff}$ with α' and α being the absorption coefficients at 488 nm and 476.5 nm, respectively. For the samples under study a ratio $\alpha'/\alpha = 0.87$ was estimated by UV-VIS absorption measurements. σ is the intrinsic emission cross-section of the Er^{3+} ions for the $^4I_{13/2} \rightarrow {}^4I_{15/2}$ transition.

As an example, in Fig. 4.11 is reported the PL intensity measured at 1540 nm as a function of the photon flux of the sample Er1Au1-N720 (red dots) for excitation at 488 nm. The PL signal of the Er800 reference sample is also reported (gray dots). In this case the PL emission increases linearly with the photon flux in the whole range explored and it behaves according to the following expression:

$$I^*_{PL}(\phi) \propto N_{Er} \frac{\tau^*}{\tau^*_{rad}} \sigma\phi = N_{Er} Q^* \sigma\phi \tag{4.12}$$

where $Q^* = \tau^*/\tau^*_{rad}$ is the quantum yield of the Er800 reference sample. A reasonable estimation of $Q^* = 0.76$ can be obtained considering the measured decay time of the Er800 reference sample and using for τ^*_{rad} the value of 14.1 ms as given by Polman et al. in Ref. [8].

To quantitatively analyze the experimental PL data and determine the more relevant parameters (sensitized fractions, quantum yield, interaction distance), it is necessary to have an independent estimation of the intrinsic emission cross-section of the Er^{3+} ions, σ. Due to the low Er concentration in the samples (below 1 %at.) and the reduced thickness of the Er containing layer (about 70 nm) a direct mesurement of σ is difficult. No deviation from the linear trend and saturation effect was observed in the measurements of the PL emission intensity as a function of the photon flux of the Er800 reference sample up to the highest flux values achievable. Nonetheless an indirect estimation of σ can be obtained applying the Fuchtbauer-Ladenberg approach to the analysis of the Er^{3+} emission spectrum [46], as described in section 1.3.6. The inset in Fig. 4.11 shows the room temperature PL emission spectrum of the Er800 reference sample. By the Fuchtbauer-Ladenberg analysis σ=4.4$\times 10^{-21}$ cm^2 was obtained that is in reasonable agreement with the cross-section values determined with different methods for various Er-implanted photonic materials [8]. As it was expected the value of σ is very low and more than three orders of magnitude lower than the effective cross-section for Er ions sensitization through energy-transfer estimated for the Er-Au co-implanted samples (see Table 4.1)

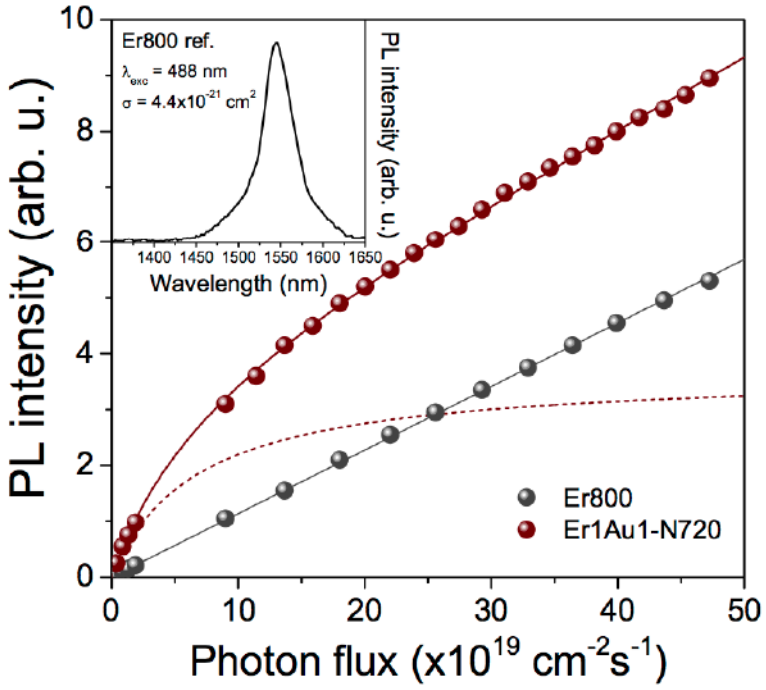

Figure 4.11: PL intensity measured at 1540 nm as a function of the photon flux of the samples Er1Au1-N720 (red dots) and the Er800 reference sample (gray dots). The measurements have been performed with resonant excitation at 488 nm. The continuous lines are best-fits to the data according to the model described in the text. The red dashed line represents the estimated contribution to the total PL signal of the sensitized Er fraction in the Er1Au1-N720 sample.
Inset: Room temperature PL spectrum of the Er800 reference sample.

Given that the measurements of PL intensity versus photon flux of all the investigated samples have been collected with the same acquisition parameters as those used for the Er800 reference sample, for the quantitative analysis of the PL intensity as a function of photon flux at 488 nm, it was chosen to perform best-fittings of the experimental data of the different Er-Au co-implanted samples normalized to that of the Er800 reference. This approach has the advantage of reducing the number of free fitting parameters and as a consequence of strongly improving the stability of the fitting algorithm providing more accurate results. Thus, the following expression was used:

$$\frac{I'_{PL}(\phi)}{I^*_{PL}(\phi)} = f'_{\mathrm{s}}\frac{\sigma'_{\mathrm{eff}}}{\sigma}\frac{Q}{Q^*}\frac{1}{1+\sigma'_{\mathrm{eff}}\tau\phi} + f_{\mathrm{d}}\frac{Q}{Q^*} \tag{4.13}$$

with f'_{s} and Q as the only free parameters ($f'_{\mathrm{s}} + f_{\mathrm{d}} = 1$). A summary of the obtained results for all the investigated samples is reported in Table 4.1. The red solid line in Fig. 4.11 is the best-fit result to the data of sample Er1Au1-N720. The red dashed line shows the contribution to the total PL signal arising from the fraction of Er ions indirectly sensitized through energy-transfer by the Au NCs, i.e., the first term in eq. (4.11). It is worth noting that a further assumption is implicitly done when using equation (4.13) for fitting the experimental data, i.e., that the number of optically active Er ions in the Er800 reference sample (N_{Er}) does not change as a consequence of the subsequent implantation of gold, so being reduced in equation (4.13). This hypothesis is quite plausible for the analyzed samples, which were all annealed at the temperatures that induce the highest PL emission for the different sample series (above

500 °C in all the cases). Therefore, it is assumed that such annealing treatments may be able to restore the number of optically active Er ions to the initial value in the Er800 reference sample. Differently, if this is not the case, the only parameter affected by this assumption is the quantum yield, Q (see Table 4.1), that would be underestimated and can be considered as a lower limit. An important result that emerges from the data in Table 4.1 is that for all the investigated samples the estimated sensitized fractions are very small, below 1%. This means that in spite of the very high sensitization cross-sections demonstrated, the number of Er ions that can be efficiently excited through the energy-transfer from the Au nanoclusters is indeed much limited. Moreover, in all cases the sensitized fractions estimated for out-of-resonance pumping conditions result higher than the values obtained at resonant excitation ($f_s > f'_s$). The physical explanation of this result is given in detail in the following. The other parameter that has been estimated with the fitting procedure described above is the quantum yield of the Er emission transition Q. The results reveal that this parameter is strongly dependent on the [Au]/[Er] concentration ratio. In particular a quantum yields $Q > 70\%$ is estimated for the Er1Au1-N720 sample that has the highest PL enhancement factor. Interestingly, the same result is obtained for the Er1Au0.5-H700 sample while the corresponding sample thermally treated in nitrogen atmosphere (Er1Au0.5-N700) has a value of Q a factor of 3 lower. No effect related to the annealing atmosphere instead appears for the samples of the Er1Au10 series that show in both cases a low quantum yield of about 30%.

In the last two columns in Table 4.1 the interaction distances estimated for excitation at 476.5 nm (R_{int}) and 488 nm (R'_{int}) are reported. The estimation of the interaction distances was carried out considering a random distribution of Er ions and Au clusters in the samples; a quantitative estimation of the interaction volume V_{int} (i.e., the volume containing the fraction f_s of Er ions excited through the energy-transfer from the Au sensitizers) can be obtained according to the relation:

$$V_{int} = \frac{f_s N}{[Au]} = \frac{4\pi}{3}(R_c - R_{int})^3 \tag{4.14}$$

where [Au] is the gold concentration in the samples and N is the average number of Au atoms per cluster determined by EXAFS analyses. A linear interpolation of the EXAFS results obtained at fixed annealing temperature as a function of the Au implantation fluence has been done to determine N for all the investigated samples. The resulting values are reported in Table 4.1. The ratio $[Au]/N$ thus represents the Au cluster concentration in the samples. The second equality in equation (4.14) can be used to determine the interaction radius R_{int} between the Au nanoclusters and the Er ions assuming the interaction volume as a spherical shell around the Au nanocluster. R_{int} represents the maximum distance from the Au nanocluster's surface at which an Er ion can be sensitized. R_c is the average Au cluster radius calculated according to the relation: $R_c = R_a\sqrt[3]{N}$ ($R_a = 0.1505$ nm is the average radius of an Au atom in the cluster) [39]. The interaction radii determined with this method from the different samples investigated in the present work are reported in Table 4.1. For all the samples the resulting values are in the range 0.4-0.8 nm demonstrating that the energy-transfer process from the Au NCs to the Er^{3+} ions is indeed an interaction mechanism occurring at very short-range.

Furthermore, shorter interaction distances were determined for excitation at 488 nm (R'_{int} in Table 4.1) with respect to the values estimated at 476.5 nm (R_{int}). Numerically, this is due to the fact that the sensitized fractions estimated from the analysis of PL data measured at 488 nm result smaller than those evaluated at 476.5 nm for all the investigated samples.

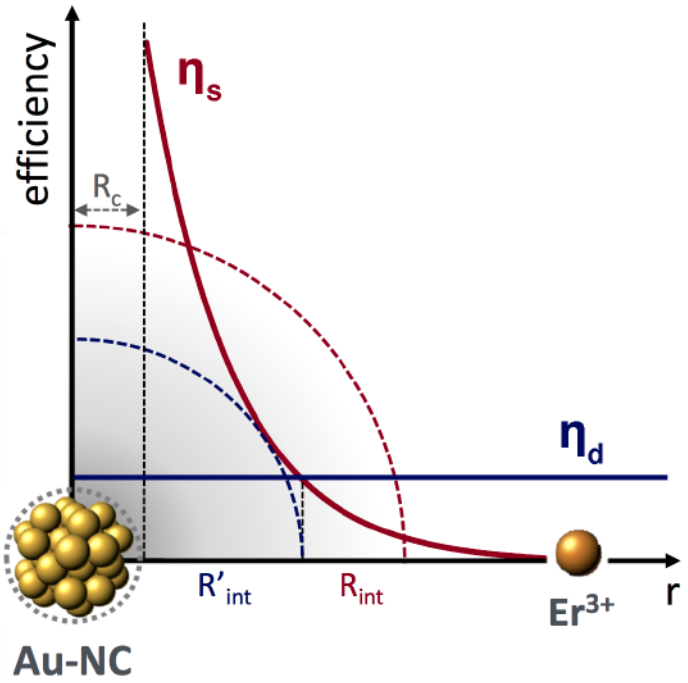

Figure 4.12: Schematic representation of the sensitization efficiency (η_s) as a function of the radial distance r between the Au nanocluster and the Er^{3+} ion. ε_d is the efficiency for direct excitation of the Er^{3+} ions through absorption of the 488 nm pumping beam. R'_{int} and R_{int} are interaction distances estimated for in-resonance (at λ=488 nm) and out-of-resonance (at λ=476.5 nm) excitation conditions. Distances are not in scale.

From the physical point of view, a tentative explanation of this result is sketched in Fig. 4.12. For out-of-resonance pumping conditions (at 476.5 nm) the Er ions are excited indirectly through the energy-transfer from the Au nanoclusters. The efficiency of this process (η_s) is very high due to the large effective cross-section for indirect sensitization, but it is expected to decrease monotonically by increasing the radial distance between the Au nanoclusters' surface and the Er ions (a typical r^{-6} dependence can be considered for dipolar interactions while an exponential decay would be expected for exchange mechanisms [77, 78]). Conversely, for resonant pumping conditions (at 488 nm) the excitation of the Er ions occurs both directly through the absorption of the incoming photons by the Er ions and indirectly, mediated by the energy-transfer from the Au sensitizers. The efficiency of direct excitation (η_d) is much lower than η_s ($\sigma << \sigma_{eff}$) but can be considered constant across the sample. Therefore, at distances from the surface of the Au NCs at which the efficiency for indirect sensitization of the Er ions becomes smaller than the one for direct excitation ($\eta_s(r) < \eta_d$), the direct excitation mechanism prevails. The interaction radius determined from the analysis of PL measurements performed at 488 nm (R'_{int}) can be interpreted in this framework as an estimation of such crossing-point. At non-resonant pumping conditions on the other hand, due to the lack of other competitive mechanisms also the Er ions lying at distances from the Au nanoclusters' surface corresponding to the tails of the efficiency curve contribute to the PL signal giving rise to larger sensitized fractions and interaction radii.

4.4.6 Multi-line excitation

The results reported in this section demonstrated that Au NCs formed upon ion implantation and thermal treatments are very efficient sensitizing agents for Er excitation and acting on the implantation and annealing parameters it is possible to gain up to one order of magnitude of improvement in the Er PL emission at λ=1540 nm. On the other hand, the mechanism of sensitization has been demonstrated to be a non-resonant energy-transfer process from the Au nanoclusters to the Er ions mediated by the broad-band interband absorption of the Au nanoclusters.

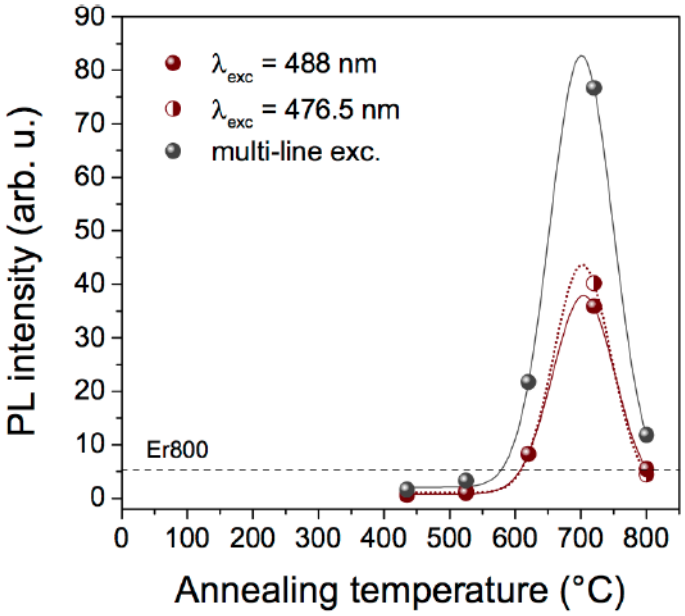

Figure 4.13: PL emission at 1540 nm as a function of the annealing temperature of samples Er1Au1-N for the three different pumping conditions: in resonance (488 nm), out-of-resonance (476.5 nm) and multi-line excitation. The intensities have been normalized to the laser power at 488 nm.

Therefore it is worth to stress the importance of broad-band pumping to gain further enhancements of the Er emission efficiency. This has indeed important technological entailments for the possible applications of these systems in optoelectronic devices. To this aim, in Fig. 4.13 it is reported the PL intensity as a function of the annealing temperature of the Er1Au1-N samples, obtained with different pumping conditions: resonant excitation (at λ=488 nm), out-of-resonance condition (at λ=476.5 nm) and multi-line pumping. In the last case all the emission lines of the Ar laser have been used at the same time to mimic a possible continuous broad-band pumping scheme. To quantitatively compare the intensities, due to the different power of the laser at the different emission wavelengths, the PL signals have been normalized to the laser power at 488 nm. The same behaviour is observed for all the sample series: a slightly higher PL emission at 1540nm is detected at all the annealing temperatures for out-of-resonance pumping conditions with respect to resonant excitation, due to the slightly higher absorption cross-section of the Au clusters at λ=476.5 nm with respect to λ=488 nm. Such effect is strongly amplified when the multi-line pumping is used, with an increase of more than a factor of two in the PL peak intensity, that results in this case in an amplification of the Er emission signal of 17 times with respect to the reference sample.

4.5 Implantation damage effects on the Er^{3+} luminescence in silica

After the investigation on the Er^{3+} photoluminescence properties in the presence of Au NCs, an important point that is still open concerns the possible synergistic role of the defects induced in the silica matrix by the Au implantation on the Er emission. Indeed, when an ion is implanted in a substrate a wealth of complex defective and/or charged configurations are generated along the collisional cascade. The physics and thermodynamics of such defects and their interactions under thermal annealing can largely influence the functional properties of the system. In particular, they could in principle affect both the rare-earth sensitization process and its luminescence quenching. The aim of the present section is therefore to investigate this aspect, by decoupling the sensitization mechanism triggered by the molecule-like Au clusters from the defects creation during Au implantation. For this reason, Er and Xe co-implantations have been performed following the same parameters used to produce the Er-Au co-implanted samples. Xe has been chosen as co-dopant in order to release to the silica matrix an implantation damage as similar as possible to that induced by Au implantation [72].

4.5.1 Sample synthesis

Silica slabs have been implanted with Er ions with the same parameters chosen in the previous section for the reference sample Er800. The sample was then annealed at 800 °C for 1 hour in N_2 atmosphere and a subsequent triple energy (150, 90 and 50 keV) Xe implantation has been performed to overlap the Er depth concentration profile. The implanted dose was $(7.8\pm0.9)\times10^{15}$ Xe^+/cm^2, in order to have and expected implantation damage on Er implanted silica similar to the one induced by the Au^+ implantation with the highest investigated dose (samples labelled Er1Au10 in the previous section). According to simulations obtained with the SRIM-2008 code [48], it has been evaluated that at the energies for the Xe implantation the nuclear and electronic energy losses of Xe in silica are about 30% lower than the corresponding quantities for Au in silica. Therefore to better reproduce the implantation-induced damage a Xe fluence about 30% higher with respect to the Au one was used, resulting in a Xe/Er ratio of about 12. The Er-Xe co-implanted samples were annealed for 1 hour in N_2 atmosphere in the temperature range 300–800 °C.

4.5.2 PL measurements

In order to evaluate the effect of Xe implantation on the Er^{3+} emission properties, both the PL intensity and the lifetime of the Er^{3+} radiative transition at 1540 nm of the Er-Xe co-implanted samples have been measured and compared to the case without Xe implantation. PL measurement were performed with resonant (at λ=488 nm) and non-resonant conditions (at λ=476.5 nm) with the set-up described in section 1.3.1. Xe implantation have been performed on silica slabs previously implanted with Er and annealed for 1 h in N_2 atmosphere at 800 °C. For this annealing condition the Er-implanted samples exhibit a PL intensity close to its maximum value. Nonetheless, after Xe implantation under resonant excitation such luminescent emission is completely suppressed and annealing treatments at temperatures above 600 °C are necessary to restore it. Moreover, the annealing evolution of the PL emission after Xe implantation is comparable with the one measured from the Er-implanted samples, as shown in Fig. 4.14. An analogous behaviour is observed also for the emission lifetimes (see

inset in Fig. 4.14(a)). In this case, only the samples annealed at the highest temperatures, that is 700 °C and 800 °C, exhibited a sufficiently intense luminescent emission to provide reliable estimations of the lifetimes from time-resolved PL measurements. For both fluences the measured lifetimes are close to those obtained in the Er-implanted samples.

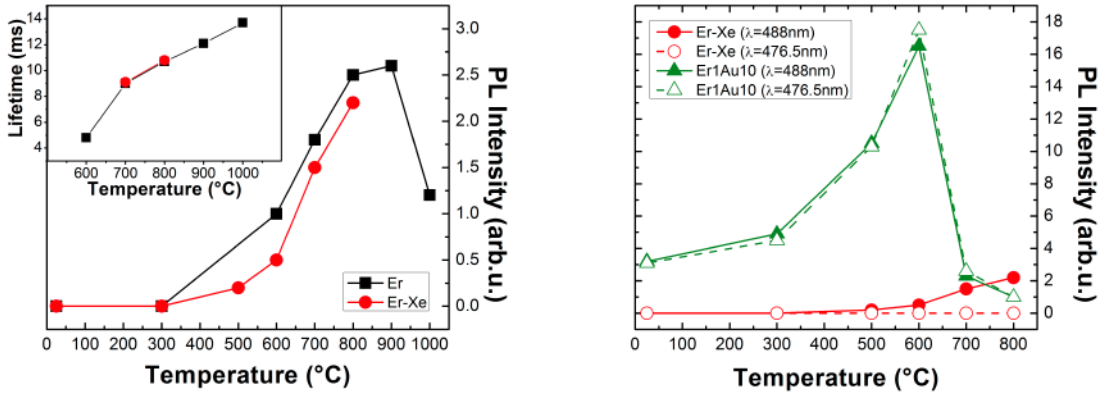

Figure 4.14: (a) PL intensity as a function of annealing temperature for the Er-implanted (black squares) and the Er-Xe co-implanted samples (red circles). The measurements have been performed with resonant excitation at 488 nm. The inset shows the corresponding emission lifetimes. (b) Comparison of the temperature evolution of the PL intensity at 1540 nm for the Er-Xe and Er1Au10 co-implanted samples under resonant (filled symbols) and non-resonant (open symbols) excitation.

As a comparison, in Fig. 4.14(b) is have reported the PL intensity as a function of the annealing temperature for the Er-Xe and the Er1Au10 co-implanted samples under resonant excitation (λ=488 nm). The results show the dramatically different temperature evolution exhibited by the Er-Au co-implanted samples with respect to that of Er-Xe co-implanted ones. For the Er1Au10 co-implanted samples, the PL intensity is enhanced by the formation of ultra small Au clusters (occurring up to T=600 °C) that via short-range non-radiative coupling sensitize the Er^{3+} emission at 1540 nm, as already discussed. Moreover, when the cluster size becomes larger than 10–20 atoms (due to cluster growth at T>600 °C) the PL intensity decreases to values comparable to those of Er-Xe co-implanted samples, in which the energy-transfer process does not occur. This result in particular suggests that the contribution of the implantation defects as the main source of energy-transfer to Er^{3+} ions can be ruled out.

Indeed to get deeper information on the luminescent behaviour of Er-Xe co-implanted samples, PL measurements have been also performed in out-of-resonance excitation condition (at λ=476.5 nm). As can be seen in Fig. 4.14(b), in the whole range of annealing temperatures no evidence of 1540 nm PL emission has been detected. This can be considered as a conclusive evidence of the absence of any energy-transfer process (at the explored excitation wavelengths) in the Xe-implanted samples, contrary to what was found for the Au-implanted samples. Therefore, the present result further supports the conclusion that molecule-like Au clusters are required to achieve a broadband energy-transfer to Er^{3+} ions [36, 39, 73].

4.5.3 Structural characterization

To evaluate the structural similarity between Xe-implanted and Au-implanted Er co-doped silica layers the morphological and compositional characterization of the samples was performed in cross-section by Transmission Electron Microscopy (TEM) with a FEI TECNAI F20 (S)TEM field-emission gun (FEG) microscope operating at 200 keV, equipped with an EDAX energy dispersive x-ray spectrometer (EDS) for compositional analysis and a Scanning TEM (STEM) attachment with a high-angle annular detector for dark field STEM imaging (HAADF-STEM).

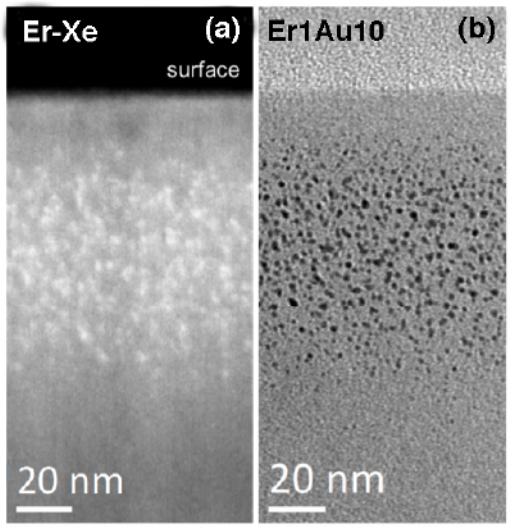

Figure 4.15: (a) Cross-sectional HAADF-STEM image of the Er-Xe co-implanted sample annealed at 800 °C; (b) BF-TEM cross-section of the Er1Au10 sample annealed at 800 °C.

Figure 4.15(a) shows the cross-section image of the Er-Xe sample annealed at 800 °C taken in STEM high-angle annular dark field (HAADF-STEM) mode. With this technique the image contrast is proportional to the atomic number; therefore the bright spots below the surface can be interpreted as Xe clusters (bubbles) with the size of about 2 nm. No lattice fringes can be detected in high-resolution mode (HR-TEM) nor diffraction rings with electron diffraction, indicating clearly that Xe aggregates are amorphous clusters or gas bubbles. As pointed out by Oliviero et al. in Ref. [79], large Xe bubbles can be formed in silica under high fluence Xe implantation (above 10^{16}ions/cm^2); their formation is generally attributed to the low solubility of noble gas atoms in silica host which therefore tend to segregate in the damaged matrix. The relatively low solubility of Xe is also typical of Au in silica. For comparison, Fig. 4.15(b) shows the bright-field (BF-TEM) cross-section image of the sample Er1Au10 annealed at the same temperature. Crystalline spherical Au nanoclusters were detected with size 1.6±0.5 nm, i.e., very similar to that of the Xe bubbles of the Er-Xe sample.

4.5.4 EXAFS measurements

To investigate the nature of the implantation induced damage on the Er site, EXAFS analyses at the Er absorption edge were performed to correlate the PL results with the evolution of the local atomic structure around Er ions (details on the experimental set-up can be found in Ref. [72]). The EXAFS spectra of the Er-Xe co-implanted samples are reported in Fig. 4.16(a) and

compared with the spectrum of the reference sample Er800 without Xe implantation; in Fig. 4.16(b) the Fourier transform (FT) moduli are shown together with the best-fit curves. For all the samples, the EXAFS signal -damped at high k values- is typical of light backscatterers, i.e., mainly oxygen in this case. The EXAFS spectra show some differences in the k=5.5–8 $Å^{-1}$ region: in particular, in this range the signal of the as-implanted sample is very low, while it progressively increases at higher annealing temperatures. Correspondingly, the main peak of the Fourier transform modulus related to the Er-O coordination (Fig. 4.16(b)) is highly asymmetric for the as-implanted sample, while the shoulder on its right-hand side (at R ∼2–2.5 Å) progressively fades away at higher temperature leading to an almost symmetric peak upon annealing at 800 °C.

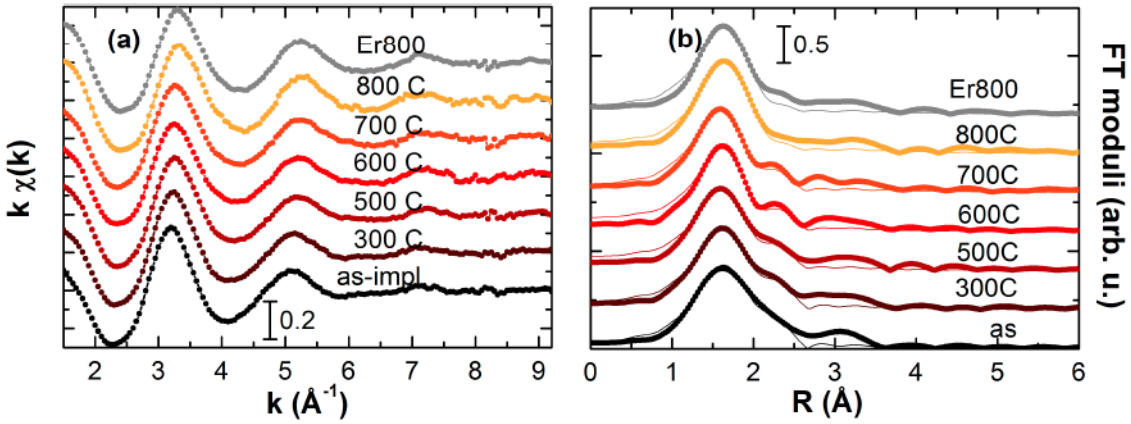

Figure 4.16: EXAFS spectra of the Er-Xe co-implanted samples, compared to the spectrum of the Er800 reference sample; (b) k^2-weighted Fourier transform (in the range k=2–8 $Å^{-1}$) moduli (full circles) and fits (solid line) of the spectra in (a).

To properly fit the first shell EXAFS signal, including the shoulder on the right-hand side, two different coordinations have to be considered: in fact, the use of an asymmetric distance distribution alone failed to reproduce the experimental data. The shorter coordination is the dominant signal and comes from the nearest O shell; the second one is responsible for the shoulder of the first peak in the Fourier transform moduli, and is related to a light backscatterer, such as Si and/or O. This signal is a minor part of the whole first shell contribution to the EXAFS spectrum, so the data analysis alone could not lead to strong conclusive arguments about the nature of the backscatterer (O or Si, or even a coexistence of both). Nevertheless, considering that this second contribution to the first shell is thermodynamically unstable (it vanishes at high annealing temperature) and the ion implantation process determines a depletion of O atoms in the implanted region favoring the formation of dopant-Si bonds, this contribution to the first shell is more likely due to Si atoms. Similarly to this case, it has been shown that the local site of Er ions co-implanted with O in crystalline Si exhibit a main Er–Si coordination that is progressively substituted by the more stable Er–O coordination upon annealing [80] (as a comparison, the heat of formation ΔH_f of Er_2O_3 is 1898 kJ/mol [81], with respect to ∼85 and ∼63 kJ/mol of ErSi and $ErSi_2$, respectively [82]). Another fact that supports this picture is that a first attempt to fit the first shell experimental data with O atoms at two different distances led to a Debye-Waller factor higher for the spectra of the samples annealed at higher temperature, that is unlikely to happen.

For the first shell, the results of the EXAFS analyses are reported in Table 4.2, in the

Table 4.2: Results of the EXAFS analysis for the first shell for Er-Xe and Er800 samples; N is the coordination number, R the interatomic distance. The Debye Waller factor σ^2 has been set to $(13\pm2)\times10^{-3}$ Å for all the samples and for both O– and Si–coordination, as estimated by the first shell fitting of the spectra from the 800°C annealed samples. In last column the PL intensity measured under resonant excitation is reported.

Sample	Temp. [°C]	O coordination		Si coordination		PL Intensity [Arb. u.]
		N	R [Å]	N	R [Å]	
Er-Xe	-	4.9±0.6	2.18±0.02	1.8±0.5	2.69±0.04	-
Er-Xe	300	4.8±0.6	2.18±0.02	1.5±0.5	2.71±0.04	-
Er-Xe	500	4.7±0.6	2.16±0.02	1.3±0.5	2.72±0.04	0.2±0.05
Er-Xe	600	4.9±0.6	2.16±0.02	1.0±0.5	2.79±0.04	0.5±0.1
Er-Xe	700	4.9±0.6	2.14±0.03	1.0±0.7	2.72±0.07	1.5±0.2
Er-Xe	800	5.7±0.6	2.17±0.02	0.5±0.6	2.84±0.09	2.3±0.2
Er800	800	5.6±0.6	2.17±0.02	0.5±0.5	2.79±0.06	2.6±0.2

last column the measured PL intensity is also reported. For the as-implanted Er-Xe sample, the average Er site is composed of about 5 O atoms and about 2 Si atoms. The Er–O distance is significantly shorter than in the Er_2O_3 and $Er_2Si_2O_7$ crystals (where R=2.23–2.31 Å), but it is in the range of distances usually observed for Er-doped silica-based systems [43, 83, 84], especially when the synthesis conditions are far from equilibrium. Moreover, the Er–Si distance is significantly shorter than in Er–silicide crystals (about 3.00 Å in $ErSi_2$ and 2.80–3.17 Å in ErSi); nevertheless, theoretical analysis on Er+O–doped crystalline Si indicates Er–O and Er–Si first shell distances of 2.18 Å and 2.60 Å, respectively, in good agreement with the values found in the present case [85]. Upon the increasing temperature annealing, the number of O atoms in the first shell increases, and Er ions reach practically the full octahedral coordination, i.e. the standard six-fold coordination of Er^{3+} in crystals with annealing at T=800 °C; correspondingly, the number Si atoms in the first shell significantly decreases and becomes negligible for the Er-Xe co-implanted sample annealed at 800 °C (see Table 4.2). Thus, the presence of both Si and O atoms in the first shell (observed for annealing temperatures below 800 °C) likely suggests that the electronic configuration around the Er site may be different from that of Er ions octahedrally coordinated with just O atoms. Moreover, the EXAFS signals from the reference sample and the Er-Xe co-implanted sample both annealed at 800°C, are identical (see Fig. 4.16(a) and Table 4.2). These results indicate that the Er–Si coordination in the first shell is related to the defects formed upon Xe implantation: at high temperature annealing the matrix and the Er site recover from irradiation damage and, correspondingly, the Er–Si coordination vanishes, leaving only the octahedral coordination with O atoms.

In conclusion, from Table 4.2 it can be seen that good direct correlation can be established between Er^{3+} PL intensity and the Er–O coordination number, indicating that in the absence of sensitizing species, the main contribution to the Er^{3+} PL intensity at 1540 nm comes from a properly structured Er^{3+} environment, i.e., when the fully octahedral configuration of the oxygen atoms around each Erbium ion is reconstructed by the thermal annealing, with the consequent fading of the Er–Si first shell contribution, proven by the observation that the Xe-implanted Er-doped silica recoveries a PL efficiency (both intensity and lifetime) very similar to the reference sample (Er800).

4.6 Conclusions

The effect of sub-nanometer Au clusters on the Er^{3+} luminescence at 1540 nm in Er-Au co-implanted silica has been elucidated. It has been demonstrated that the energy-transfer mechanism controlling the sensitization process of Er ions in the presence of gold sub-nanometric clusters is a non-radiative short-range interaction with an estimated coupling length of the order of 0.5 nm. Since the energy-transfer process is mediated by the broad-band interband absorption of the sub-nanometer Au clusters, the Er^{3+} excitation can be achieved by using pumping sources more convenient than lasers such as LEDs or white light sources.

Exploring [Er]/[Au] concentration ratios spanning over more than one order of magnitude, it has been demonstrated that with an opportune post-implantation thermal treatment an enhancement of the PL intensity of more than one order of magnitude can be achieved. Systematic photoluminescence characterizations performed both for resonant and out-of-resonance Er excitation conditions revealed that the sensitization mechanism is characterized by a large effective cross-section, more than three orders of magnitude larger that the intrinsic cross-section for Er emission. Furthermore, studying the implantation damage of Xe ions to the Er-doped silica systems, the possibility that matrix defects behave as active species in the Er sensitization process has been ruled out and it was demonstrated that the optimization of the Er luminescent properties in silica is connected to the recovery of the first shell full octahedral coordination of oxygen atoms around Er ions.

General conclusions

The present thesis deals with the interaction of plasmonic and pre-plasmonic nanostructures with an emitter in close proximity. The investigation was carried out following different approaches (i.e., plasmonic coupling with planar interfaces, interaction with nanostructures with 2D periodic pattern and energy-transfer from pre-plasmonic noble metal sub-nanometric clusters), but always with the aim of inserting the experimental results in the framework of new or existing theoretical models in order to better understand the photophysical nature of the interaction. This approach allowed the development of predictive models that can be used in the design of novel devices for different photonic applications.

In this framework, the choice of Erbium-doped silica as emitting source was driven by the great technological importance of this rare earth in photonics and optoelectronics. In particular, the strategy adopted was to work with an emitting system as efficient as possible. For this reason the first step of the research activity was devoted to the optimization of the Er^{3+} PL properties in silica. For the synthesis of the Er-doped films, two different fabrication techniques have been used: magnetron co-sputtering and ion implantation. The first approach in particular allows a fine tuning of the thickness of the doped layer and its distance from the surface, necessary to study the interaction with thin films and nanohole arrays where the separation distance is a crucial parameter. Regardless of the fabrication method, a high temperature annealing (above 600 °C) was found to be necessary for the activation of the Er^{3+} characteristic emission at 1540 nm. Moreover, for the co-sputtered samples it has been observed that an annealing in vacuum atmosphere has a beneficial effect on the PL intensity due to the out-diffusion of quenching species from the deposited silica layer. From PL measurements on the other hand the excitation cross section for Er^{3+} in silica was estimated to be of the order of 10^{-21} cm^2. It is worth noting that such low value represents one of the main limitations to the development of new photonic devices based on Er-doped materials. An additional limitation may derive from the long lifetime of the Erbium emission. The Erbium $^4I_{13/2} \rightarrow ^4I_{15/2}$ transition is characterized by a lifetime of several milliseconds: such long permanence in the excited state makes the rare earth sensitive to non-radiative decay processes and in particular limits the maximum Er concentration for an efficient emission at 1540 nm. It has been observed, indeed, that the measured decay rate increases roughly linearly with the concomitant increase of Er concentration, decreasing the quantum efficiency of the radiative process. Quantum efficiencies of the radiative emission close to the unity have been obtained in the limit of very low Er concentration (of about 0.1 %at.), for which the non-radiative decay rate results almost negligible.

The investigation of the modification of the optical properties of an emitter due to proximity of an interface demonstrated that a strong control on the lifetime can be achieved by varying the overlayer material and the distance from the interface. To describe the decay rate modification different contributions have to be taken into account: the variation of the local density of state due to the reflection from the interface, the coupling of the emitted radiation with propagating surface plasmons on the metal-dielectric interface and the dissipation in the overlayer. The experimental results were compared with the theoretical description derived

from the model proposed by Chance et al., and an excellent agreement has been found between the theoretical predictions and the measured values for dielectric (air), metallic (Au, Ag, Cr, Ti) and semiconducting (Si) overlayers, providing an useful tool to predict the variation of the decay rate and to choose the optimum overlayer material in the design of new photonic devices. In particular, the highest reduction of the Er^{3+} lifetime (up to 1/3 of the initial value) has been obtained by interaction with metallic optically thick films. Moreover, the efficient coupling between Er emission at 1540nm and propagating surface plasmons at the SiO_2–noble metal interface has been proven, showing that if the SPPs are efficiently coupled out, the radiative efficiency of the Er^{3+} transition at 1540 nm can be further enhanced.

A further step ahead in the improvement of the optical properties of an emitter was obtained when a noble metal overlayer is patterned with a 2D periodic array of nanometer-sized holes. A combination of nanosphere lithography and reactive ion etching offered a convenient and versatile method for the fabrication of highly ordered NHAs on large areas. The optical properties of these systems can be tailored simply by acting on the self-assembling nanoparticles size and the etching duration. It has been proven that by coupling with resonant and non-resonant gold NHAs, the decay rate of the Erbium radiative emission at 1540nm can be strongly enhanced, particularly when the NHA EOT peak matches the emission wavelength. Moreover, the investigation of the dependence of the lifetime shortening on the distance between the emitter and the plasmonic nanostructure has pointed out that the coupling is stronger as the distance decreases, especially for resonant NHAs. The experimental data have been compared with FEM simulations, demonstrating not only a strong coupling of the emitted radiation with propagating SP modes, but also that the dissipation in the gold nanostructures is negligible, so that the higher photon flux is all available in the far-field. The results revealed that the coupling of Er:SiO_2 thin films with gold NHAs offers several advantages for the realization of plasmonic-based devices. In fact, unlike the film geometry, the surface plasmons propagating on the metal-dielectric interface are directly coupled out into far-field radiation contributing to the overall signal. Moreover, the emitted radiation can be collected from both sides of a NHA and its angular distribution can be tailored simply by acting on the holes periodicity. Finally, it is worth noting that NHAs are optical filters whose transmitted wavelength is determined by the lattice parameter and a combination of NHAs with different periodicity opens new prospectives for the design of smart excitation-emission configurations.

Furthermore, the enhancement of the photoluminescence properties of an emitter can be obtained not only acting on the emission process, but also increasing the excitation cross section. For this purpose, an interesting opportunity is represented by the sensitization effect of the ultra-small gold clusters obtained by ion implantation on the Er^{3+} emission at 1540 nm. Although such noble metal clusters are too small to have the continuous density of states necessary for plasmon excitations to be supported, nonetheless they can efficiently interact with nearby emitters, absorbing light through interband transition and transferring subsequently to the emitter the energy necessary for the excitation. It has been demonstrated that the energy-transfer process from the Au nanoclusters (Au NCs) to the Er ions is a short-range coupling mechanism and it can be described in the framework of the Förster energy-transfer theory. Long-range interaction effects as those mediated by the emission of photons from the Au NCs subsequently absorbed by the Er ions have been ruled out. Exploring the influence of size and density of the Au NCs on the Er^{3+} PL intensity at 1540 nm, it has been found out that independently of the initial Au concentration in the silica matrix the highest sensitization effect occurs when the Au NCs are made by about 10–20 atoms. Tailoring the Au implantation fluence and the post-implantation annealing necessary for the Au clustering, an enhancement

of the PL intensity of more than one order of magnitude has been achieved. Moreover a simple phenomenological model for the Er sensitization mediated by energy-transfer from Au NCs has been developed through which the effective cross-section and the interaction distance of the energy-transfer process have been determined. The results revealed that the sensitization mechanism is characterized by a large effective cross section, more than three orders of magnitude larger that the intrinsic cross section for Er emission. Nonetheless only a limited fraction of the Er ions can be indirectly excited by energy-transfer from the Au NCs. Moreover, interaction distances of the order of 0.5 nm were estimated, further confirming the short-range character of the energy-transfer mechanism. An additional advantage of the Au NCs sensitization is that the light is absorbed through broad-band interband transition in metal clusters, therefore the Er^{3+} exciting can be achieved through non-resonant pumping. This has important technological entailments for the possible applications of these systems in photonic and optoelectronic devices, exploiting broad-band pumping sources.

In conclusion, on the basis of all the obtained results discussed in this thesis, promising opportunities in the development of novel and more efficient photonic devices can be foreseen. The research in this field is far from being completed and many interesting issues for the future research can be suggested. For instance the investigation of the coupling of Er:SiO_2 thin films with a graphene layer could lead to further PL enhancement due to its promising plasmonic properties in the near-IR region. A deeper comprehension on mechanisms involved in the emitter-NHA coupling can contribute to the development of a full theoretical description of the interaction. Concerning the molecular-like metal cluster, further insights in the understanding of the photophysical nature of the sensitization effect can be obtained by a deeper investigation of the dynamics of the energy-transfer mechanism under ultra-short laser pulses or by the exploration of other metallic species or alloys.

Bibliography

[1] R. P. Feynman, "There's plenty of room at the bottom," Engineering and Science **23**, 22–36 (1960).

[2] N. Taniguchi *et al.*, "On the basic concept of nanotechnology," in "Proc. Intl. Conf. Prod. Eng. Tokyo, Part II, Japan Society of Precision Engineering," (1974), pp. 18–23.

[3] S. A. Maier, *Plasmonics: fundamentals and applications* (Springer, 2007).

[4] E. M. Purcell, "Spontaneous emission probabilities at radio frequencies," Physical Review **69**, 681 (1946).

[5] R. Amos and W. Barnes, "Modification of the spontaneous emission rate of eu^{3+} ions close to a thin metal mirror," Physical Review B **55**, 7249 (1997).

[6] T. W. Ebbesen, H. Lezec, H. Ghaemi, T. Thio, and P. Wolff, "Extraordinary optical transmission through sub-wavelength hole arrays," Nature **391**, 667–669 (1998).

[7] P. Anger, P. Bharadwaj, and L. Novotny, "Enhancement and quenching of single-molecule fluorescence," Physical review letters **96**, 113002 (2006).

[8] A. Polman, "Erbium implanted thin film photonic materials," Journal of Applied Physics **82**, 1–39 (1997).

[9] W. J. Miniscalco, "Erbium-doped glasses for fiber amplifiers at 1500 nm," J. Lightwave Technol. **9**, 234–250 (1991).

[10] A. M. Glass, "Fiber optics," Physics Today **46**, 34 (1993).

[11] E. Desurvire, "The golden age of optical fiber amplifiers," Physics Today **47**, 20 (1994).

[12] S. Hufner, *Optical spectra of transparent rare earth compounds* (Academic Press, 1978).

[13] C. Layne, W. Lowdermilk, and M. J. Weber, "Multiphonon relaxation of rare-earth ions in oxide glasses," Physical Review B **16**, 10 (1977).

[14] P. M. Becker, A. A. Olsson, and J. R. Simpson, *Erbium-doped fiber amplifiers: fundamentals and technology* (Access Online via Elsevier, 1999).

[15] P. Blixt, J. Nilsson, T. Carlnas, and B. Jaskorzynska, "Concentration-dependent upconversion in er^{3+}-doped fiber amplifiers: Experiments and modeling," Photonics Technology Letters, IEEE **3**, 996–998 (1991).

[16] F. Auzel, "Upconversion processes in coupled ion systems," Journal of Luminescence **45**, 341–345 (1990).

[17] E. Snoeks, P. Kik, and A. Polman, "Concentration quenching in erbium implanted alkali silicate glasses," Optical Materials **5**, 159–167 (1996).

[18] A. Kenyon, "Recent developments in rare-earth doped materials for optoelectronics," Prog. Quant. Electron. **26**, 225 (2002).

[19] F. Auzel, "Multiphonon-assisted anti-stokes and stokes fluorescence of triply ionized rare-earth ions," Physical Review B **13**, 2809 (1976).

[20] M. P. Hehlen, N. J. Cockroft, T. R. Gosnell, and A. J. Bruce, "Spectroscopic properties of er^{3+}- and yb^{3+}-doped soda-lime silicate and aluminosilicate glasses," Phys. Rev. B **56**, 9302–9318 (1997).

[21] C. Strohhofer and A. Polman, "Absorption and emission spectroscopy in er^{3+} yb^{3+}-doped aluminum oxide waveguides," Opt. Mat. **21**, 705 (2003).

[22] M. Fuji, M. Yoshida, Y. Kanzawa, S. Hayashi, and K. Yamamoto, "1.54-mm photoluminescence of er^{3+} doped into sio_2 films containing si nanocrystals: evidence for energy transfer from si nanocrystals to er^{3+}," Appl. Phys. Lett. **71**, 1198 – 1200 (1997).

[23] C. E. Chryssou, A. J. Kenyon, T. S. Iwayama, C. W. Pitt, and D. E. Hole, "Evidence of energy coupling between si nanocrystals and er^{3+} in ion-implanted silica thin films," Applied Physics Letters **75**, 2011–2013 (1999).

[24] G. Franzò, V. Vinciguerra, and F. Priolo, "The excitation mechanism of rare-earth ions in silicon nanocrystals," Appl. Phys. A **69**, 3 (1999).

[25] D. Pacifici, G. Franzò, F. Priolo, F. Iacona, and L. Dal Negro, "Modeling and perspectives of the si nanocrystals-er interaction for optical amplification," Phys. Rev. B **67**, 245301 (2003).

[26] F. Enrichi, G. Mattei, C. Sada, E. Trave, D. Pacifici, G. Franzò, F. Priolo, F. Iacona, M. Prassas, M. Falconieri, and E. Borsella, "Study of the energy transfer mechanism in different glasses co-doped with Si nanoaggregates and Er^{3+} ions," Opt. Mat. **27**, 904 – 909 (2005).

[27] L. Jin, D. Li, L. Xiang, F. Wang, D. Yang, and D. Que, "Energy transfer from luminescent centers to $erer^{3+}$ in erbium-doped silicon-rich oxide films," Nanoscale research letters **8**, 1–6 (2013).

[28] L. Slooff, A. Polman, M. Oude Wolbers, F. Van Veggel, D. Reinhoudt, and J. Hofstraat, "Optical properties of erbium-doped organic polydentate cage complexes," Journal of applied physics **83**, 497–503 (1998).

[29] L. Slooff, A. Van Blaaderen, A. Polman, G. Hebbink, S. Klink, F. Van Veggel, D. Reinhoudt, and J. Hofstraat, "Rare-earth doped polymers for planar optical amplifiers," Journal of Applied Physics **91**, 3955–3980 (2002).

[30] B. Chen, Y. Yang, F. Zapata, G. Qian, Y. Luo, J. Zhang, and E. B. Lobkovsky, "Enhanced near-infrared-luminescence in an erbium tetrafluoroterephthalate framework," Inorganic Chemistry **45**, 8882–8886 (2006).

[31] R. V. Deun, P. Nockemann, C. Gorller-Walrand, and K. Binnemans, "Strong erbium luminescence in the near-infrared telecommunication window," Chemical Physics Letters **397**, 447 – 450 (2004).

[32] G. Mancino, A. J. Ferguson, A. Beeby, N. J. Long, and T. S. Jones, "Dramatic increases in the lifetime of the er^{3+} ion in a molecular complex using a perfluorinated imidodiphosphinate sensitizing ligand," Journal of the American Chemical Society **127**, 524–525 (2005).

[33] C. Strohhofer and A. Polman, "Silver as a sensitizer for erbium," Appl. Phys. Lett. **81**, 1414 (2002).

[34] A. Martucci, M. de Nuntis, A. Ribaudo, M. Guglielmi, S. Padovani, F. Enrichi, G. Mattei, P. Mazzoldi, C. Sada, E. Trave, G. Battaglin, F. Gonella, E. Borsella, M. Falconieri, M. Patrini, and J. Fick, "Silver sensitized erbium doped ion exchanged sol gel waveguides," Appl. Phys. A **80**, 557 – 563 (2004).

[35] H. Portales, M. Mattarelli, M. Montagna, A. Chiasera, M. Ferrari, A. Martucci, P. Mazzoldi, S. Pelli, and G. Righini, "Investigation of the role of silver on spectroscopic features of er^{3+}-activated ag-exchanged silicate and phosphate glasses," Journal of Non-Crystalline Solids **351**, 1738 – 1742 (2005). SiO, Advanced Dielectrics and Related Devices 5.

[36] E. Trave, G. Mattei, P. Mazzoldi, G. Pellegrini, C. Scian, C. Maurizio, and G. Battaglin, "Sub-nanometric metallic au clusters as efficient er^{3+} sensitizers in silica," Applied physics letters **89**, 151121–151121 (2006).

[37] M. Mattarelli, M. Montagna, K. Vishnubhatla, A. Chiasera, M. Ferrari, and G. C. Righini, "Mechanisms of ag to er energy transfer in silicate glasses: a photoluminescence study," Phys. Rev. B **75**, 125102 (2007).

[38] M. Eichelbaum and K. Rademann, "Plasmonic enhancement or energy transfer? on the luminescence of gold-, silver-, and lanthanide-doped silicate glasses and its potential for light-emitting devices," Advanced Functional Materials **19**, 2045–2052 (2009).

[39] C. Maurizio, E. Trave, G. Perotto, V. Bello, D. Pasqualini, P. Mazzoldi, G. Battaglin, T. Cesca, C. Scian, and G. Mattei, "Enhancement of the er^{3+} luminescence in er-doped silica by few-atom metal aggregates," Physical Review B **83**, 195430 (2011).

[40] J. M. Khosrofian and B. A. Garetz, "Measurement of a gaussian laser beam diameter through the direct inversion of knife-edge data," Applied Optics **22**, 3406–3410 (1983).

[41] E. Cattaruzza, G. Battaglin, F. Visentin, and E. Trave, "Er-doped sio_2 films by rf magnetron co-sputtering," Journal of Non-Crystalline Solids **355**, 1128 – 1131 (2009).

[42] L. Slooff, M. De Dood, A. Van Blaaderen, and A. Polman, "Effects of heat treatment and concentration on the luminescence properties of erbium-doped silica sol–gel films," Journal of non-crystalline solids **296**, 158–164 (2001).

[43] C. Maurizio, F. Iacona, F. D'Acapito, G. Franzò, and F. Priolo, "Er site in er-implanted si nanoclusters embedded in sio_2," Physical Review B **74**, 205428 (2006).

[44] A. Polman, "Erbium as a probe of everything?" Physica B: Condensed Matter **300**, 78 – 90 (2001).

[45] T. Förster, "Zwischenmolekulare energiewanderung und fluoreszenz," Ann. Phys. p. 55 (1948).

[46] W. L. Barnes, R. I. Laming, E. J. Tarbox, and P. Morkel, "Absorption and emission cross section of er^{3+} doped silica fibers," Quantum Electronics, IEEE Journal of **27**, 1004–1010 (1991).

[47] D. McCumber, "Einstein relations connecting broadband emission and absorption spectra," Physical Review **136**, A954 (1964).

[48] J. F. Ziegler, J. P. Biersack, and M. D. Ziegler, *SRIM–The Stopping Range of Ions in Matter* (Ion Implantation Press, 2008).

[49] J. Wright and F. Fong, "Radiationless processes in molecules and condensed phases," Topics in applied physics **15** (1976).

[50] K. Drexhage, M. Fleck, H. Kuhn, F. Schafer, and W. Sperling, "Beeinflussung der fluoreszenz eines europium-chelates durch einen spiegel," Ber. Bunsenges. Phys. Chem **70**, 1179 (1966).

[51] K. H. Drexhage, H. Kuhn, and F. P. Schäfer, "Variation of the fluorescence decay time of a molecule in front of a mirror," Berichte der Bunsengesellschaft für physikalische Chemie **72**, 329–329 (1968).

[52] K. H. Drexhage, "Monomolecular layers and light," Scientific American **222**, 108–119 (1970).

[53] K. Drexhage, "Influence of a dielectric interface on fluorescence decay time," Journal of Luminescence **1–2**, 693 – 701 (1970).

[54] K. H. Drexhage, "Interaction of light with monomolecular dye layers," (Elsevier, 1974), pp. 163 – 232.

[55] J.-Y. Zhang, X.-Y. Wang, and M. Xiao, "Modification of spontaneous emission from cdse/cds quantum dots in the presence of a semiconductor interface," Optics letters **27**, 1253–1255 (2002).

[56] Y. Zhang, V. K. Komarala, C. Rodriguez, and M. Xiao, "Controlling fluorescence intermittency of a single colloidal cdse/zns quantum dot in a half cavity," Physical Review B **78**, 241301 (2008).

[57] M. Leistikow, J. Johansen, A. Kettelarij, P. Lodahl, and W. Vos, "Size-dependent oscillator strength and quantum efficiency of cdse quantum dots controlled via the local density of states," Physical Review B **79**, 045301 (2009).

[58] E. Fermi, "Quantum theory of radiation," Reviews of modern physics **4**, 87–132 (1932).

[59] W. Barnes, "Fluorescence near interfaces: the role of photonic mode density," journal of modern optics **45**, 661–699 (1998).

[60] M. Yeung and T. Gustafson, "Spontaneous emission near an absorbing dielectric surface," Physical Review A **54**, 5227 (1996).

[61] R. Chance, A. Miller, A. Prock, and R. Silbey, "Fluorescence and energy transfer near interfaces: The complete and quantitative description of the eu/mirror systems," The Journal of Chemical Physics **63**, 1589 (1975).

[62] R. Chance, A. Prock, and R. Silbey, "Molecular fluorescence and energy transfer near interfaces," Adv. Chem. Phys **37**, 65 (1978).

[63] R. Chance, A. Prock, and R. Silbey, "Comments on the classical theory of energy transfer," The Journal of Chemical Physics **62**, 2245 (1975).

[64] K. G. Sullivan and D. G. Hall, "Enhancement and inhibition of electromagnetic radiation in plane-layered media. i.plane-wave spectrum approach to modeling classical effects," J. Opt. Soc. Am. B **14**, 1149–1159 (1997).

[65] J. Bao, N. Yu, F. Capasso, T. Mates, M. Troccoli, and A. Belyanin, "Controlled modification of erbium lifetime in silicon dioxide with metallic overlayers," Applied Physics Letters **91**, 131103–131103 (2007).

[66] E. D. Palik, *Handbook of Optical Constants of Solids: Index*, vol. 3 (Access Online via Elsevier, 1998).

[67] P. B. Johnson and R.-W. Christy, "Optical constants of the noble metals," Physical Review B **6**, 4370 (1972).

[68] R. Chance, A. Miller, A. Prock, and R. Silbey, "Luminescent lifetimes near multiple interfaces: a quantitative comparison of theory and experiment," Chemical Physics Letters **33**, 590–592 (1975).

[69] P. Andrew and W. L. Barnes, "Molecular fluorescence above metallic gratings," Phys. Rev. B **64**, 125405 (2001).

[70] G. Ford and W. Weber, "Electromagnetic interactions of molecules with metal surfaces," Physics Reports **113**, 195–287 (1984).

[71] J. Kalkman, L. Kuipers, A. Polman, and H. Gersen, "Coupling of er ions to surface plasmons on ag," Applied Physics Letters **86**, 041113–041113 (2005).

[72] T. Cesca, C. Maurizio, B. Kalinic, G. Perotto, P. Mazzoldi, E. Trave, G. Battaglin, and G. Mattei, "Implantation damage effects on the er^{3+} luminescence in silica," Optics Express **20**, 16639–16649 (2012).

[73] T. Cesca, B. Kalinic, C. Maurizio, C. Scian, G. Battaglin, P. Mazzoldi, and G. Mattei, "Near-infrared room temperature luminescence of few-atom au aggregates in silica: a path for the energy-transfer to er^{3+} ions," Nanoscale (2014).

[74] D. Barbier, M. Rattay, F. Saint Andre, G. Clauss, M. Trouillon, A. Kevorkian, J.-M. Delavaux, and E. Murphy, "Amplifying four-wavelength combiner, based on erbium/ytterbium-doped waveguide amplifiers and integrated splitters," Photonics Technology Letters, IEEE **9**, 315–317 (1997).

[75] P. Kik, M. Brongersma, and A. Polman, "Strong exciton-erbium coupling in si nanocrystal-doped sio2," Applied Physics Letters **76**, 2325–2327 (2000).

[76] S. Latt, H. Cheung, and E. Blout, "Energy transfer. a system with relatively fixed donor-acceptor separation," Journal of the American Chemical Society **87**, 995–1003 (1965).

[77] D. L. Dexter, "A theory of sensitized luminescence in solids," The Journal of Chemical Physics **21**, 836–850 (1953).

[78] B. Julsgaard, Y.-W. Lu, R. V. Skougaard Jensen, T. G. Pedersen, K. Pedersen, J. Chevallier, P. Balling, and A. Nylandsted Larsen, "Er sensitization by a thin si layer: Interaction-distance dependence," Physical Review B **84**, 085403 (2011).

[79] E. Oliviero, M.-O. Ruault, B. Décamps, F. Fotuna, E. Ntsoenzok, O. Kaïtasov, and S. Collin, "Synthesis of mesoporous amorphous silica by kr and xe ion implantation: Transmission electron microscopy study of induced nanostructures," Microporous and Mesoporous Materials **132**, 163–173 (2010).

[80] A. Terrasi, G. Franzo, S. Coffa, F. Priolo, F. DAcapito, and S. Mobilio, "Evolution of the local environment around er upon thermal annealing in er and o co-implanted si," Applied physics letters **70**, 1712–1714 (1997).

[81] D. R. Lide, *CRC Handbook of Chemistry and Physics 2004-2005: A Ready-Reference Book of Chemical and Physical Data* (CRC press, 2004).

[82] N. Gorbachuk, S. Kirienko, V. Sidorko, and I. Obushenko, "Thermodynamic properties of erbium mono-and disilicide at low temperatures," Powder Metallurgy and Metal Ceramics **46**, 72–76 (2007).

[83] C. Piamonteze, A. Iniguez, L. Tessler, M. M. Alves, and H. Tolentino, "Environment of erbium in a-si: H and a-sio$_x$: H," Physical review letters **81**, 4652 (1998).

[84] M. Marcus, D. Jacobson, A. Vredenberg, and G. Lamble, "Concentration and annealing effects on photoluminescence and local structure of er-implanted silica," Journal of non-crystalline solids **195**, 232–238 (1996).

[85] J. Wan, Y. Ling, Q. Sun, and X. Wang, "Role of codopant oxygen in erbium-doped silicon," Physical Review B **58**, 10415 (1998).